Growth, Structure and Properties of Ultra-Thin Metal-Organic Films

By

Mrinal Kanti Bera

S. N. Bose National Centre for Basic Sciences,

JD Block, Sector III, Salt Lake, Kolkata-700098, India

A Thesis submitted to

West Bengal University of Technology

in partial fulfillment for the Degree of

Doctor of Philosophy **(Science)**

September, 2009

To my beloved Grandmother...

Acknowledgments

This thesis took six years to take shape and it would not have been possible to complete it without the constant help and support of some people who are well known to me. I would like to take this opportunity to acknowledge them all and thank them. I would also like to beg pardon, if I forget to mention anyone of them here.

First of all, I would like to devote my earnest thanks to my Thesis Supervisor Prof. Milan Kumar Sanyal for introducing me to the highly exciting and emerging field of Nanoscience and the evolving X-ray scattering techniques to probe them. He is an excellent experimentalist, a good teacher, an excellent guide and above all a noble hearted person. He always extracts time from his busy schedule to come with us to teach and guide us performing experiments at different Synchrotron sources. Whatever knowledge I have gained from this six years period of research regarding the use of X-ray scattering techniques to probe structures of matter is due to him.

I would like to give my special thanks to my Thesis Co-Supervisor Prof. Sushanta Dattagupta, who always motivated me to do experiments though he himself is a Theoretical Physicist. He provided me the required freedom and support throughout the period of my thesis work. He is an excellent physicist and wonderful teacher. I will never forget his classes on Classical Mechanics and a Special Course on Statistical Mechanics while doing my Masters Degree.

During my thesis work, I met some excellent scientists across the world like Prof. C. N. R. Rao (India), Prof. J. Daillant (France), Prof. B. Lin (USA), Prof. L. Yang (USA), Prof. M. Meron (USA) through my Supervisor Prof. M. K. Sanyal. It is my priveledge that I got chances to collaborate and work with them. I thank them all for their kind support and help for my thesis work.

I also like to thank Prof. B. Sinha (Former Director, Saha Institute of Nuclear Physics (SINP)) and Prof. A. K. Raychaudhuri (Director, S. N. Bose National Centre for Basic Sciences (SNBNCBS)) for their kind permissions and support for carrying out my thesis work smoothly with the facilities in both the renowned institutes.

I would like to thank Prof. B. D. Ray, Prof. J. K. Bhattacharjee (Dean, SNBNCBS), Prof. A. Mookerjee (Head, Dept. of Material Science, SNBNCBS) for their help, support and valuable suggestions. They along with Prof. H. S. Mani and other distinguished Faculties from different institutes in Kolkata taught us the basic foundations of physics in the classes of our Masters Degree. I feel highly privileged to have learned from them. I also like to thank all the faculty members Prof. D. Ghosh, Prof P. Chakraborty, Prof. A. Datta, Prof. T. K. Chini, Prof. M. Mukherjee, Prof. S. Hazra, Prof. S. Kundu, Prof. S. Banerjee, Dr. S. Bhunyia and Dr. K. S. R Menon of Surface Physics Division (SPD), SINP, for their help, support and encouragement throughout my research work.

I would like to take this opportunity to thank all the Staff members of SNBNCBS and SINP. Specially I would like to thank Mr. S. Deb , Mr. S. Mukherjee, Mr. J. Kar and Mrs. S. Majumdar for their help and support through out my stay at SNBNCBS. I like to thank Mr. S. Banerjee, Mr. A. Das, Mr. S. Das, Mr. Souvik Banerjee and Mr. G. Sarkar of SPD, SINP for their support in my research work. I also like to thank Mr. Mukul Das, Mr. H. Jana, Mr. G. Jana and Mr. Mantu Das of SPD Office, SINP, for their help and support.

Apart from supervisor, a research student always learn and take support from his/her seniors, juniors and specially from batchmates and I am not the exception. I would like to take this opportunity to thank my batchmates Debabrata, Abhishek, Venkat, Navin and Manas for their company and help throughout my stay at SNBNCBS. I am really glad to have friends like them. I would also like to thank my Seniors Abhishek da, Manirul da, Mukul da, Santabrata da, Anuj da and Kamal da who gave us a warm welcome in SNBNCBS when we first came and made us felt like we were at home. I will never forget them for their anonymous support and help. After completing my Masters from SNBNCBS when I joined SINP

for my thesis work I came across my seniors Mrinmay da, Sudipta di, Mishreyee di, Amarjeet da, Sudeshna di, Atikur da and Indranil da. I learned lots of small but smart experimental tricks from them which helped me afterwards. Without their support, help and criticism it would not have been possible to give my work a shape as this thesis. I thank them all from my heart. I also like to thank Rupak, Puneet and Safiul from SINP and Kanishka, Kalyani and Neenu from Jawaharlal Nehru Centre for Advanced Scientific Research (JNCASR) for their help in doing some of the experiments. I would also like to thank Sirsendu, Abhisakh, Mojammel, Suman, Nupur, Paramita, Tanushree, Pabitra, Manjula and Bishnu for their support, enthusiasm and lively atmosphere in the laboratory.

Funding plays an important role in any kind of Research programme. In this regard, I would first of all like to thank SNBNCBS for funding during my Masters as well as throughout my research whenever needed. I am very much thankful to SINP for providing me all the facilities which an experimental research student needs. I would like to thank Council for Scientific and Industrial Research (CSIR), Govt. of India, for providing my adequate financial support as Junior and Senior Research Fellowship for the research period of five years. I would also like to thank Department of Science and Technology (DST), Govt. of India for providing my sufficient financial support to perform our experiments at various Synchrotron Sources across the globe.

Atlast, I would like to thank my parents (father and mother) and my parent in laws for having an unquestionable faith on me and giving me their never ending unconditional love, support and encouragement throughout my thesis work. It would be really unfair, if I forget to mention someone who played a very important role behind all i.e my wife Sagarika. Though she is from totally different academic background but she always took initiative to ask and motivate me for my work. I would like to take this opportunity to thank her too.

Mrinal Kanti Bera

List of Publications

1. "Reversible Buckling in Monolayer of Gold Nanoparticles on Water Surface", **M. K. Bera**, M. K. Sanyal, S. Pal, J. Daillant, A. Datta, G. U. Kulkarni, D. Luzet and O. Konovalov, *Europhysics Letters*, **78**, 56003-1-6 (2007).

2. "Formation and Ordering of Gold Nanoparticles at the Toluene-Water Interface", M. K. Sanyal, V. V. Agrawal, **M. K. Bera**, K. P. Kalyanikutty, J. Daillant, C. Blot, S. Kubowicz, O. Konovalov and C. N. R. Rao, *Journal of Physical Chemistry C (Letters)*, **112**, 1739-1743 (2008).

3. "Effect of Vibrations on the Formation of Gold Nanoparticle Aggregates at the Toluene-Water Interface", **M. K. Bera**, M. K. Sanyal, R. Banerjee, K. P. Kalyanikutty and C. N. R. Rao, *Chemical Physics Letters*, **461**, 97-101(2008).

4. "Small-Angle X-ray Scattering Study of the Aggregation of Gold Nanoparticles During the Formation at the Toluene-Water Interface", **M. K. Bera**, M. K. Sanyal, L. Yang, K. Biswas, A. Gibaud and C. N. R. Rao, *Communicated.*

5. "Non-Fickian Diffusion of Gold Nanoparticles in Ultrathin Polyacrylamide film", **M. K. Bera** and M. K. Sanyal, *Communicated.*

Contents

List of Figures

List of Tables

Chapter 1

Introduction

Last two decades have witnessed new directions of modern research broadly named as *Nanoscience and Technology* [1, 2, 3, 4]. Under these new directions, fabrication, characterization, manipulation of materials with a control over nanometer level and their possible applications have remained under intense focus of research. These new materials, fabricated with control over atomic dimensions, required for Nanoscience are termed as *Nanomaterials* and have the size in the range of 1-100 nanometers (nm). With this size-range, materials started to exhibit the properties which are totally different from its atomic and bulk properties. Due to this they embrace areas of research as broad as engineering, physics, chemistry, material science and molecular biology. The study of these new materials have also been triggered by the availability and development of new instruments and approaches which can give information up to atomic length scales.

Driven by the desire of fabricating new materials with improved and novel properties, nanomaterials and their organizations to form superstructures are studied to perform complex and efficient tasks. The tasks include higher rate of decomposition of pollutants, selective and sensitive response towards a given biomolecule, an improved conversion of light into electrical energy, or more efficient energy and data storage [5, 6].

This thesis is based on the study of growth and structural properties of gold nanoparticles either encapsulated by thiol or organic precursor during their organization at air-water, toluene-water and on solid surfaces to form ultra-thin films.

Grazing Incidence X-ray Scattering (GIXS) techniques have been used extensively for the study along with some other techniques like Atomic Force Microscopy (AFM), Transmission Electron microscopy (TEM), UV-Visible Spectroscopy, Scanning Electron Microscopy (SEM). In the subsequent sections, a brief introduction about Gold nanoparticles, its properties and the studies of ultra-thin films made of them is provided. This introductory chapter is concluded with a brief outline of the thesis.

1.1 Gold Nanoparticles

Gold nanoparticles also known as gold colloids are the most stable metal nanoparticles. Though the form was not known, gold nanoparticles were used extensively in Roman times to make coloured glasses which are still present in stained glass windows of cathedrals throughout Europe . Faraday [7] was the first to recognize that the colour of these glasses was due to the minute size of the gold particles. Gold nanoparticles have been studied extensively in the last two decades due to the exhibition of their size-related electronic, magnetic and optical properties, and applications to catalysis and biology. Though various methods for the preparation of gold nanoparticles have been reported and reviewed [8, 9, 10] earlier but the progress in the last two decades is exceptional after the breakthroughs reported by Schmid [10, 11, 2] and Brust et al [12, 13, 14]. Lots of reviews and books [1, 15, 16, 4] have been published regarding gold nanoparticles soon after these pioneering works.

Exhibition of the unique properties of gold nanoparticles is attributed to the effect of confinement in size. Nanoparticles in the size range of 1-10 nm exhibit electronic structures governed by quantum mechanical rules [17]. The resulting physical properties are neither those of bulk metal nor of molecular compounds, but they strongly depend on the particle size, inter-particle distance, nature of the protecting organic shell, and shape of the nanoparticles [18]. Generally metal nanoparticles are synthesized by bottom-up approach [5] in which ions of a metal are reduced in a solution by a proper reducing agent in the presence of some capping agents. The capping agents get attached to the nanoparticles to prevent them from coalescence. The molar ratio of the metal ions to the capping agents in the solution

decides the nanoparticle size. In general alkane thiols, organic ligands and polymers are used as capping agents. Among the capping agents, alkane-thiols having a -SH group and has an strong affinity towards gold (111) surface are mostly used to stabilize gold nanoparticles.

1.1.1 Electronic Properties

Due to confinement in the size, the de Broglie wavelength of the valence electrons in the nanoparticles approaches the size of the nanoparticles and the nanoparticles start behaving electronically as a zero dimensional quantum dots. Then a gap opens up between the valence band and conduction band unlike the bulk. This band gap has a dependence over size of the nanoparticles and below a certain size (about 20 nm) metal to insulator transitions have been observed. For instance, disordered films of gold nanoparticles reported [19] recently showed metal to insulator transitions. The confinement in the size also decreases the capacitance C of the nanoparticles below 10^{-18} Farad and the single transition of electrons is observed at low temperatures which is termed as Coulomb Blockade. The single electron transitions at low temperatures is due to higher electrostatic charging energy ($e^2/2C$) of the nanoparticles compared to thermal energy (k_BT). Dorogi et al [20] studied films of gold nanoparticles on a thin di-thiol film and showed the evidence single electron transitions through gold nanoparticles using ultra-high vacuum Scanning Tunneling Microscope (STM). In a recent study [21], thin film of gold nanoparticles deposited on a Gadolinium Stearate film were reported to provide rectification behaviour due to spatial asymmetry of the connecting tunnel barriers. Other than these, examples of nanoparticles in many electronic applications are very well reviewed and discussed by Matusui [6].

1.1.2 Optical Properties

Freely mobile electrons in a confined metal nanoparticle show characteristic collective oscillation frequency of the plasma resonance, giving rise to plasmon resonance band (PRB), observed near 530 nm for the size range (5-20 nm) [5,22]. Due to which

a peak is observed in the UV-Visible spectroscopy, known to be plasmon absorption peak, near the wavelength of 530 nm. The absorption characteristics of colloidal gold nanoparticles, in solution or deposited on substrates, are determined by local dielectric environment, size of the particles, inter-particle spacing [23, 24, 25, 26] and chemical nature of interface [27]. The study of the PRB has remained an area of very active research from both scientific and technological standpoints, especially when the nanoparticles are embedded in ionic matrices and glasses [28, 24]. For instance, a driving force for this interest is the application to the photographic process [29]. PRB also provides considerable amount of information about the band structure of metals and has been the subject of extensive research for the optical spectroscopic properties of gold nanoparticles [28, 30].

Apart from PRB, Fluorescence studies of gold nanoparticles have also been carried out under different conditions [31, 32, 33, 34, 35, 36, 37, 38, 39, 40, 41], including femtosecond emission [32] and steady-state investigation of the interaction between thiolate ligands and the gold core [33]. Capping fluorescent groups are pyrenyl [35], polyoctylthiophenyl [37], fluorenyl [41], and other probes [36, 38, 39, 40]. The resonant energy transfer is also observed in fluorescent ligand-capped gold nanoparticles and is of great interest in biophotonics [42].

1.1.3 Magnetic Properties

The confinement in size as well as the increase in the ratio of surface atoms to the total number of atoms in metallic nanoparticles drastically change their properties. This is true for ligand or surfactant protected gold nanoparticles also. Gold in bulk is a well known diamagnetic material but recently magnetic measurements using Superconducting Quantum Interference Device (SQUID) and X-ray Magnetic Circular Dichroism (XMCD) [43, 44, 45, 46] on gold nanoparticles protected with ligands showed the existence of ferromagnetism in them. Till now there is no concrete explanation for the appearance of magnetism in gold nanoparticles below 5 nm but the general belief is the size confinement and attachment of ligands.

1.1.4 Catalytic Properties

Although the catalytic properties of platinum were discovered by Michael Faraday in 1835, and those of the transition metals and their oxides soon after, it has been widely believed until quite recently that gold was too inert to be useful as a catalyst. The paradigm was overturned in the mid-1980s by the work of Masatake Haruta at the Osaka National Research Institute in Japan [47], and Graham Hutchings, then at University of the Witwatersrand in South Africa [48]. Their work showed for the first time that gold can act as an active catalyst provided it is prepared according to some specific recipes. These early endeavours have laid the basis for an ever-expanding study of catalytic gold, and it is now generally (but not universally [49]) accepted that the special property of catalytically active gold is in the size range below 3 nm [50, 51].

1.2 Thin film of nanoparticles

Nanoparticles having unique size dependent properties can act as building blocks of new advanced materials which will have direct applications in micro- or nano-electronics, optoelectronics, chemical and biological sensors and catalysis [10, 52, 53, 54, 17, 55, 5, 56, 16]. Lots of research work is going on around the world to arrange them either in the form of one dimensional array [57, 58] or a thin film of two dimensional array [59, 60, 21, 61, 62, 63, 64, 65, 66, 67, 68] or a three dimensional [69, 70, 71] superstructures in a controlled way. Among the three arrangements, assembly of nanoparticles in the form of ultra-thin film on different substrates and interfaces has been studied extensively due to its direct possible applications. Apart from the experimental observations, understanding of the formation of these structures by complex inter-particle interaction and interaction of the nanoparticles with their external environment has remained a subject of interest.

1.2.1 Thin films at air-water interface

In most of the studies of thin films of organo-metallic nanoparticles, variety of different methods have been developed to deposit them on a substrate. Most of the

techniques utilize, in one way or another, the solubility of these particles in organic solvents or even in aqueous solutions in some cases [4, 55]. When nanoparticles with a protective ligand capping are allowed to spread on the inhomogeneous environment of air-water interface they generally form a very well monolayer known as Langmuir Monolayer [72]. In this approach a dilute solution of nanoparticles in a volatile solvent is prepared and spread over air-water interface. After the evaporation of the solvent the left over nanoparticles form a well-ordered monolayer which can be transferred to a solid substrate either by Langmuir–Blodgett (LB) or Langmuir–Schaeffer techniques [73, 11, 74, 75]. The remarkable feature of this technique is the ability to control the coverage of the nanoparticles on the substrate. With the help of movable barriers the monolayer of the nanoparticles can be compressed before depositing it on a substrate . The studies showed that the monolayer of the gold nanoparticles deposited by this technique showed local hexagonal ordering and depending on the distance between the nanoparticles the assembly found to exhibit interesting collective behaviour [76, 77, 78, 61, 21, 79]. This technique has also been extended further to deposit multilayer of nanoparticle by collapsing the monolayer. Studies revealed [77, 78, 61] that the collapsed film is not as well ordered as the monolayer but the understanding of the collapse is still lacking. Though this technique provides a control over the surface coverage of nanoparticles but a recent study [80] showed that one cannot increase the surface coverage of the monolayer of the nanoparticles beyond 60% by just compressing and transferring it on to a substrate. The reason behind this 60% monolayer coveraged is also not well understood. A chapter of this thesis is devoted to discuss our detail study on the structure of monolayer of preformed thiol encapsulated gold nanoparticles on air-water interface under different conditions of temperatures and surface pressures. We showed that the monolayer of the gold nanoparticles undergoes through a buckled structural phase before the collapse and the monolayer can either be annealed or decompressed to get rid of the buckled structure.

1.2.2 Thin films on Solid Surfaces

The simplest approach of depositing nanoparticles directly from a solution onto a solid substrate is either by allowing drops to wet and evaporate on the substrate or by dipping the substrate in the solution to allow nanoparticles to self-assemble at the interface [81, 82, 83, 69, 84, 54, 85, 67, 68, 86, 87]. Though the technique is simple but the results i.e the two dimensional ordering and patterns formed by the nanoparticles are interesting systems to understand. The interplay between the interactions of inter-nanoparticle, nanoparticle-solvent, nanoparticle-substrate, solvent-substrate and dynamics of solvent evaporation lead to numerous variety of patterns and structural transitions.

Structural phase transitions in solids proceeds via complicated phases covering a range of stable and meta-stable configurations [88]. Detailed investigations have revealed that the thermodynamic properties guiding the evolution and phase stability of nanostructures are distinctly different from their bulk counterparts [89]. Colloidal nanosystems like nanoparticles are prone to structural phase-transitions under the influence of external parameters like temperature [90, 91], confinement [88, 92, 93], shear [94, 95], electrical and magnetic fields [96, 97, 98] and provide viable routes to visualize and study the ordering and dynamics of structural transitions in 2D using state-of-the-art techniques like scattering and microscopy. Sequence of structural transformation from n$\triangle \rightarrow$(n+1)$\square \rightarrow$ (n+1)$\triangle$, of such colloidal systems when trapped within optically flat surfaces have been observed with increasing separation between the surfaces [99, 100]. Here n is the number of layers and $\triangle$ and $\square$ are layers corresponding to triangular and square symmetry respectively.

The pattern formation becomes much more complex when the nanoparticles are deposited on soft solid substrates like polymer films [101, 102, 103, 104, 105, 106, 107]. The presence of macromolecules like polymers in the vicinity of nanoparticles changes the environment of nanoparticles inducing interactions amongst them [101, 102]. These complex interactions induce both in-plane and out-of-plane diffusion of nanoparticles which are not understood properly.

1.2.3 Thin films at liquid-liquid interfaces

Another interesting approach to form thin films of metal-organic nanoparticles is to make use of an interface between two immiscible liquids [108, 109, 110, 111, 63, 64, 65, 66]. This approach can be used in two different ways. In the first one, by proper choice of capping ligands of preformed nanoparticles and the immiscible liquids, it is possible to spontaneously arrest the nanoparticles at the interface and then transfer them on to a substrate [108, 109, 110]. While in the second one, it is possible to form metal-organic nanoparticles at the interface between the liquids by a reduction reaction between reacting species present in both the liquids [64, 65, 66]. In both the cases the interplay between the interfacial energy and thermal fluctuations govern the ordering and structure of the films at the interface. The evidence of this interplay is very much manifested in the formation of larger gold nanoparticles with increase in temperature of the liquids [66]. It is well known that bare liquid interfaces have a long range order characterized by thermally excited capillary waves [112,113,114,115]. But microscopic structure of liquid interfaces, during transfer of ions across them, studied by extensive numerical simulations suggested [116] the formation 'finger' like protrusions of size about 1 nm which last for tens of picoseconds. The later approach being more complex due to the formation of gold nanoparticles by transfer of ions across the interface followed by reduction. Till date the experiments performed to study the interfacial films by reduction reaction are based on Transmission Electron Microscopy and other measurements on the transferred films. The in-situ studies of the formation of these interfacial films by reduction reaction, which can provide us not only the structure of the films but also improve out understanding of interfacial reactions and its dependence on interfacial tension, are still rare in the literature. A detailed studies on the formation and ordering of gold nanoparticles at toluene-water interface by a reduction reaction is also presented in a chapter of this thesis. The results show the formation of 1.3 nm gold nanoparticles at the toluene-water interface just after the reaction and these gold nanoparticles self-assemble spontaneously to form 13 member aggregates in the absence of external vibrations. The presence of external mechanical vibrations increases the rate of reaction to form aggregates having fractal dimension of 2

indicating disc like structures.

1.3 GIXS technique

X-rays are electromagnetic waves having wavelengths in the range of 0.01 to 100 Å and can be generated either by tube sources in laboratories or huge Synchrotron sources. After the discovery of X-rays in 1986 by Rontgen and pioneering works by Max von Laue, W. H and W. L. Bragg and P. P. Ewald on X-ray Diffraction from solids, X-ray scattering become a strong tool for structural determination of materials. In X-ray scattering technique, a well collimated (monochromatic or White) X-ray beam is allowed to scatter from a sample of interest and the scattered X-ray beam is collected by a detector. With a monochromatic beam the scattered intensities are measured as function of scattering angle and the technique is termed as Angular Dispersive while the technique, using white beam and the measurements are performed as a function of energy keeping the scattering angle fixed, is termed as Energy dispersive. In both the techniques the effective wavelength is varied and depending upon the structure of the sample there is an interference pattern observed in the scattered X-rays. Angular Dispersive technique is widely used due to its high resolution while Energy dispersive technique, due to fast data collection rate, is generally used for studying structural dynamics of a system. The advantage of X-ray scattering technique over other techniques are that it is non-destructive, gives very well statistically averaged information about the structure and it is the only technique to provide structural information about buried interfaces.

Thin films of materials, their surfaces and interfaces have been studied extensively during the last few decades. Though the direct measurements techniques like Atomic Force Microscopy (AFM), Scanning Electron Microscopy, Transmission Electron Microscopy (TEM) have been developed to produce the images of them in the atomic level resolutions but the structural studies of thin films, buried surfaces and interfaces are only possible by X-ray scattering measurements. For the study of thin film of materials like nanoparticles in which the characteristic length scales (nanoparticle size) are much higher than the atomic length scales, the scattering measure-

ments in the Grazing incidence geometry is required. Grazing incidence geometry makes the X-rays sensitive to the interfacial structure by its low penetration depth below the critical angle and plays a crucial role for studying structure and ordering of interfacial films [117,118,113,75,61,115,119,110,120,121,114,112,122,123,124,125]. The Grazing incidence techniques, which are extensively used for our measurements and presented in this thesis are Specular X-ray Reflectivity (XRR), Grazing Incidence Diffraction (GID), Grazing Incidence X-ray Off-Specular scattering (GIXOS), Grazing Incidence Small Angle X-ray Scattering (GISAXS).

In order to extract information from the scattering data collected by using these technique one needs to have proper theoretical formalism and modeling. The details of the theoretical formalism which are needed to study the growth and structural properties of thin films at the interfaces are discussed in Chapter 3.

1.4 Outline of Thesis

This thesis is based on our new experimental findings to address growth, ordering and structural properties of thin films of gold nanoparticles different surfaces and interfaces as discussed above. Some of the results are already published in International Journals. Grazing incidence X-ray scattering technique is mainly employed with the laboratory rotating anode source at Surface Physics Division (SPD), Saha Institute of Nuclear Physics (SINP), India to study the films at solid interfaces and various Synchrotron sources namely European Synchrotron Radiation Facility (ESRF), France, Advanced Photon Source (APS) and National Synchrotron Light Source (NSLS) both in USA. This thesis has six chapters excluding Introduction.

Second Chapter is devoted to the brief description of all the experimental techniques starting from preparation of thiol passivated gold nanoparticles, its size determination and instruments involved for the experiments performed. Since X-ray scattering has been the main tool of our experiments we have presented a detailed description about X-ray sources and instruments used. In the Third chapter, theoretical formalism of GIXS technique used in this thesis is presented.

Fourth chapter addresses the structure and ordering of monolayer of dodecanethiol

passivated gold nanoparticles of two different sizes on air-water interfaces studied by GIXS technique. The experiments on the gold nanoparticles with gold-core size just below 2 nm are carried out at ESRF, France, while that of size above 2 nm at APS, USA. Our main aim of this study is to understand the ordering of nanoparticle of different sizes up to the collapse of the monolayer and has not been done to the best of our knowledge. The results show that gold nanoparticles below 2 nm exhibit reversible buckling under compression-decompression cycles before the monolayer collapses to form bilayer. While gold nanoparticles of size above 2 nm do not show reversible buckling.

In this thesis, the Fifth Chapter is devoted to address the two basic phenomena which occur in the monolayer of thiol encapsulated gold nanoparticles when transferred to a solid substrate from air-water interface and by spin casting them on a surface of a thin polymer film respectively. We observed that when a monolayer of gold nanoparticles is transferred from a liquid surface it undergoes a phase transformation from closed-pack hexagonal to square lattice as a function of time. When the nanoparticles are deposited on a thin film of Polyacrylamide a continuous change in the monolayer structure is observed due to both in-plane and out-of-plane diffusion. The diffusion mechanism attributed to the movement of the nanoparticles inside the polymer film is found to be Non-Fickian.

In the Sixth Chapter, in-situ studies of formation of Gold nanoparticles at toluene-water interface by an interfacial reaction, its ordering and structural properties are discussed. The studies reveal that the gold nanoparticles formed at the toluene-water interface due to reduction reaction having gold-core of size 1.3 nm with an organic capping of 0.5 nm. The gold core size is shown to be independent of the presence of macroscopic fluctuations at the interface while the thickness of the film is dependent on it. Studies also show that the films formed in the presence of macroscopic fluctuations composed of fractal aggregates of 1.3 nm gold nanoparticles.

Chapter 2

Experimental Techniques

The search of new materials and their properties demand the development of new, efficient techniques for their preparation and measurement of properties. This chapter is devoted to the experimental techniques which were used for preparing the gold nanoparticles and to study the growth and structure of films of nanoparticles on solid substrates, at air-water and toluene-water interfaces.

2.1 Preparation of Gold nanoparticles

The reduction of gold (III) derivatives is the conventional method of preparing gold nanoparticles. Till now many methods [5] have been introduced to reduce gold ions to form gold nanoparticles. In the year 1951, Turkevitch [8] introduced a method of preparing 20 nm gold nanoparticles by reducing AuHCl4 by citrate in water. Schmid's cluster $[Au_{55}(PPh_3)_{12}C_{16}]$, reported in 1981, long remained unique with its narrow dispersity (1.4±0.4 nm) for the study of a quantum-dot nanomaterial, despite its delicate synthesis [126]. Later in the year 1994, Brust et al introduced a phase transfer method [13, 14] which made a considerable impact in the field of nanoparticle synthesis. The method involved transfer of gold ions to an organic phase followed by reduction reaction in the presence of capping agent like alkane thiols. The alkane thiols have a strong affinity towards the newly formed gold nanoparticles by reduction reaction and get attached to their surfaces to restrict their further growth. Due to this property of alkane thiols one can have control over

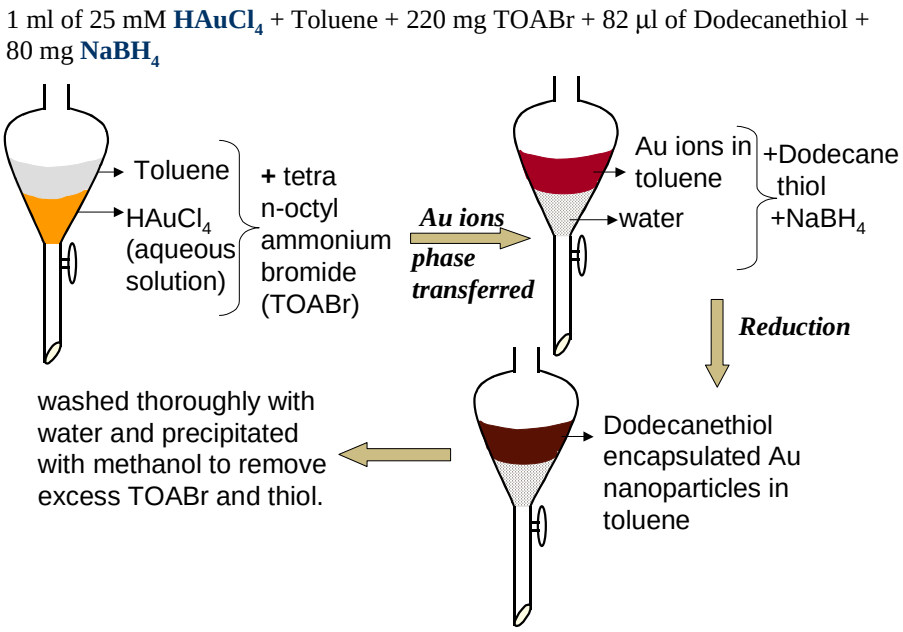

Figure 2.1: Schematics of preparation of thiol encapsulated-Gold nanoparticles by Brust Method.

the size of nanoparticles by changing the molar ratio of gold to thiol. We used the same technique to prepare the gold nanoparticles for our experiments.

A schematics of the preparation method of gold nanoparticles is shown in Figure 2.1. In a typical preparation we took 1 mL of 25 mM aqueous solution (yellow in color) of $HAuCl_4$ (Hydrogen tetrachloroaurate) in a volumetric flask and 5 mL toluene. Then we added the well known phase transfer reagent Tetra-octyl Ammonium Bromide (TOABr) and shaken the flask vigorously. After shaking the flask for about 1 minute the transparent toluene layer became light brown in color due to transfer of Gold ions from the aqueous layer to the toluene layer. Before adding the reducing agent, the solution was shaken after adding 82 µL of Dodecanethiol due to the toluene layer becomes milky in colour. Then 5 mL aqueous solution of 80 mg of $NaBH_4$ (Sodium Borohydride) is added as a reducing agent with rapid shaking to produce dark brown colour toluene solution. Then the solution containing newly formed gold nanoparticles are thoroughly washed with water and precipitated with excess of Methanol. The precipitated gold nanoparticles are then filtered filter paper

of pore size 0.45 μm and stored on it for using it for experiments. All the chemicals used were freshly ordered from Aldrich, USA. We prepared gold nanoparticles of two different core sizes by taking two molar ratios of Gold to Dodecanethiol (Au:Thiol) viz 3:1 and 6:1 . In order to use the nanoparticles for experiments firstly a section of the filter paper was first weighed and then dipped into measured amount of toluene. Then the left over filter paper after the transfer of nanoparticles from the surface of the filter paper to the solution is again weighed to calculate the density of the solution.

2.2 Determination of size of the Nanoparticles

Before doing any experiment with the nanoparticles so prepared it is important to determine the size and distribution of the nanoparticle which we prepared. For this purpose we performed two measurements as

- UV-Visible Absorption Spectroscopy and
- Transmission Electron Microscopy.

2.2.1 UV-Visible Absorption Spectroscopy

The spectroscopy of photons in the UV-visible region is termed as UV-Visible absorption spectroscopy. It uses light in the visible and adjacent (near ultraviolet (UV) and near infrared (NIR)) ranges. This technique is employed to characterize nanoparticles, the basic idea being the fact that there exists a strong band in the visible region of the absorption spectra of noble metal nanoparticles arising from the surface plasmons in response to an external electromagnetic field [127, 86]. It has been observed that as the nanoparticle size decreases there is dramatic increase in the plasmon resonance bandwidth which may be accompanied by shifts in the resonance position. The intensity is however proportional to the metal concentration. This necessitate the introduction of size dependent dielectric constant, at least for free electron metals, when the particle diameter (a) becomes smaller that the electron mean free path (l) in the bulk metal. We used this technique to observe

the Plasmon modes of the Gold nanoparticles and determine their sizes. For $a < l$, the electrons are scattered by the surface, strongly affecting their response to the incident electromagnetic field. This results a inversely proportional dependence of the plasmon bandwidth on particle diameter [128, 129]. In fact, for particle diameters substantially smaller than a wavelength of light, samples prepared without a matrix generally appear to be black. The size of spherical metallic nanoparticles can be obtained from the width of its absorption peak i.e a Lorentzian and is given by [130]

$$\Gamma = \frac{2\nu_F}{a} \tag{2.1}$$

where Γ is the Full-Width at Half-Maximum (FWHM) of the absorption spectrum near the surface plasmon peak, υ_F is the Fermi velocity of the metal. It is assumed here that the particles are spherical in shape.

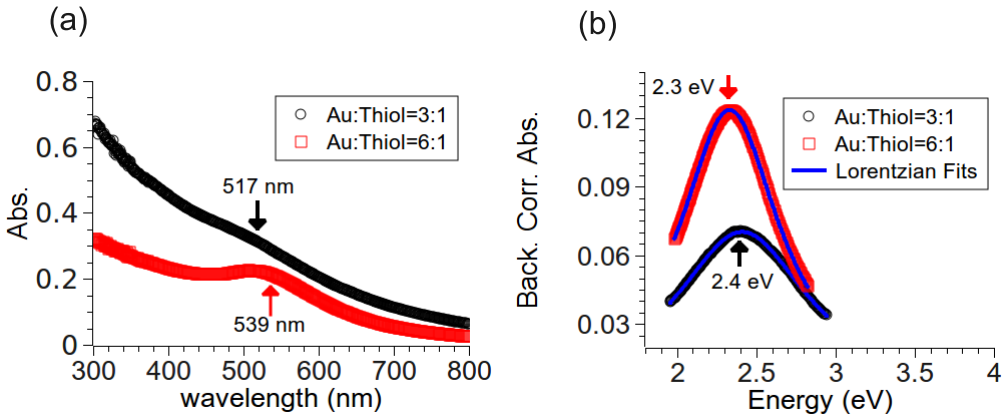

Figure 2.2: (a) Variation of Absorption of the gold nanoparticles as a function of wavelength. (b) Linear Background corrected plasmon absorption peaks as a function of energy. The peak positions corresponding to wavelengths and energies are marked in the plots by vertical arrows.

We performed our measurements on a dilute solutions of the nanoparticles using GBC UV-Visible Cintra 10_e Spectrometer, Australia (Shown in Figure) of Surface Physics Division(SPD), Saha Institute of Nuclear Physics (SINP), India, in transmission mode to determine the size of them. The scan range used for our measurements was 300-800 nm with a Tungsten-Iodine lamp. A Czerny-Turner monochromator was

used to select the precise wavelength of interest and Silicon photo diode was used as the detector. Figure 2.2 (a) shows the UV-Visible absorption plots for two nanoparticles prepared with Au:Thiol ratio 3:1 (Black Circles) and 6:1 (Red Squares) as a function of wavelengths (λ). The presence of weak plasmon peak around 516 nm for the nanoparticles prepared with Au:Thiol=3:1 compared to the peak at 540 nm for Au:Thiol=6:1 indicates reduction of core size with low Au:Thiol ratio. In order to know calculate the average size of the nanoparticles we have subtracted a linear background around the plasmon peaks and plotted them as a function of energies (hc/λ, h being the Planck's constant and c the speed of light) in eV shown in 2.2 (b). We fitted the curve with a Lorentzian to know the width 'Γ' and calculated the the size of the nanoparticles 'a' from Equation 2.1. We obtained the gold-core size of the nanoparticles prepared with Au:Thiol ratio 3:1 as 1.8±0.1 nm and with 6:1 as 2.4±0.2 nm.

2.2.2 Transmission Electron Microscopy

Transmission electron microscopy (TEM) is a microscopy technique [131] whereby a highly accelerated beam of electrons with energies ($>$ 100 keV and higher) is transmitted through an ultra thin specimen, interacting with the specimen as it passes through. An image is formed from the interaction of the electrons transmitted through the specimen; the image is magnified and focused onto an imaging device, such as a fluorescent screen, on a layer of photographic film, or to be detected by a sensor such as a CCD camera. The working principle of the imaging system in transmission electron microscopy (TEM) is sketched in Figure 2.3. The lens system used in TEM is the same as in an inverted light microscope with two differences, namely, the use of electromagnetic lenses to focus the electron beam instead of glass lenses and the use of an electronic gun instead of an incandescent lamp. Focusing of the electron beam is done by varying the magnetic field of electromagnetic lenses. The electron beam is concentrated by the use of one or two condenser lenses. An objective lens initially magnifies the image which is further enlarged by the use of one or more projector lenses in the same way the eye-piece lens does in a light microscope. The greatest advantages that TEM offers are the high magnification ranging from

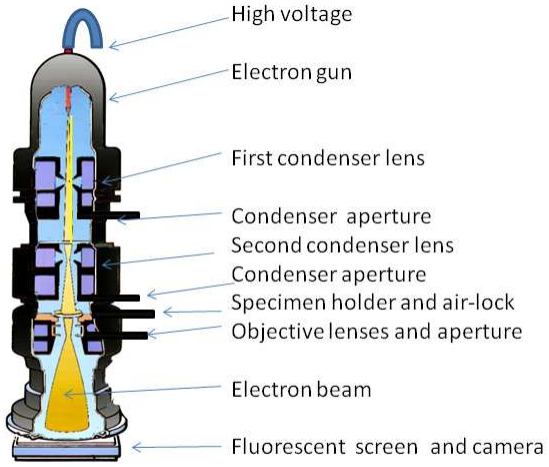

Figure 2.3: Schematics of a Transmission Electron Microscope.

50 to 10^6 and its ability to provide both image and diffraction information from a single sample.

The high magnification or resolution of all TEM is a result of the small effective electrons wavelength 'λ' which is given by the de Broglie relationship

$$\lambda = \frac{h}{\sqrt{2mqV}} \tag{2.2}$$

where m and q are the electron mass and charge, h is Planck's constant, and V is the potential difference through which electrons are accelerated.

We used JEOL-JEM 2010 Transmission Electron Microscope at Indian Association for the Cultivation of Science, India, operated at 200 kV for measuring the particle size of the Dodecanethiol encapsulated gold nanoparticles as discussed in Section 2.1 on page 12. We prepared a dilute solution of the gold nanoparticles in toluene and put few microlitres of the it on a Carbon-coated Copper grid and allowed to dry under a lamp. The TEM micrograph of the nanoparticles obtained with Au:Thiol ratio 3:1 and 6:1 are shown in Figure 2.4 on the next page (a) and (b) respectively. For the determination and particle size distribution we have used a Image processing software namely ImageJ available under public domain at *http://rsb.info.nih.gov/ij/*. The particle size distribution for the corresponding ratios are shown in Figure 2.4(c) & (d). The distribution show that the particle

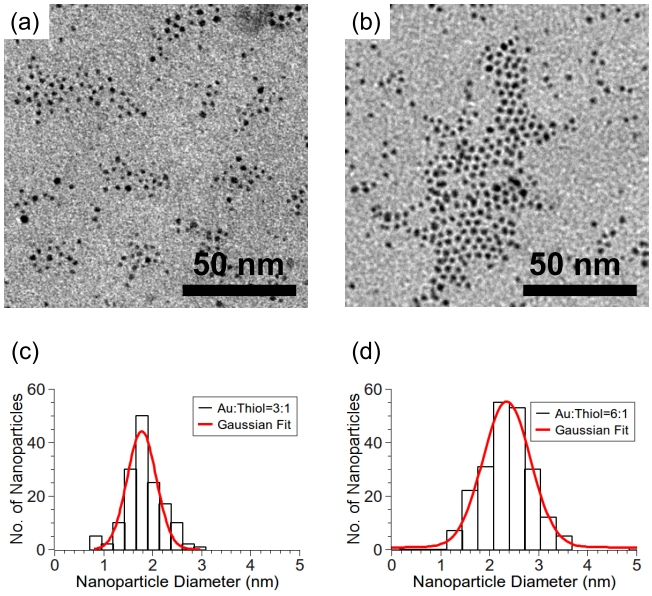

Figure 2.4: TEM micrograph of Nanoparticles prepared with Au:Thiol ratio (a) 3:1 and (b) 6:1. The corresponding Particle size distributions are shown in (c) & (d) respectively.

size obtained by the ratio (AU:Thiol) of 3:1 has a narrow distribution with average diameter 1.8 nm while that with 6:1 is 2.4 nm. This matches very well with our previous findings with UV-Visible spectroscopy measurements.

2.3 Preparation of Thin films of Nanoparticles

2.3.1 Spin Coating

Spin coating [132] is the most easy and widely used technique nowadays for depositing thin uniform films of materials, which can be easily dissolved in a volatile liquid, on a solid flat substrate within very short time. Polymers, Micro-emulsions and Nanoparticles well dispersed in a volatile liquids are most common materials which are deposited by Spin Coating. In this simple technique, first the material to be deposited is added to a volatile solvent to form a solution and then few drops of the solution (according to the substrate dimension) are placed on the solid substrate. Depending on the wettability of the substrate, the solution can flow to form a meta-stable continuous film or form a droplet on the surface. The substrate is placed on a vacuum chuck, which is connected to a pump. As soon as the pump

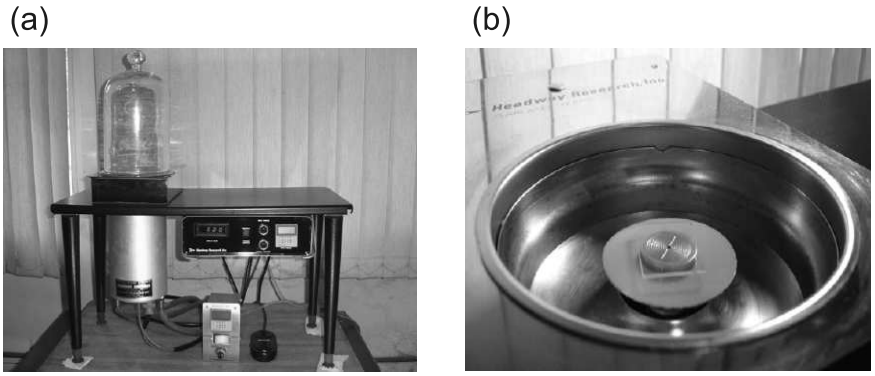

Figure 2.5: (a) The Spin Coater at SPD, SINP. (b) The vacuum chuck on which the substrates are placed (a glass slide is shown for example).

is on, the substrate is hold by the chuck and by spinning the substrate with very high speed (more than thousands of rotations per minute) the solution is forced to spread throughout the substrate. The direction of flowing of the solution is outward from the center of the substrate due to the centrifugal force. Eventually, the solvent evaporates making a thin film and the viscosity of the solution increases. Ultimately, the spinner is stopped and depending on the rotation speed and the concentration of the solution used for spinning, we get a film of uniform thickness within few seconds. The films should be kept in a desiccator or in some vacuum arrangement so that the residual solvent goes out.

We have used the spin coater from Headway Research Inc., USA, Model–EC101 (shown Figure 2.5) at SPD, SINP, India, to deposit Gold nanoparticles and Polymer namely Polyacrylamide (Molecular weight $\sim 5\times10^6$ and Radius of gyration, $R_g \sim 80$ nm) on Si (100) substrates like Silicon. Details of the deposition are discussed in Chapter 5.

2.3.2 Langmuir-Blodgett (LB) Deposition Technique

LB deposition technique [117] is generally used to study and deposit monolayers of 'Amphiphile' molecules like long chain fatty acids having hydrophobic tail and hydrophilic head groups on solid substrates. This method make use of clean water surface on which a solution of desired amphiphile in a suitable volatile solvent (insoluble in water) is spread. The solvent evaporates out within few minutes and

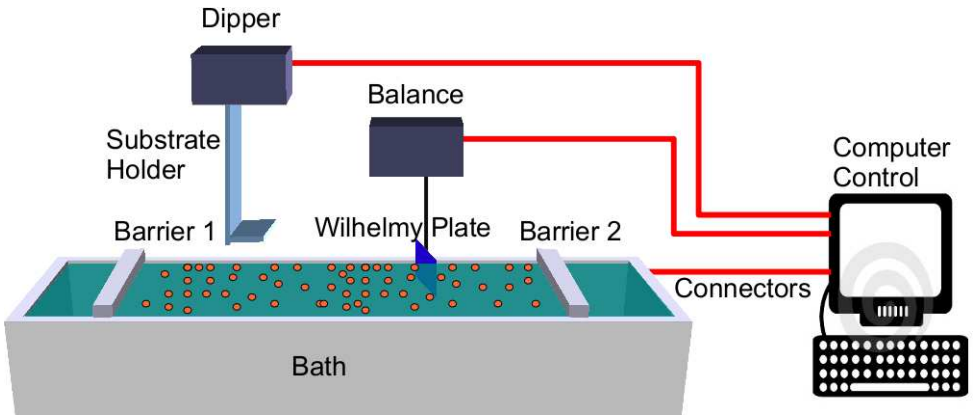

Figure 2.6: Schematics of LB deposition System.

the left over molecules on the water surface form a monolayer of molecules which is termed as Langmuir monolayer after the pioneering work of Irving Langmuir [72]. The first study on a deposition of multilayer of long chain carboxylic acid onto a solid substrate was carried out by Blodgett [133, 134]and this started the field of LB film deposition.The most important property of the Langmuir monolayer is its surface tension. In studies of these monolayer films, one measures the difference in surface tensions between a clean or pure liquid (denoted as the subphase) surface and that covered by the film. Langmuir first pointed out the analogy between the surface tension differential and the force or pressure exerted by the film [72]. The surface pressure, Π, is defined as,

$$\Pi = \gamma_o - \gamma, \tag{2.3}$$

where γ_o is the surface tension of the pure liquid and γ the surface tension of the film covered surface.

The instrument which is used to prepare the Langmuir monolayer and subsequently deposit the LB films is called a trough. The trough has undergone several modifications since the first one developed by Agnes Pockels. The modern day troughs are fully computerized with state-of-the-electronics involved in the design. Figure 2.6 shows the schematic of a single bath trough. The essential elements of a trough are (a) the bath, usually made of a hydrophobic material like Teflon (PTFE), (b) the mobile barriers for controlling the area and hence pressure of the monolayer,

(c) a balance that measures the surface pressure and (d) a dipper for dipping the substrate in the monolayer. In all the commercially available troughs there is a provision in the bath to increase the temperature of the liquid by flowing hot or cold water through the bath. This helps to do temperature study defined by the temperature range of the liquid used.

We have used KSV 5000 alternating trough of SPD, SINP, India, for depositing monolayer films of thiol encapsulated gold nanoparticles on Silicon substrates at particular surface pressures and temperatures. Before the deposition the substrate has been chemically treated with ammonia (NH_4OH) and hydrogen peroxide (H_2O_2) solution (NH_4OH:H_2O_2:H_2O = 1:1:2) to make the surface hydrophilic. This Method of treating substrates is known as RCA cleaning [135, 136]. Hydrophilic silicon substrates were then kept horizontally in a homemade L-shaped Teflon substrate holder which is attached to the clip of the trough dipper. The substrate holder thus can be moved up and down with desired speed. At the time of film deposition water surface was properly cleaned and the L-shaped substrate holder was immersed into the water so that the substrate was kept parallel to water surface and 10 mm below the air-water interface. Transfer onto Si (100) were done at room temperature, with the substrate moving upwards at the rate of 0.5 mm/min, in this modified inverse Langmuir-Schaefer method [74, 75]. Details of the deposition conditions are discussed in the corresponding chapters. Other than deposition we have used single trough mounted on the Goniometer in the beamlines ID10B and 15IDC of Synchrotron Sources at European Synchrotron Radiation Facility (ESRF), France, and Advanced Photon Source (APS), Argonne National Laboratory (ANL), USA.

2.4 X-ray Scattering Measurements

Since the discovery of X-rays in 1896 by W. C. Roentgen [137], it has been used extensively as a probe of the structure of matter. X-rays are electromagnetic waves with wavelengths in the range of 10 to 0.001 nanometers, corresponding to frequencies in the range 30 petahertz to 30 exahertz (30×10^{15} Hz to 30×10^{18} Hz) and energies in the range 120 eV to 120 keV. Till the mid 1970, X-ray tubes were only

used as X-ray sources in which X-rays are generated by bombarding high energy electrons on a suitable target material like Copper (Cu), Molybdenum (Mo) etc. In mid 1970s it was realized that the synchrotron radiation emitted from charged particles circulating in storage rings constructed for high energy nuclear physics experiments was potentially a much more intense and versatile source of X-rays. Indeed synchrotrons have proved to be such vastly better source that many storage rings have been constructed around the world dedicated solely to the production of X-rays.

2.4.1 X-ray Tube Sources

After the discovery of X-rays in 1985, the first X-ray tube to be used as a standard X-ray source was developed by W. D. Coolidge in 1912. A typical X-ray tube (shown in Figure 2.7 on the following page) consists of a filament or cathode made of Tungsten to produce electrons which are focused and accelerated by applying a high voltage between cathode and anode. The anode is generally coated with a metal like Copper (Cu), Molybdenum (Mo), etc. depending upon the requirement of wavelength of X-rays to be generated. The point where the electron beam strikes the anode is called the focal spot. Most of the kinetic energy of the electrons after bombardment with anode is converted to heat and only about 1% of the energy is converted into X-ray. The heat generated during the bombardment is dissipated by keeping the anode in contact with circulating coolant like cold water. This generation of heat at anode and efficiency of cooling restrict the power of the X-ray tube around 1 kW. A further improvement in the power was achieved when a rotating anode (shown in Figure 2.7 on the next page) was used instead of fixed anode. A rotating anode can dissipate heat over a larger volume compared to fixed one. The technical difficulties like problem of maintaining high vacuum seal on the rotating shaft of anode took some time to settle and only after 1960's rotating anode X-ray sources could be available on commercial basis.

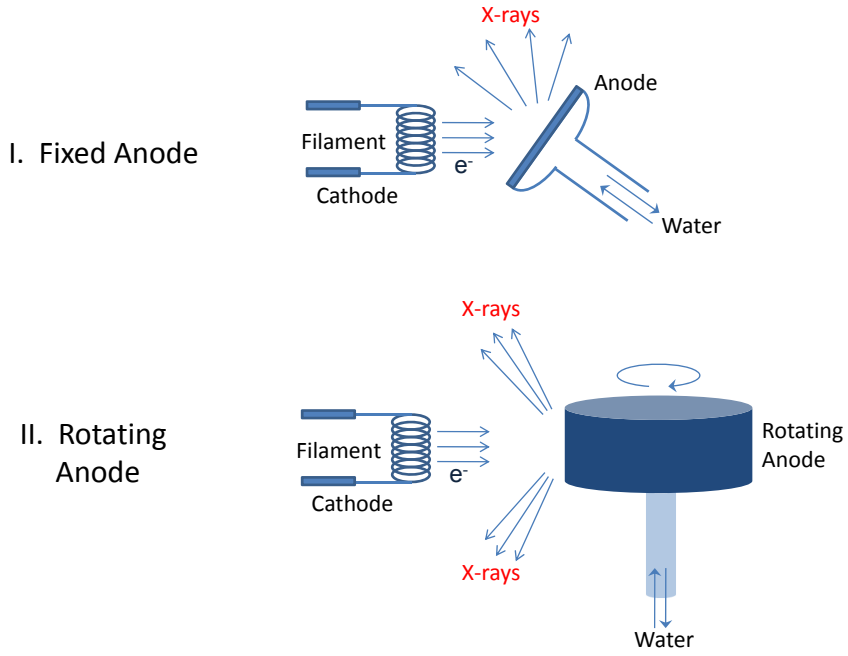

Figure 2.7: Schematics of Fixed and Rotating Anode X-ray tubes.

X-rays produced from bombardment of electrons on anode consist of two distinct components depending the nature interaction of electrons with anode material. There is a continuous part due to the electrons being decelerated, and eventually stopped in the metal. This is known as bremsstrahlung radiation and has maximum energy that corresponds to the high voltage applied to the tube.

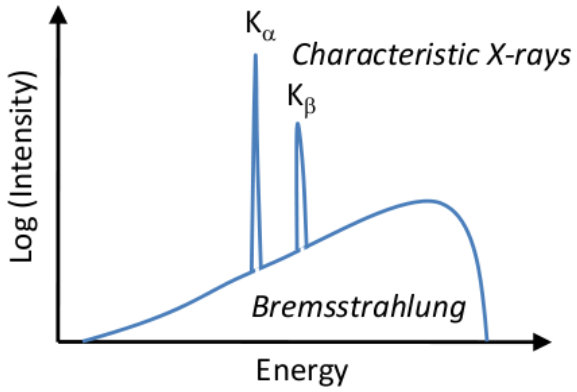

Figure 2.8: The X-ray spectrum from a anode material showing a continuous *bremsstrahlung* and *characteristic* X-ray peaks $K_\alpha$and K_β.

During collision of a high energy electron with an atom of the anode, an electron from inner shells of the atom can be knocked off creating a vacancy. The sponta-

neous relaxation of an electron from an outer shell into the vacancy produces an X-ray photon with a characteristic energy equal to the difference between the energies of the shells. These characteristic energy peaks superimposed on continuous bremsstrahlung give the total spectrum of X-rays (shown in Figure 2.8 on the preceding page) emitted from that particular anode material. The experiments with monochromatic beam utilize the K lines of the anode material which is several orders of magnitude more intense than bremsstrahlung spectrum.

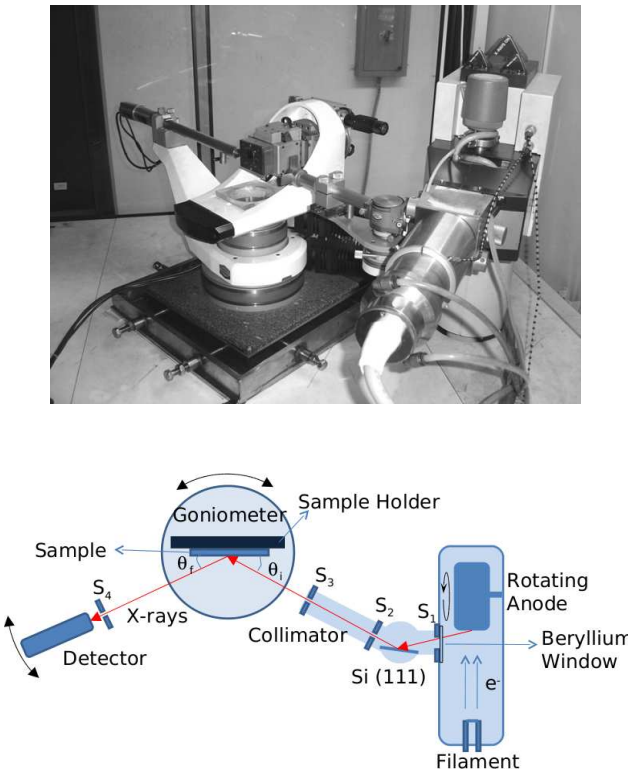

Figure 2.9: Rotating anode X-ray set up of our laboratory and its schematics.

2.4.1.1 Rotating Anode source in our laboratory

The x-ray scattering experiments, which we performed in the laboratory of SPD, SINP, India, are done using 18 kW Rotating anode X-ray generator FR591 with Copper anode from Enraf Nonius, Germany (shown in Figure 2.9), operated at 55 kV and 70 mA corresponding to 4 kW power in fine focus mode. The schematics of the X-ray measurement setup is also shown in Figure 2.9 along with the laboratory set up. The Cu rotating anode and cathode assembly are placed inside a vacuum chamber maintained at high vacuum ($\sim 10^{-7}$ millibar) with the help of a turbo

pump backed by another rotary pump. The anode is cylindrical in cross-sectional view and its shaft also rotates co-axially inside another cylinder containing ferrofluid. The ferrofluid serves the purpose of vacuum seal as well as the lubricant. The anode is water-cooled and it can rotate with very high speed, typically at the speed of 4000 RPM at full power of the instrument. The cathode part consists of a high voltage cable receptable connector, metal body having a ceramic nose piece and focus assembly. The whole cathode is insulated and cooled by oil flow all the time. The filament and other important equipments are associated with the focus assembly. Electrons, produced from the filament are accelerated by the voltage between anode and filament and directly hits the anode. The axis of electron beam is at 90° angle with the axis of rotation of the rotating anode. In this instrument, we have both broad focus and fine focus types of filaments. For broad focus, a distance of 9 cm is fixed between the anode and the filament that produces 0.5 × 10 mm^2 electron beam. But in case of fine focus, the electron beam cross-section is 0.3 × 3.0 mm^2 keeping 10 cm distance from filament to anode. The powers dissipated are 18 kW and 4 kW for broad focus and fine focus set up respectively.

The X-rays generated in the vacuum chamber from the Cu rotating anode is allowed to incident on a Silicon (111) single crystal monochromator through a Beryllium Window S_1 and Cu-K_α is only selected by eliminating Cu-K_β with an adjustable horizontal slit S_2 adjacent to the monochromator and Cu-$K_{\alpha 2}$ with a pair of horizontal and vertical slits S_3 of width 100 μm and 5000 μm respectively.

2.4.1.2 Goniometer

For the X-ray scattering measurements from solid surfaces the samples are vertically on a triple axis goniometer (Micro-controller Inc.) head of SPD, SINP, India. Both translational and angular movements are possible using different stepper motors of the goniometer. As the direction of incoming x-ray beam is fixed, the angle of incidence (θ_i) on the sample is controlled by changing the angle of the goniometer head with respect to the beam direction. The scattered beam is collected by the detector mounted on the 2θ arm of the goniometer. Both the θ and 2θ motors are mounted co-axially. The typical distance of monochromator to goniometer centre and from

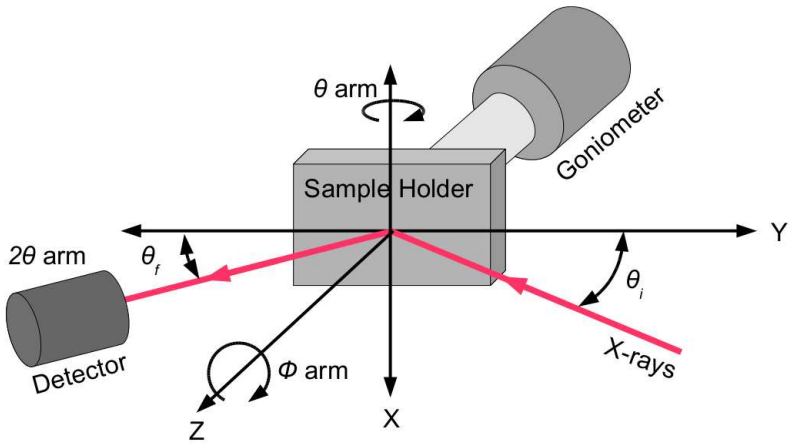

Figure 2.10: Movements of Goniometer.

this centre to the detector is 40 cm. Movements of the goniometer is indicated in Figure 2.10. The goniometer is equipped with Z-motor to control translational movements along Z-axis, the θ_X and θ_Y motors for rotations along X-axis and Y-axis respectively and another Φ motor about Z-axis. There are separate microprocessors for all the θ, 2θ and Φ movements and also we can control the motor movements from control panel.

2.4.1.3 The Detector

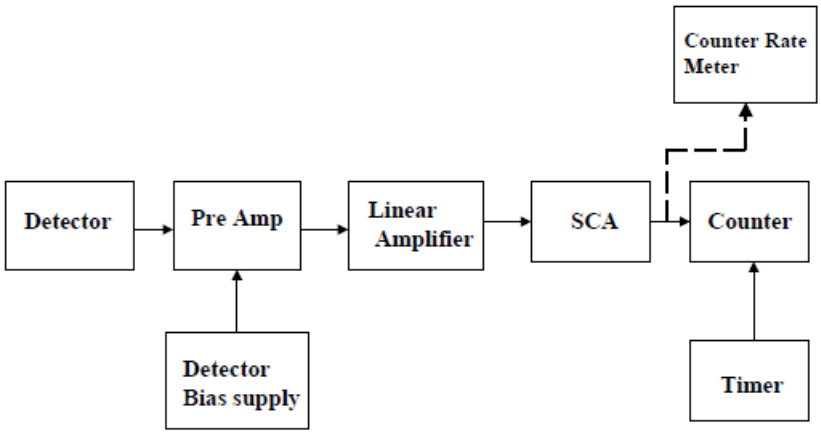

Figure 2.11: Schematic of signal chain from detector to counter in our laboratory set up where we have indicated different labels.

In our laboratory at SPD, SINP, India we use NaI scintillation detector for detecting scattered X-rays from the samples. The detector signals are processed by by

standard linear electronics consisting of photomultiplier tube (PMT), a preamplifier followed by a linear amplifier and a single channel analyzer (SCA). We have shown a schematic of the above sequence from detector to counter in Figure 2.11. The detector picks up signals coming from the sample and each incident photon generates optical pulses with a certain amplitude that is proportional to that particular photon. The rise time of the pulse has very short compared to the fall time. The light pulses are incident onto the photo-cathode of PMT and photo-electrons are generated. These photo-electrons are subsequently reflected off the dynodes producing secondary electrons. Finally we get a magnified signal at the anode of PMT. The output of the detector is fed to a preamplifier circuit [138] having larger time constant than the charge collection time of the detector to acquire the whole charge. The purpose of having the preamplifier circuit is that it minimizes the capacitive load on the detector giving better signal-to-noise ratio. The linear tail pulses from the preamplifier may result the pulse pileup problem and one need to shape the pulses [138] to reduce the tail without loosing pulse amplitude. So the preamplifier output is feed through a linear shaping amplifier that amplify and shape the coming signals. To convert the linear pulse to a logic pulse, a differential discriminator or single channel analyzer (SCA) is used. If the input linear pulse lies between a window of certain amplitude, then only we get a logic output pulse for counting purpose. In our X-ray scattering set up, we have selected a Lower Level Discriminator (LLD) and a window to select only the $CuK_{\alpha 1}$ line and to optimize the signal-to-noise ratio accordingly. We have another evacuated collimator tube between the detector and the sample stage and overall we have a background around 0.25 counts/sec.

Usually, three different types of scans are performed in grazing incidence x-ray reflectivity studies—specular reflectivity scan, transverse diffuse scan and longitudinal off-specular scan [117]. In specular scans the scattered intensities are measured as a function of scattering angle keeping equal incident and scattered angles ($\theta_i = \theta_f = \theta$) of x-ray beam with sample surface normal. In diffuse scattering measurements, two types of scans can be executed. A transverse diffuse scan is performed about a specular point by scanning θ motor at fixed 2θ. The longitudinal diffuse data are collected along a specular direction keeping a suitable offset in θ motor. We can

perform scans with a minimum step of 0.001° with stepping motors. In the analysis of these reflectivity data, instrumental effects are important. Obtained data are properly corrected considering footprint of the beam and appropriate resolution functions depending on the slit widths as very discussed in the review by Sanyal et al [117]. The details of resolution functions are discussed in next chapter.

2.4.2 Synchrotron Sources

A Synchrotron source is a source of electromagnetic radiation produced by accelerating charges, mainly electrons, in a curved path. The electromagnetic radiation so produced is known to be synchrotron radiation [139, 122]. A schematics of a synchrotron is shown in Figure 2.12. In a typical synchrotron source first the electrons are accelerated to high speeds in a linear accelerator (LINAC) to gain the energy in the range of several Giga-electron-Volts (GeV) and then transferred into storage rings in which the electrons are kept circulating at constant energy. In a storage ring the synchrotron radiation is produced either in the bending magnets needed to keep the closed orbits, or in the insertion devices wigglers or undulators situated in the straight sections of the ring. In these devices an alternating magnetic field forces the electrons to follow oscillating paths rather than moving in a straight line. In a wiggler the amplitude of the oscillations is rather large, and the radiation from different wigglers add incoherently, whereas in undulators, electron produce a coherent addition of the radiation from each oscillation. Apart from these devices a RF or radio frequency system is also kept in a storage ring to replenish the energy of the electrons radiated as synchrotron X-rays.

A X-ray beam is characterized by single quantity called *Brilliance*, which allows one to compare the quality of X-ray beam from different sources, and defined as

$$Brilliance \;=\; \frac{Photons/second}{(mrad)^2(mm^2\; source\; area)(0.1\%\; bandwidth)}$$

The brilliance is a function of the photon energy.

After a X-ray beam is extracted from a storage ring, which is considered as *white*

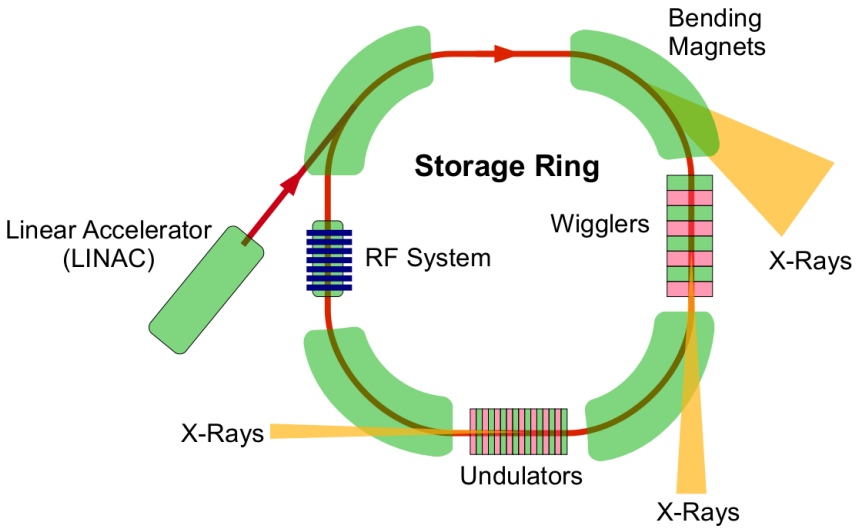

Figure 2.12: Schematics of a Synchrotron Source.

beam, is allowed to pass through a series of vacuum pipes for its conditioning to use it for any particular experiment. This whole section of conditioning a beam is known to be Beamlines. A standard synchrotron beamline consists of the following components:

- **Monochromator**: For X-rays, Silicon or Germanium single crystals are used as monochromators. The purpose of these single crystals is to extract a particular wavelength or energy from the white X-ray beam. This is done by incident the white beam on the crystals and the lattice planes of the crystals diffract the X-rays of different energies in different directions in accordance with Bragg's law. In order to direct the diffracted beam in the same direction as the incident one another similar crystal parallel to the first is used (shown in Figure 2.13). Monochromators with this kind of crystal arrangements are known to be *Double Crystal Monochromators*.

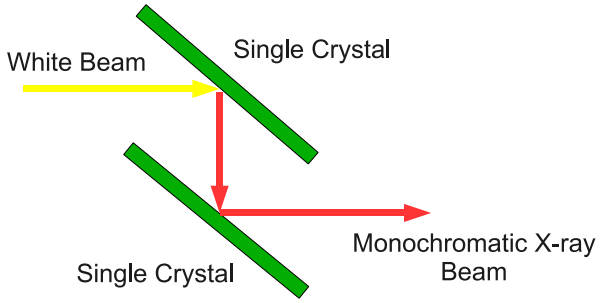

Figure 2.13: Schematics of Double Crystal Monochromator.

- **Windows**: Thin sheets of metal, often beryllium, which transmit almost all of the beam, but protect the vacuum within the storage ring from contamination, are generally used as windows.
- **Slits**: In order to define both the horizontal and vertical beam size several slits are used before indenting the beam on a sample of interest.
- **Focusing Mirrors**: One or more mirrors, which may be flat, bent-flat, or toroidal are used to collimate or focus the X-ray beam. Lenses are also used.
- **Spacing tubes**: Vacuum tubes which provide the proper space between optical elements, and shield any scattered radiation, are generally used in beamlines.

2.4.3 Liquid Surface Spectrometer

Measurement of the angular dependence of the reflectivity from a solid sample can be achieved by simply rotating the sample with respect to the incident beam. This is obviously unacceptable for studying bulk liquids, since the surfaces must remain horizontal. Therefore, studying liquids requires a specially designed goniometer that is commonly called liquid surface spectrometer [121].

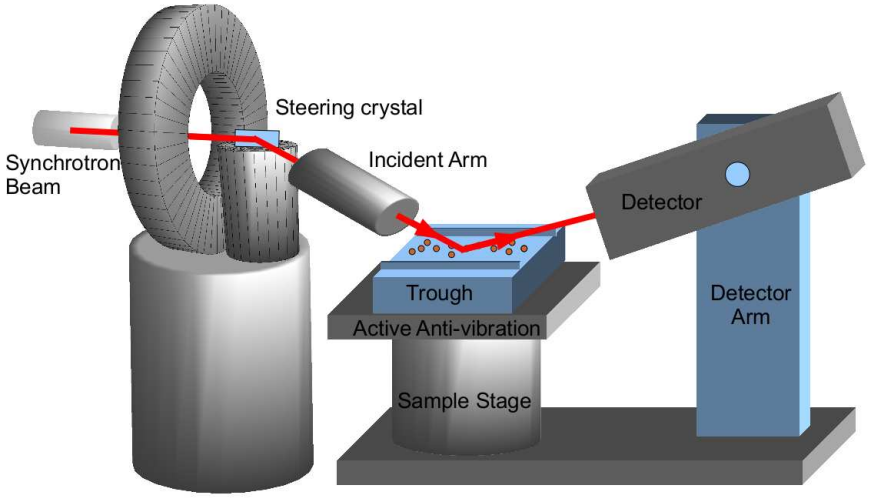

Figure 2.14: Schematics of Liquid Spectrometer.

In Figure 2.14 we have shown a schematics of a Liquid spectrometer. A horizontal monochromatic beam from the synchrotron source is Bragg-reflected by a steering crystal that can be rotated around the axis parallel to the incident beam by an angle χ while keeping the angle between the incident beam and the reciprocal lattice vector $\overrightarrow{G}$ of the crystal fixed. In this way the angle α that the Bragg-reflected beam makes with respect to the horizontal plane of the sample changes such that

$$G \sin \chi = \frac{2\pi}{\lambda} \sin \alpha \tag{2.4}$$

There is an incident arm located between the steering crystal and the sample, containing the slits defining the size of the beam and the normalization monitor. The size of the slit is smaller than the size of the beam and is usually on the order of 10 μm for low incident angles and opened up to 300-500 μm for higher angles to increase the flux. The normalization monitor is used to measure the intensity of the incident beam, which is then used to normalize the scattered signal. In view of the fact that the beam follows a cone the incident arm as well as the sample stage containing the sample have to move both vertically and horizontally in order to follow the beam. The beam reflected from the sample is registered by a detector that must also move horizontally in order to follow the reflection. If the distance

from the steering crystal to the sample stage is equal to the distance from the sample stage to the detector then the vertical position of the detector can be held fixed.

In fact, the actual mechanical implementation of what might appear a rather simple instrument is quite sophisticated. Depending on the particular setup, a typical liquid surface spectrometer requires motion of more than twenty individual motors, some of which require precision in the range of 1μm - 100μm for linear motors and a few millidegrees for rotational motors. These include motors responsible for movement of monochromator crystal, sample height (which is defined by the incident angle α), detector height and detector rotation (which determines output angle β, as well as various motors responsible for optical delivery of the beam (mirrors and slits). In addition there are two sets of motorized slits before the sample and two on the detector side, each of which has four separate motors. The motion of most of the spectrometer motors is controlled by commands issued through a computer interface, according to a liquid surface geometry code [140, 141]. However, for the geometry code to work properly, the exact positions of these motors have to be individually aligned with respect to both the x-ray beam and the positions of other motors. Furthermore several tracking parameters, such as the distances that relate the linear displacement of the sample and detector to the various angles, have to be carefully determined before liquid surface spectrometer can be used. Also, in the course of the measurement there is often slight drifts in the position of the incident beam, the shape of the liquid sample, etc. As a consequence key motor positions and tracking parameters have to be periodically checked during the experiment, and if necessary adjusted [142, 143].

2.4.4 Active Anti-vibration system

One of the experimental difficulties in dealing with liquids is that even minor vibrational noise disturb the sample, causing ripples on the surface that deflect the reflected beam away from the detector. It is therefore crucial to isolate the liquid from vibrations coming from either outside of the experimental hutch, or from the movements of liquid spectrometer itself. Suppression of external vibrations are accomplished by a commercially available active vibration isolation system. The

Beamline	Source	Energy, E(keV)	Mono-chromator	Flux (ph/s/mm^2)	Resolution ($\triangle E/E$)
ID10B, ESRF, France	Undulator	8-22	Diamond(111), Diamond(220)	1×10^{12} @ 9 keV	5.9×10^{-5}, 2.3×10^{-5}
X21, NSLS, BNL,USA	Wiggler	6-16	Si(111), Multilayers	2×10^{12} @ 300 mA	2.0×10^{-4}, 1.0×10^{-2}
15IDC, APS, ANL, USA	Undulator	6-32	Diamond(111)	1×10^{13} @ 9 keV	2×10^{-4}

Table 2.1: Specifications of Beamlines used for our experiments.

motion of the table top containing the sample is detected by a highly sensitive piezoelectric accelerometer consisting of a mass resting on a piezoelectric disc. The acceleration signal obtained by accelerometer is processed by analog control circuit and amplifier. A correction signal is then supplied to a magnetic actuator that is located on the movable table that supports the liquid sample. Active feedback systems available commercially are capable of suppressing external vibrations in all 6 degrees of freedom with frequencies $>$ 0.6Hz while supporting up to 90 kg of equipment. Minimization of the effect of vibrations caused by the movements of the spectrometer is further achieved with a pre-determined sleep time, normally on the order of 5 to 10 seconds, is used between the completion of the motor movement and the beginning of signal detection count.

2.4.5 Spectrometers used in our experiments

For our X-ray scattering experiments to study growth and structure of films of gold nanoparticles on air-water and toluene-water interface we have used Liquid spectrometer of ID10B (Tröika II) Beamline of European Synchrotron Radiation Facility, France and 15IDC beamline of Advanced Photon Source at Argonne National Laboratory, USA. We have also used X21 beamline of National Synchrotron Light Source (NSLS) at Brookhaven National Laboratory, USA for our in-situ study of formation and ordering of gold nanoparticles at toluene-water interface. The specifications of the beamlines used for our experiments are given in Table 2.1.

2.4.6 Trough and Cell used for the study at Liquid-Liquid interface

There are two major challenges in studying ordering at the interface of two immiscible liquids. Firstly, when X-rays has to penetrate through one of the liquids to incident on the interface and get scattered most of its energy is absorbed due to the absorption of the liquids. Secondly, the interface between the liquids always forms a curved meniscus with the wall of the trough/container containing the liquids and makes the grazing incidence scattering measurements an impossible task.

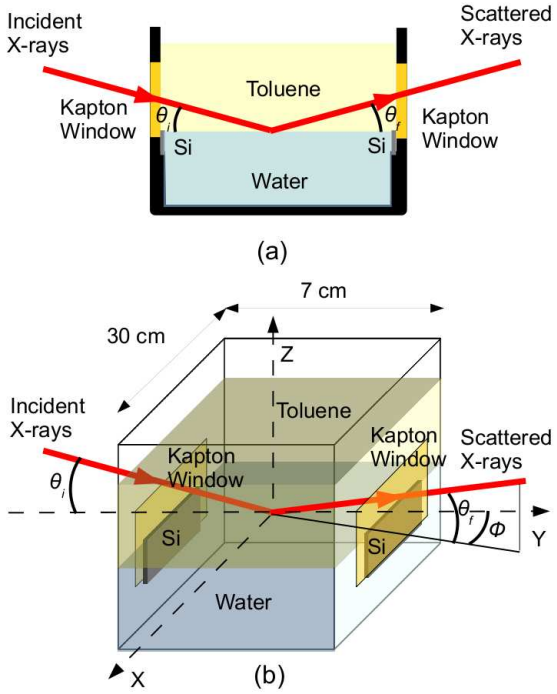

Figure 2.15: Schematics of the trough prepared for Grazing Incidence X-ray scattering measurements from toluene-water interface with (a) side view and (b) Perspective view. Dimensions of the trough are not up to the scale.

The availability of high brilliance synchrotron sources makes it possible to select high energy X-rays which can penetrate through the liquids and then the scattered X-rays have enough intensity to provide a good quality data. While in order to flatten the curved meniscus smart techniques have been employed. In order to perform grazing incidence X-ray scattering from liquid-liquid interface we have used a trough which has been developed in ID10B beamline of ESRF, France. The schematics of the trough is shown in Figure 2.15. The trough made of Teflon is 30

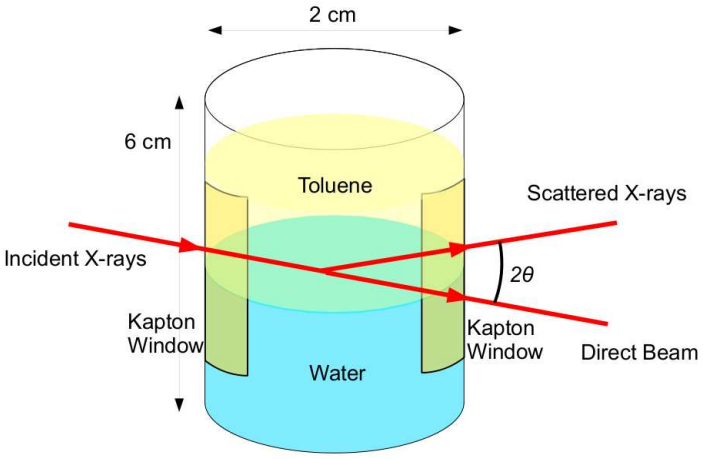

Figure 2.16: Schematics of Teflon cell.

cm long and 7 cm wide and has a pair of Kapton windows on the opposite side of the walls through which X-rays can go in and go out of the trough. Two thin silicon wafer of 0.5 mm thickness are mounted on the windows to anchor the interface between the two liquids. The anchoring of the interface is done by adjusting the height of the interface with control addition and removal of the lower liquid. In our experiments we have used water as the lower layer and toluene as upper one.

In ordered to perform Small Angle X-ray scattering from liquid-liquid interface in which flattening of interface is not very much required we prepared a cylindrical cell made of Teflon. The height and diameter of the cell is 6 cm and 2 cm respectively. This cell has also two Kapton windows on diametrically opposite side of the cell to allow the X-ray to go in and out of the cell. The experiment is performed at X21 beamline of National Synchrotron Light Source (NSLS), Brookhaven National Laboratory (BNL), USA. Details of the experiments will be discussed in Chapter 6.

2.5 Atomic Force Microscopy

The advent of Scanning Probe Microscopes and especially of the Atomic Force Microscope (AFM) has opened new perspectives in the field of microscopy. AFM is a very high-resolution type of scanning probe microscope having nanometer order of resolution which is more than 1000 times better than the optical diffraction limit. First AFM was designed by Binnig, Quate and Gerber [144] in 1986, four years after

the invention Scanning Tunneling Microscope [145]. The need of conducting sample and ambient measurement conditions like ultrahigh vacuum for STM measurements make AFM more popular than STM for surface microscopy. Though lots of advancements [146]have been done in the designing of ATM but the basic principle remained the same.

2.5.1 Basic Principle

In AFM a sharp tip mounted on a cantilever is allowed to scan over a sample surface and deflection of the tip due to its interaction with the sample surface atoms is monitored. Schematics of AFM is shown in Figure 2.17. Under normal working conditions the interaction forces between the tip and sample atoms bend the cantilever following Hooke's law. The cantilever deflection is detected by an 'optical lever' principle and converted into an electrical signal to produce the images. In optical lever method, a laser beam reflected from the backside of the cantilever is made incident on a Position Sensitive Photo Detector (PSPD). As the cantilever deflects, the angle of reflected beam changes and the spot falls on a different part of the detector. Generally the detector is made of four quadrants (marked as A, B, C and D in Figure 2.17) and the signals from the four quadrants are compared to calculate the position of the laser spot. The vertical deflection of the cantilever

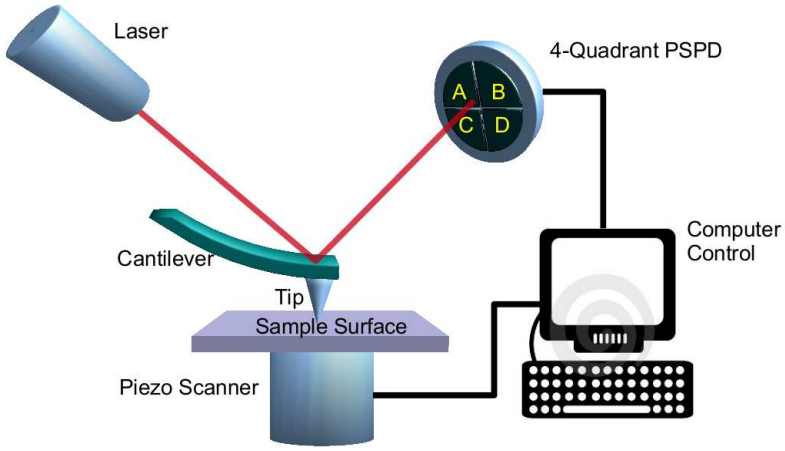

Figure 2.17: Schematics of a Atomic Force Microscope showing its working principle.

can be calculated by comparing the signal from the 'top' and 'bottom' halves of the

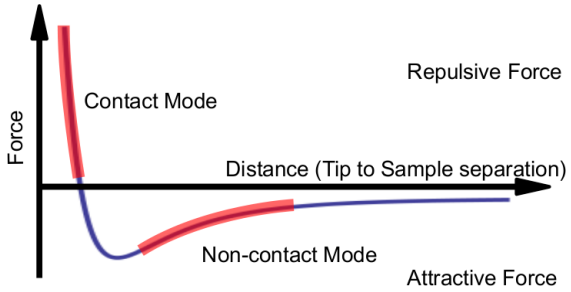

Figure 2.18: Variation of inter-atomic forces with distance.

detector. The lateral twisting of the cantilever can also be calculated by comparing the 'left' and 'right' halve signals from the detector. This detection system measures the cantilever deflection with sub-Angstrom sensitivity. The spring constant of the cantilever should be small enough to allow detection of small forces and its resonant frequency should be high to minimize sensitivity to mechanical vibration. The scanning i.e tip or sample movement is performed by an extremely precise positioning device made from piezo-electric ceramics, most often in the form of a tube scanner. The scanner is capable of sub-Angstrom resolution in X, Y and Z-directions. To control the relative position of the tip with respect to the sample accurately, good vibration isolation of the microscope has to be ensured.

In AFM, the force $F(r)$ which acts between the tip and sample is used as the imaging signal. For two electrically neutral and non-magnetic bodies held at a distance r of the order of several nanometers, the van der Waals forces usually dominate the interaction between them. The force can be derived from the Lenard-Jones potential and its distance dependence can be written as

$$F(r) \propto \left[\frac{1}{r^{13}} - \frac{1}{r^{7}}\right]$$

The variation of interaction force with the distance is depicted in Figure 2.18. As the atoms are gradually brought together the attractive force between them increases until they are so close together that their electron clouds begin to repel each other electrostatically. This electrostatic repulsion progressively weakens the attractive force as the inter-atomic separation continues to decrease and when the

distance between the atoms reaches a couple of Angstroms, the total van der Waals force becomes repulsive. In AFM, the local variation of the force acting between the tip and the sample is measured in order to generate the three dimensional images of the surface.

2.5.2 Modes of Operation

There are various modes of operation of an AFM among which contact mode, tapping mode and non-contact mode are frequently used to probe surfaces.

2.5.2.1 Contact Mode

In contact mode, the tip and the sample remain in close contact during the scanning, i.e. the tip is always in the repulsive regime of the intermolecular force as shown in Figure 2.18 on the preceding page. The forces range from nano to micro-Newton in ambient and even lower (0.1 nN or even less) in liquids. In this mode, imaging can be done in two different methods:

Constant Force Imaging: In this method a feedback circuit adjusts the height of the tip during scanning so that the cantilever deflection and hence the corresponding force remains same. The feedback system is connected to the z-piezodrive and the output signal of the feedback loop adjusts the vertical z position of the sample or the tip to achieve a constant cantilever deflection (constant force). The output signal can be recorded as a function of (x, y) co-ordinates which are determined by the corresponding voltages applied to the x and y piezoelectric drives. The obtained signal obtained in terms of voltages can finally be translated into 'topography' $z(x, y)$ provided that the sensitivities of the three orthogonal piezoelectric drives are known.

Constant Height Imaging: In this method the tip is scanned at a fixed height above the sample and the variation in tip sample interaction force reflects the atomic-scale topography of the sample. This mode is useful when the tip has to be scanned faster than the finite response time of the feedback loop. A significant drawback of this mode lies in the fact that vertical height information is not directly avail-

able. Although the constant force mode is generally preferred for most application, constant height mode is often used for taking atomic scale images of atomically flat surfaces, where the cantilever deflections and thus the variation in force is small. This also essential for recording real-time images of changing surfaces, where high scan speed is essential. A significant drawback of the contact mode is the dragging motion of the probe tip, combined with adhesive forces between the tip and the surface which can cause substantial damage to both sample and probe and creates artifacts in the resulting image. Thus this mode is not an ideal one to perform high resolution topographic imaging of surfaces of soft materials which can easily be damaged or of over-layers those are loosely bounded to the substrates.

2.5.2.2 Non-Contact Mode

Non-contact AFM (NC-AFM) mode is a vibrating cantilever technique in which an AFM cantilever is made to vibrate above the surface at such a distance that the forces of interaction not remains in the repulsive regime of the inter-atomic force curve as indicated in Figure 2.18 on page 37. Since in non-contact regime, there is no contact between the tip and the sample surface and the total force acting between them is very low, this mode is advantageous for studying soft or elastic samples. Cantilever used in this mode must be stiffer that those used for contact AFM because soft cantilever can be pulled to contact with the sample surface. Th small force values in non-contact regime and the greater stiffness of the cantilevers make the NC-AFM signal small and therefore difficult to measure. Thus a sensitive AC detection scheme is used for NC-AFM operation. In non-contact mode, a stiff cantilever vibrates slightly above its resonant frequency (typically from 100 to 400 Hz) with an amplitude of a few hundred of Angstroms. The resonant frequency of the cantilever is decreased by van der Waals force resulting in a change in oscillation amplitude. The system monitors the changes in resonance frequency or vibrational amplitude of the cantilever and these changes can be used as a measure of changes in the force gradient, which reflects changes in the tip-to-sample spacing or sample topography. The resonance frequency or vibrational amplitude of the cantilever is kept constant with the aid of feedback system that moves the scanner up and down.

By keeping the resonant frequency or amplitude constant, the system also keeps the average tip-to-sample distance constant. As with contact AFM, the voltage applied to the scanner is used to generate the topography. Although this mode does not suffer from the tip to sample degradation effects that are sometimes observed after taking several scans with contact AFM. Contact AFM often provides better resolution that NC-AFM. This is because the attractive van der Waals forces are substantially weaker that the forces used by contact mode and the attractive forces extend only a small distance from the surface, where the adsorbed fluid layer may occupy a large fraction of their useful range. Hence, even when the sample-tip separation is successfully maintained, non-contact mode provided substantially lower resolution that contact mode.

2.5.2.3 Tapping Mode

Tapping mode imaging overcomes the limitations of the conventional scanning modes by alternately placing the tip in contact with the surface to provide high resolution and then lifting the tip off the surface to avoid dragging the tip across the surface. Tapping mod imaging is implemented in ambient by oscillating the cantilever assembly at or near the cantilever's resonance frequency using a piezoelectric crystal. The piezo motion causes the cantilever to oscillate with high amplitude (typically greater than 20 nm) when the tip is not in contact with the surface. The oscillating tip is then moved toward the surface until it begins to lightly touch, or 'tap' the surface. During scanning, the vertically oscillating tip alternately contacts the surface and lifts off, generally at a frequency of 50, 000 to 500,000 cycles per second. As the oscillating cantilever begins to intermittently contact the surface, the cantilever oscillation is reduced due to energy loss caused by the tip contacting the surface. The amplitude of oscillation changes when the tip scans over the bumps or depressions. A constant oscillation amplitude and thus a constant tip-sample interaction is maintained during scanning with the help of the feedback circuit by adjusting the tip-sample separation. This mode inherently prevents the tip from sticking to the surface and causing damage during scanning. Unlike contact and non-contact modes, when the tip contacts the surface, it has sufficient oscillation amplitude to

overcome the the tip-sample adhesion forces. Also, the surface material is not pulled sideways by lateral forces since the applied force is largely vertical. This technique has proved to be valuable tool since it allows reduction of the lateral forces acting on the sample during scanning. Damage and distortion to the sample can be minimized. For these reasons, tapping mode ARM is well suited for the study of polymer, nanoparticles, soft matter and fragile objects.

We have used Nanoscope-IV Multimode SPM from Digital Instruments, USA, in tapping mode under ambient conditions to obtain the surface morphology of thin films of gold nanoparticles deposited on Silicon substrates. We have also used Variable temperature ultra high vacuum scanning probe microscope (VT-UHV-SPM) from Omicron Nano-Technology, Germany, in tapping mode under under ultra high vacuum (10^{-10} millibar) for obtaining high resolution images of topography of ultra thin films of gold nanoparticles prepared at toluene-water interface by a reduction reaction. Measurements by both the instruments are done at SPD, SINP, India. The details of the measurements are discussed in the corresponding chapters.

2.6 Scanning Electron Microscopy

Scanning electron microscopy (SEM) [147] is widely used to obtain images of the morphology or topography of a specimen by scanning an electron probe across it. Compositional analysis of the specimen can also be carried out by monitoring characteristic x-rays produced by the electron-specimen interaction. Thus detailed maps of elemental distribution along with the topography the specimen comprising multiphase materials or composites and bio-active materials can be done using SEM.

Figure 2.19: The SEM setup in our Laboratory.

Figure 2.19 shows the FEI Quanta 200F schottkey field emission gun (FEG) Scanning Electron Microscope set up in our laboratory. The Quanta 200F FEG SEM operates in three vacuum modes for different types of samples: High Vacuum mode is the conventional mode for observing conducting sample. Other two modes are Low Vacuum and ESEM modes using which one can observe nonconducting materials (insulator, ceramic, polymer) without any metal coat on the sample. In either of these two modes, water vapour is used inside the chamber from a built-in water reservoir. The ionization of H2O by electron bombardment produces $H^{+}$and OH^{-} which help to neutralize the charging on the nonconducting sample under investigation. Acceleration voltage of the electron beam of the employed SEM can be varied from 200V to 30kV. The resolution is 2 nm at 30 kV in high vacuum and 3.5 nm at 3 kV in low vacuum mode. This particular advantage allows to work with nonconducting polymer samples at ESEM or low vacuum mode at a low pressure (around 0.3 Torr) without damaging the sample.

The schematics overview of a SEM is shown in Figure 2.20 on the next page. There are different types of detectors used for different mode—the Everhart Thomley Detector (ETD) is a Secondary Electron (SE) detector. The Gaseous Secondary Electron Detector (GSED) and Large Field Detector (LFD) are used for both Low Vac and ESEM modes. Also for back-scattered electron detections a solid state back-scattered electrons (BSE) detector is included.

The energy of the primary electrons determines the quantity of secondary elec-

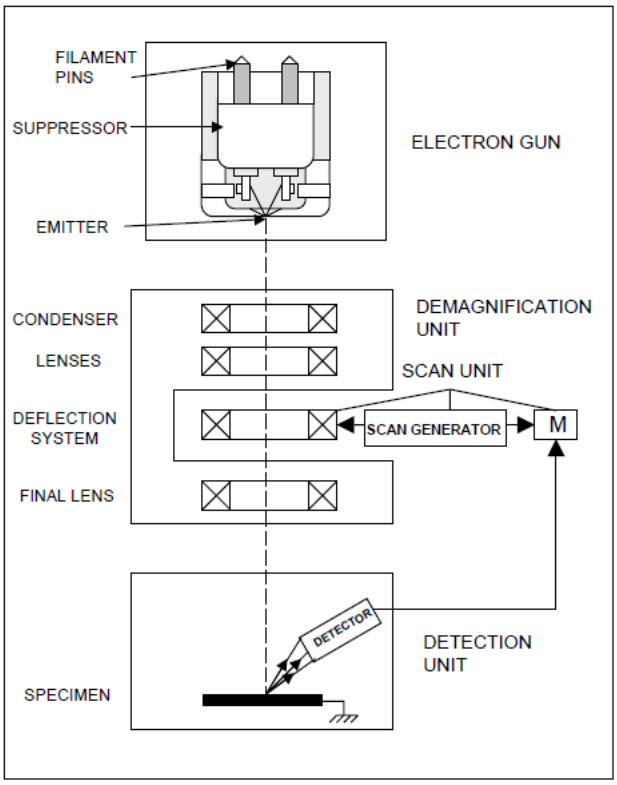

Figure 2.20: The schematic diagram to show the working principle of SEM.

trons collected during inspection. The emission of secondary electrons from the specimen increases as the energy of the primary electron beam increases, until a certain limit is reached. Beyond this limit, the collected secondary electrons diminish as the energy of the primary beam is increased, because the primary beam is already activating electrons deep below the surface of the specimen. Electrons coming from such depths usually recombine before reaching the surface for emission. Aside from secondary electrons, the primary electron beam results in the emission of back-scattered (or reflected) electrons from the specimen. Back-scattered electrons possess more energy than secondary electrons, and have a definite direction. Back-scattered electron imaging is useful in distinguishing one material from another, since the yield of the collected back-scattered electrons increases monotonically with the specimen's atomic number.

2.6.1 Energy Dispersive X-ray Spectrometry (EDS)

The SEM set up in our laboratory (refer Figure 2.19 on page 42) is also equipped with a Energy Dispersive X-ray Spectrometer (EDS). The EDS system uses a sapphire Si(Li) type detector with a Super Ultra Thin Window (SUTW) for detection of all elements down to and including Beryllium with a resolution of 130 eV or better, measured at MnK_α, 1000 CPS and with the time constant 100 μs. EDX analysis is useful for elemental analysis with a minimum detection limit of ∼0.1 wt%, as well as estimating their relative concentrations on the surface of the sample.

During EDX analysis, the sample is bombarded with an electron beam inside the scanning electron microscope. The electron beam generates X-ray photons in the beam specimen interaction volume beneath the specimen surface. These X-ray photons have energies specific to the elements in the specimen and are called the characteristic X-rays that provide the SEM's analytical capability. The X-ray photons pass through the Si(Li) detector and processed by a computer X-ray analyzer (CXA) and the resulting spectrum are displayed on a computer screen. Furthermore, the atom of every element releases X-rays with unique amounts of energy during the transferring process. Thus, by measuring the amounts of energy present in the X-rays being released by a specimen during electron beam bombardment, the identity of the atom from which the X-ray was emitted can be established. The EDX spectrum is just a plot different X-ray energies corresponding to the energy levels of different elements vs. the counts related with the characteristic X-ray peaks. An EDX spectrum plot not only identifies the element corresponding to each of its peaks, but the type of X-ray to which it corresponds as well. For example, a peak corresponding to the amount of energy possessed by X-rays emitted by an electron in the L-shell going down to the K-shell is identified as a K_α peak. The peak corresponding to X-rays emitted by M-shell electrons going to the K-shell is identified as a K_β peak and so on. One can do X-ray mapping analysis of a certain portion of the sample to see how the elements are exactly distributed to that area.

We have used SEM in low vacuum mode for studying the patterns formed by thiol passivated gold nanoparticles on Polyacrylamide thin films which is discussed in Chapter 4 & 5. We have also used SEM in the same mode for studying the thin

films of gold nanoparticles formed at toluene-water interface by interfacial reduction reaction. In order to check the composition of the films we have collected also collected EDX spectra which will be discussed in Chapter 6.

Chapter 3

Theoretical Formalism

After the invention of X-rays by Roentgen in 1986, and pioneering works of Bragg and Laue on crystal structure determination by using X-rays, a new field called *X-ray Crystallography* has emerged. Soon After the availability of intense X-rays from the modern synchrotron sources, now X-rays have found its use in the determination of interfacial structures of solids, liquids. X-rays are electromagnetic waves and interact with materials through its electrons. The refractive index of X-rays for any material as shown for the first time by Compton is less than 1 and given by

$$n = 1 - \delta + \mathrm{i}\beta \tag{3.1}$$

where δ and β are positive quantities and depend on the average electron density (ρ_e) and absorption coefficient (μ) of the material as

$$\delta = \frac{\lambda^2 r_e}{2\pi}\rho_e \tag{3.2}$$

$$\beta = \frac{\lambda}{4\pi}\mu \tag{3.3}$$

where $r_e = 2.814 \times 10^{-5}$ Å and known as *classical electron radius* and λ is the wavelength of X-rays. According to the laws of optics, X-rays suffer total external reflections when it propagate through a medium of higher refractive index and incident on a surface of a material having lower refractive index. The very concept of total external angle defines an angle below which the X-rays are totally reflected

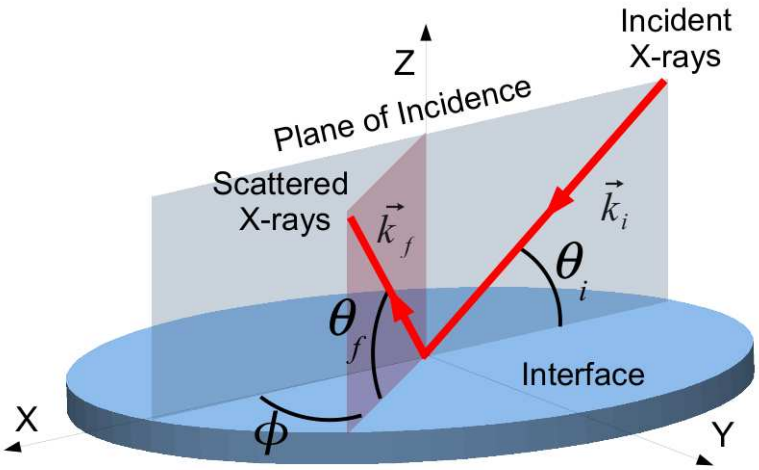

Figure 3.1: Schematics of the Scattering Geometry for GIXS measurements.

and termed as *Critical angle* (θ_c) and related to the electron density of the material as

$$\theta_c = \sqrt{2\delta} \quad = \quad \lambda\sqrt{\frac{r_e\rho_e}{\pi}} \tag{3.4}$$

provided the first medium is vacuum. Otherwise, for two different media it is related in the same fashion to the difference between their electron densities. The phenomena is of great importance for the study of surfaces/interfaces due to the reason that below the critical angle the X-rays propagate as an evanescent wave along the surface/interface with a penetration depth of few nanometers. Around this critical angle X-rays can probe both in-plane and out-of-plane structures at the surfaces/interfaces and the measurement techniques developed for this very purpose are known to be GIXS techniques.

In Figure 3.1, the schematics of scattering geometry employed under GIXS techniques is shown. The incident X-ray beam has momentum vector $\vec{k_i}$ and then the elastically scattered X-rays will have momentum vector $\vec{k_f}$ with $|\vec{k_i}| = |\vec{k_f}| = k_0 = 2\pi/\lambda$, where λ is the wavelength of X-rays. Then we can write the wave-transfer vector as

$$\vec{q} \quad = \quad \vec{k_f} - \vec{k_i} \tag{3.5}$$

with the components along X, Y and Z directions respectively [117] as

$$\begin{aligned} q_x &= k_0 \left(\cos\theta_f \cos\phi - \cos\theta_i\right), \\ q_y &= k_0 \left(\cos\theta_f \sin\phi\right) \text{ and} \\ q_z &= k_0 \left(\sin\theta_f + \sin\theta_i\right) \end{aligned} \tag{3.6}$$

We can also define an in-plane wave transfer vector by combining the q_x and and q_y components as

$$\begin{aligned} q_{||} &= \sqrt{q_x^2 + q_y^2} \\ &= k_0 \sqrt{\cos^2\theta_f + \cos^2\theta_i - 2\cos\theta_f \cos\theta_i \cos\phi} \end{aligned} \tag{3.7}$$

In general in grazing incidence geometry θ_i, θ_f are small and $\cos\theta_i, \cos\theta_f \approx 1$ and then the in-plane wave transfer vector becomes function of in-plane angle ϕ as

$$q_{||} = 2k_0 \sin\left(\frac{\phi}{2}\right) \tag{3.8}$$

Depending on different angular settings there are several types of measurements under GIXS as follows.

3.1 Specular X-ray Reflectivity (XRR)

Specular X-ray reflectivity has emerged as a powerful tool for the investigation of the structural properties of thin films. In XRR technique, a well collimated monochromatized X-ray beam is allowed to incident on a sample surface/interface at a grazing incidence θ_i (starting form few milliradians) and the reflected intensity is recorded in the plane of incidence ($\phi = 0$) at an angle θ_f. If the angle of incidence of impinging X-rays is sufficiently small (less than θ_c), the penetration depth and the scattering is limited to the near interface region. Reflectivity data is generally taken at angles considerably larger than the critical angle of total external reflection and therefore penetration depth is of the order of hundreds of nanometers. The

sensitivity is then obtained by interference of X-rays by layers with different electron densities at different depths in the sample.

It one of the most used GIXS techniques in which intensity of specularly reflected X-rays are measured as function of angle of incidence (θ_i). The necessary angular conditions maintained during the measurements are

1. $\theta_i = \theta_f$ and

2. $\phi = 0$.

With these angular conditions the reflected intensity is only a function of out-of-plane wave transfer vector q_z and $q_x, q_y = 0$. XRR provides us with structure along the out-of-plane direction of the surfaces/interfaces. The scattering intensity collected as function of θ_i has a dependence on the distribution of electron density in the out-of-plane direction across the surfaces/interfaces. Generally point detectors are used for these measurements.

There are two approaches to calculate XRR from a thin film at any interface. First approach is exact and make use of Maxwell's equations to calculate the Electric Field vectors at different depth of the film to calculate the reflectivity. This approach automatically takes care of multiple scattering and termed as Dynamical Theory [148, 149, 150]. The second approach, known as Kinematical Theory or Born Approximation [148, 149], greatly simplifies the expression for the intensity of specular reflectivity for non-ideal surfaces that are either rough or have structure.

3.1.1 Dynamical Theory

The basic expression for specular X-ray reflectivity for a smooth surface can be obtained by solving the Maxwell's wave equations under the appropriate boundary conditions for the continuity of the electric field and its derivatives [150,151,152,150]. The wave equation for the electric field, $\psi(\vec{r})$, can be written in the form of the Helmholtz equation as

$$\left(\nabla^2 + k^2 n(\vec{r})^2\right)\psi(\vec{r}) = 0, \tag{3.9}$$

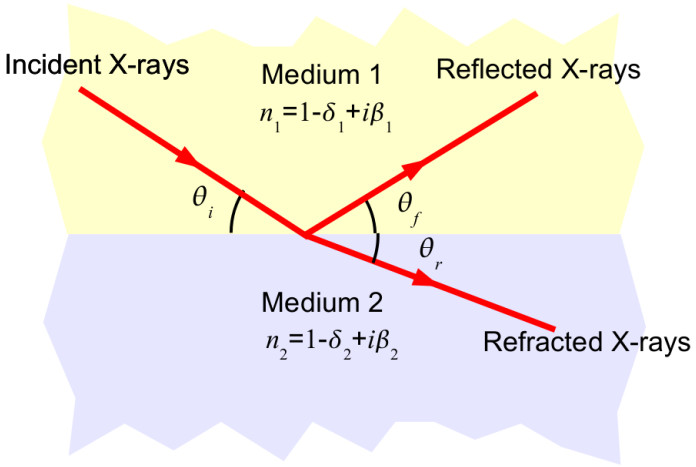

Figure 3.2: Schematic showing incident, reflected and refracted X-rays from s Vacuum-Medium interface.

where $\vec{k}$ is the momentum vector of the X-rays in vacuum with $|\vec{k}| = 2\pi/\lambda$ and $n(r)$ is the refractive index of the medium given by Equation 3.1.

In vacuum, the z-component of the momentum transfer vector, normal to the surface or $x-y$ plane, is given by

$$q_{z,0} = \frac{2\pi}{\lambda} (\sin\theta_f + \sin\theta_i) \tag{3.10}$$

In specular condition $\theta_i = \theta_f$, we can write

$$k_{z,0} = q_{z,0}/2 = 2\pi \sin\theta_i/\lambda \tag{3.11}$$

For a single interface separating two media shown in Figure 3.2, Snell's law of refraction gives

$$\frac{\cos\theta_i}{\cos\theta_r} = \frac{n_1}{n_2} = \frac{1-\delta_1+\beta_1}{1-\delta_2+\beta_2} \tag{3.12}$$

Since for any material $\delta \sim 10^{-6}$ and $\beta \sim 10^{-7}$ we can expand the denominator of Equation 3.12 in power series and neglecting the higher order terms we can write

$$\begin{aligned} \frac{\cos\theta_i}{\cos\theta_r} &= 1-(\delta_1-\delta_2)+i\,(\beta_1-\beta_2) \\ &= 1-\frac{\lambda^2 r_e}{2\pi}\triangle\rho_e + i\frac{\lambda}{4\pi}\triangle\mu \end{aligned} \tag{3.13}$$

Now depending on the differences in the average electron densities (electron density contrast) of two media one can define an angle of incidence such that the refracted angle becomes zero and the angle of incidence is known to be *critical angle* of that particular interface. From Equation 3.13 we can get the dependence of critical angle on the electron density contrast between the two media considering only the real part as

$$\theta_c = \sqrt{2\,(\delta_1-\delta_2)} = \lambda\sqrt{\frac{r_e}{\pi}\triangle\rho_e} \tag{3.14}$$

Similarly we can define a critical wave-transfer vector for the interface as

$$q_c = \frac{4\pi}{\lambda}\sin\theta_c \tag{3.15}$$

Depending on the critical wave-transfer vector $q_{c,i}$ of i^{th} medium with respect to that of vacuum the wave-transfer vector along z in in that medium can be written as

$$q_{z,i} = \sqrt{q_{z,0}^2 - q_{c,i}^2} \tag{3.16}$$

Now by using the appropriate boundary conditions for the electric field and its derivative at the interface between Medium 1 and Medium 2 one can obtain *Fresnel Formulas* for the reflection and transmission coefficients as [117, 122, 149, 148]

$$r_{1,2} = \frac{q_{z,1}-q_{z,2}}{q_{z,1}+q_{z,2}} \tag{3.17}$$

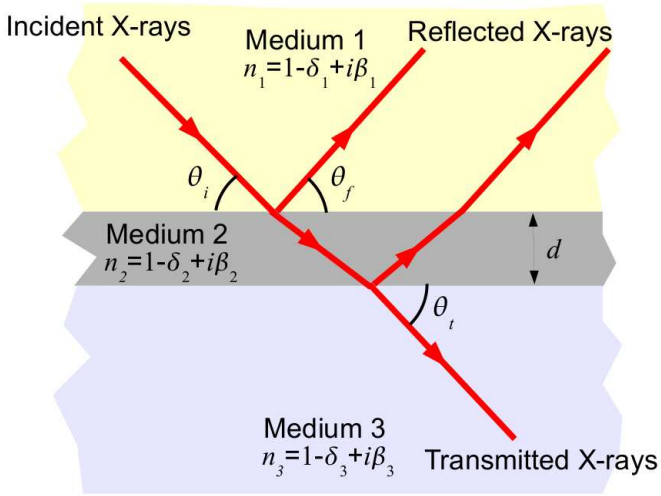

Figure 3.3: Schematics of incident, reflected and transmitted X-rays from a thin film sand-witched between two media.

and

$$t_{1,2} = \frac{2q_{z,1}}{q_{z,1} + q_{z,2}} \tag{3.18}$$

The specular X-ray reflectivity from an interface separating two media as function of wave-transfer vector can be written as

$$\begin{aligned} R(q_{z,0}) &= r_{1,2} r_{1,2}^* \\ &= \left| \frac{\sqrt{q_{z,0}^2 - q_{c,1}^2} - \sqrt{q_{z,0}^2 - q_{c,2}^2}}{\sqrt{q_{z,0}^2 - q_{c,1}^2} + \sqrt{q_{z,0}^2 - q_{c,2}^2}} \right|^2 \end{aligned} \tag{3.19}$$

and for $q_{z,0} > 3q_c$(obtained from Equations 3.15, 3.14) the Fresnel reflectivity from the interface may be well approximated by $q_{z,0}^{-4}$.

In the case of a thin film of finite thickness d as shown in Figure 3.3, we have to solve the wave equations at two interfaces. It is interesting to note that the continuity condition at $z = d$ will generate an extra factor, which in turn will give us reflectance at the film-substrate interface as

$$r_{2,3} = \frac{q_{z,2} - q_{z,3}}{q_{z,2} + q_{z,3}} \exp\left[-iq_{z,2}d\right] \tag{3.20}$$

With the help of simple algebra and noting the fact that $r_{21} = -r_{12}$ [150] we can write the reflectance from the thin film sand-witched between two media as

$$r_0 = \frac{r_{1,2} + r_{2,3}}{1 + r_{1,2}r_{2,3}} \tag{3.21}$$

We can easily extend the above calculation to the case of reflectivity for a system having M such thin films (stratified media), having smooth interfaces. We denote the thickness of each film by d_n. A set of simultaneous equations similar to Equation 3.21 can be solved and one can arrive at a recursive formula [153, 117] given by,

$$r_{n-1,n} = \frac{r_{n,n+1} + F_{n-1,n}}{1 + r_{n,n+1}F_{n-1,n}} \exp(-iq_{z,n}d_n) \tag{3.22}$$

where

$$F_{n-1,n} = \frac{q_{z,n-1} - q_{z,n}}{q_{z,n-1} + q_{z,n}} \tag{3.23}$$

To obtain the specular reflectivity of the system having M layers one solves the above recursive relations from the bottom layer with the knowledge that $r_{M,M+1} = 0$, since the thickness of the $(M+1)^{th}$ medium (normally the substrate) can be taken as infinite. It should be mentioned here that the reflectivity calculation of stratified homogeneous media having smooth boundary interfaces given by Equation 3.22 is not only used for multilayer films, but also widely used to approximate realistic continuously varying electron density profiles. This is done by subdividing the continuous electron density of the film into series of discrete layers [154, 155].

So far we have dealt only with smooth surfaces and interfaces. At this stage we can introduce the concept of roughness. It should be mentioned here that roughness is different from waviness of a/an surface/interface. In fact this difference becomes apparent when the variation of electron density is plotted as a function of depth (Z-axis). In the length scale probed by X-ray (few Angstroms), the density profile for rough surface will be a slowly varying function but the profile for surface having waviness will be sharp one. Roughness for solid films can vary from few tens of Angstroms fro very rough film to few Angstroms for films grown in Molecular Beam

Epitaxy (MBE) technique. Intrinsic roughness for liquid films are high and can be correlated to the molecular diameter of the liquid [112].

It is known that reflectivity of a rough surface is smaller than that of a smooth surface and this deviation increase with q_z. One can calculate the effect of roughness by approximating the electron density profile with a series of discrete layers as discussed above and using iterative scheme of Equation 3.22. Actually the first derivative of the scattering profile can be described, for most of the cases, as a Gaussian function and as a result by using Born Approximation [156] one can write the reflectivity of a rough surface as

$$r_{n-1,n} = r^F_{n-1,n} \exp[-q_{z,n-1} q_{z,n} \sigma^2_{n-1,n}/2] \tag{3.24}$$

The parameter σ_n is the measure of roughness between $(n-1)^{th}$ and n^{th} interfaces, and roughness acts like a *Debye-Waller Factor* [122]. σ_n is actually the Root Mean Square (RMS) fluctuation of the interface with respect to the average interface. Equation 3.24 also explains the observation that reflectance of rough surface $r_{n-1,n}$ deviates more from the reflectance for smooth surface $r^F_{n-1,n}$ as $q_{z,n-1}$ and $q_{z,n}$ increase with $q_{z,0}$ (or q_z). For a surface separating two media as shown in Figure 3.2 Equation 3.24 can be simplified [157] as

$$R_{rough} = R_F \exp[-q_z^2 \sigma^2_{1,2}], \tag{3.25}$$

where R_F is Fresnel given in Equation 3.19 and $\sigma_{1,2}$ represents surface roughness. In general, the roughness of the film surface brings down the reflectivity curve faster, on the other hand roughness of the interface of the film and the substrate reduces the amplitude of multilayer peaks.

3.1.2 Resolution Function

While performing reflectivity data analysis, one has to include the effect of resolution of the experimental set-up. The resolution mainly depends on the wavelength dispersion ($\triangle\lambda/\lambda$), the angular divergence of incoming beam ($\triangle\theta_i$) and the acceptance

of the outgoing beam ($\triangle\theta_f$). Before comparing a calculated data with a measured values one needs to convolute the calculated data with a relevant resolution function [117]. In the usual geometry of reflectivity measurements, the aperture of the detector slits perpendicular to the scattering plane is kept wide open so that the scattered intensity in the q_y direction is integrated out. So the resolution function is a dependent on the width of the slit along the scattering plane which gives a window of size $\triangle q_z$ in q-space over which the calculated reflectivity has to be integrated out. The $\triangle q_z$ depends on both the wavelength and geometry of the experimental set-up. To calculate $\triangle q_z$, we start with the total differential of Equations 3.6 with in-plane angle $\phi = 0$ as

$$dq_z = k_0 \left(\cos\theta_i d\theta_i + \cos\theta_f d\theta_f\right) + dk_0 \left(\sin\theta_i + \sin\theta_f\right), \tag{3.26}$$

$$dq_x = k_0 \left(\sin\theta_i d\theta_i + \sin\theta_f d\theta_f\right) - dk_0(\cos\theta_i - \cos\theta_f) \tag{3.27}$$

With the assumption that $d\theta_i$ and $d\theta_f$ are randomly distributed both $\triangle q_z$ and $\triangle q_x$ can be written as

$$\triangle q_z = \left[k_0^2 \left(\cos\theta_i^2 \triangle\theta_i^2 + \cos\theta_f^2 \triangle\theta_f^2\right) + \triangle k_0^2 \left(\sin\theta_i + \sin\theta_f\right)^2\right]^{\frac{1}{2}}, \tag{3.28}$$

$$\triangle q_x = \left[k_0^2 \left(\sin\theta_i^2 \triangle\theta_i^2 + \sin\theta_f^2 \triangle\theta_f^2\right) + \triangle k_0^2 (\cos\theta_i - \cos\theta_f)^2\right] \tag{3.29}$$

For angle dispersive reflectivity measurements ($\theta_i = \theta_f = \theta$), neglecting the wavelength dispersion term $\triangle k_0$ we can write the above equations as

$$\triangle q_z = k_0 \cos\theta \left[\triangle\theta_i^2 + \triangle\theta_f^2\right]^{\frac{1}{2}} \tag{3.30}$$

$$\triangle q_x = k_0 \sin\theta \left[\triangle\theta_i^2 + \triangle\theta_f^2\right]^{\frac{1}{2}} \tag{3.31}$$

Defining $\left[\triangle\theta_i^2 + \triangle\theta_f^2\right]^{\frac{1}{2}}$ as the Half-Width at Half-Maximum (HWFM), σ_d, of the direct beam we can write

$$\triangle q_z = k_0 \sigma_d \cos\theta \tag{3.32}$$

$$\triangle q_x = k_0 \sigma_d / 2 \tag{3.33}$$

3.1.3 Kinematical Theory or Born Approximation

The full dynamical theory described above is exact but does not clearly show the physics of scattering because numerical calculations are necessary. Sometimes simplifications or approximations can provide analytical expressions which reasonably matches with the exact solutions. Born Approximation greatly simplifies the expression for reflectivity by applying three approximations:

1. No Multiple Reflections at the interfaces.
2. The effects of refraction at the interfaces can be neglected.
3. The reflection coefficient at each interface is proportional to the difference of electron density.

By dividing a system into M discrete layers and incorporating the above approximations by their order for the calculation of reflectivity using Parratt recursion relations given by Equation 3.23 one can write the reflectance of the system as

$$r = \frac{4\pi r_e}{q_{z,0}^2} \sum_{j=1}^{M} (\rho_{j+1} - \rho_j) \exp[iq_{z,0} Z_{j+1}], \tag{3.34}$$

where Z_j is the depth of the j^{th} layer from the top surface of the system. Finally, if we consider the system to be made of an infinite number of thin layers, the sum may then transformed into an integral over z, and the reflectance has the form

$$r = \frac{4\pi r_e}{q_{z,0}^2} \int_{-\infty}^{+\infty} \frac{d\rho(z)}{dz} \exp[iq_{z,0} z] dz \tag{3.35}$$

Now we will apply another very useful approximation by replacing the factor $(4\pi r_e \rho_\infty)^2/q_{z,0}^4$ by Fresnel reflectivity of the vacuum-substrate interface $R_F(q_{z,0})$ and write the reflectivity as

$$R(q_{z,0}) = R_F(q_{z,0}) \left| \frac{1}{\rho_\infty} \int_{-\infty}^{+\infty} \frac{d\rho(z)}{dz} \exp[iq_{z,0} z] dz \right|^2 \tag{3.36}$$

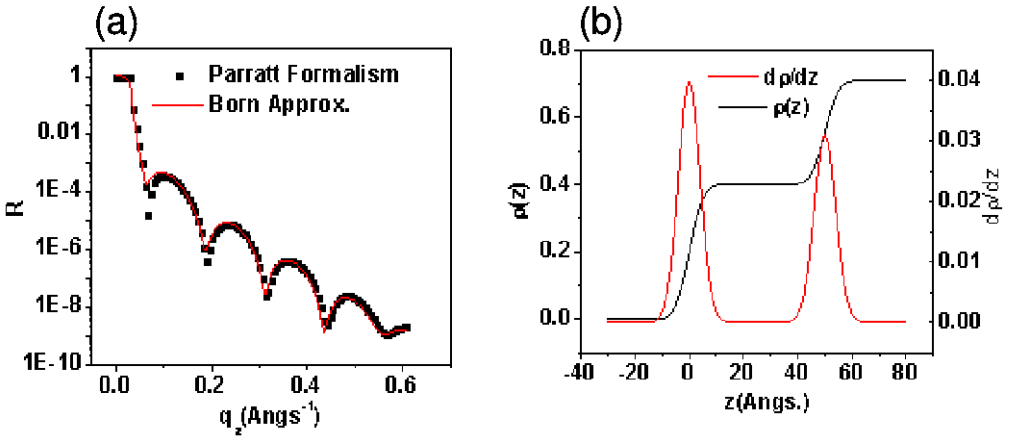

Figure 3.4: (a) Specular Reflectivity of a thin film of 50 Å calculated by both Parratt Recursion formula (Symbols) and Born approximation (Red Solid line) (b) The corresponding electron density profile and its derivative used for calculating reflectivity using Born approximation.

This equation is known as *Master Formula* with ρ_∞ to be the electron density of the substrate. As the basic assumption to obtain this analytical formula is the exclusion of multiple scattering events, this formula would work well only for thin films in which the effect of multiple scattering is not dominant. In Figure 3.4(a) we have shown X-ray specular reflectivity calculated by using Parratt recursion formula and Master formula along with the electron density profile as a function of depth and its derivative. The mismatch between the two calculated reflectivity is evident near the critical angle where multiple scattering is important.

3.1.4 Inversion Scheme Based on Born Approximation

In a reflectivity measurement, intensity of a X-ray beam is measured as a function of angle of incidence θ_i keeping the angle of reflection θ_f equal to that of incidence (shown in Figure 3.2). The reflectivity measurements provide information about electron density profile (EDP) of thin films as a function of depth z [153, 154]. The unavailability of phase information during the reflectivity measurements makes the extraction of the EDP from it non-trivial. In order to extract the EDP profile from the reflectivity measurement, one assumes an aprori EDP across the thin film and calculates reflectivity, approximating the EDP by a series of slabs having constant

electron densities, by using the recursive formula given by equation 3.22 . The calculated reflectivity profile is then fitted to the experimental data by varying some of the parameters such as the electron density of each slab, thickness of the slabs and roughness of the interfaces [149, 155]. This conventionally used technique works well for systems in which actual EDP is close to the apriori assumption of EDP with which the non-linear fitting process is started and only a few parameters are involved in fitting. Due to the recursive non-linear relationship between real space parameters, i.e thickness and electron density of each slab and reflectivity profile, determination of parameters by fitting becomes problematic when initial guess of real space parameters are far away from the actual solution. A scheme has been developed [158] to inverse the reflectivity data to get the actual EDP using the *Master formula* based on Born Approximation.

In order to calculate the reflectivity using the Master formula 3.36, one needs to provide the derivative of EDP as a function of depth as an input. According to the scheme [158], a model EDP $\rho_m(z)$ is considered which is close to the actual EDP $\rho_e(z)$ and their derivative will follow a relation given by

$$\rho'_e(z) \;=\; \mathcal{FT}^{-1}\left[\sqrt{\frac{R_e(q_z)}{R_m(q_z)}}\mathcal{FT}\left[\rho'_m(z)\right]\right] \tag{3.37}$$

where $R_e(q_z)$ and $R_m(q_z)$ are the experimental data and the calculated reflectivity data from the modeled EDP $\rho_m(z)$. $\mathcal{FT}$ and $\mathcal{FT}^{-1}$ are the representations for Forward and Inverse Fourier Transform respectively. In the above expression the phase factors of the actual and model reflectivity are assumed to be equal which is in practice not true. In order to avoid the phase problem an iterative procedure is employed to obtain the $\rho_e(z)$, through the intermediate derivatives of EDP generated in each iteration.

In analyzing an experimental reflectivity data, an iterative procedure is started using Equation 3.37, where a model profile $\rho_m(z)$ is used to generate the initial model reflectivity $R_m(q_z)$. The deviation of $R_m(q_z)$ from the $R_e(q_z)$ is used in 3.37 to generate modified profile, $\rho_e(z)[= \int_0^z \rho'_e(z')dz']$. Model reflectivity profile

$R_m(q_z)$, for the next iteration is now calculated by setting $\rho_m(z)$ equal to $\rho_e(z)$ of the previous iteration with the assumption that the obtained derivative profile $\rho_e(z)$ is non-zero only in the interval $[0, T]$, where T is the total thickness of the film. The model reflectivity $R_m(q_z)$ can be calculated either by Master Formula or by Parratt Recursion formula. In the presence of large absorption, which is not included in the Born approximation, Parratt formalism should be used. The obtained EDP within the interval $[0, T]$ from this iterative scheme can only be said to be consistent with the reflectivity and may not be the unique solution. There are some particular conditions for which it is possible to extract the information regarding phase from the reflectivity data and have been discussed in some view graphs [159, 160, 161]. As the starting guess of the EDP is very close to the actual solution this technique is very useful to find the finer details of the EDP.

3.2 Development of Software for the fitting of Reflectivity data

We have developed a program to fit experimental X-ray reflectivity data using a freely available open source platform for numerical and scientific computing known as *Scilab* [162]. We have given a Graphical User Interface (GUI) to the program to make it more user friendly. The program is capable of fitting Neutron reflectivity data as well. A screen-shot of the GUI is shown in Figure 3.5. For the calculation of reflectivity both Parratt Recursion Formula and Inversion Scheme discussed in the previous subsection are included in the program. Two more methods namely, Reflectivity fitting using Distorted-Wave Born-Approximation (DWBA) and Model independent fitting, in which no apriori model EDP is required, are under construction and will be included in the program in future.

The GUI of the program has four section as shown in Figure 3.5. The top left section is for selecting the source i.e X-rays or Neutron. One needs to select one of them to proceed further. In the top right section one has to provide the wavelength of the source (for neutrons the default value should be kept as the program for neutron reflectivity is kept independent of wavelength), information about the

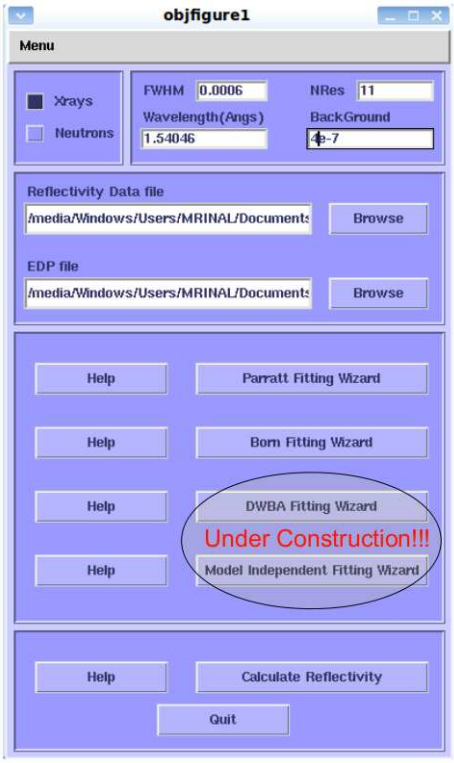

Figure 3.5: Screen-shot of the GUI developed to fit experimental reflectivity data.

resolution function i.e FWHM (Gaussian Resolution function), Nres (No .of points to carry out the convolution with Gaussian resolution function) and constant background. In the second section from the top of GUI one needs to provide the path of the experimental reflectivity data file (for example "datafile.dat") in two columns format (q_z,Reflectivity) and file (for example "EDPfile.dat") containing the initial information about the system (thickness, electron density, absorption factor of the layers and roughnesses of the interfaces separating the layers) in the format shown in Figure3.6. As shown in Figure 3.6, the file should contain eight columns and as many numbers of rows to describe the system. The columns names should not be included in the file. The first and last rows are for giving the information about the top layer and the substrate. P1-P4 are flags which can take integer values of either 1 or 0 depending on whether the values just in the left adjacent columns are used as fitting parameters or not. Both data file and EDP file must have the extension of ".dat". The fourth column of the GUI is provided for generating the reflectivity profile corresponding to the initial parameter values provided by the EDP file. In order to generate one just needs to click the "Calculate Reflectivity" button and within

d(Å)	P1	ρ(el/Å^3)	P2	β	P3	σ(Å)	P4
0	0	0	0	0	0	0	0
100	1	0.45	0	1.4E-8	0	3.0	1
1E6	0	0.71	0	1.7E-7	0	5.0	0

Figure 3.6: The format of the file containing the information about the parameters of the system to calculate the specular reflectivity.

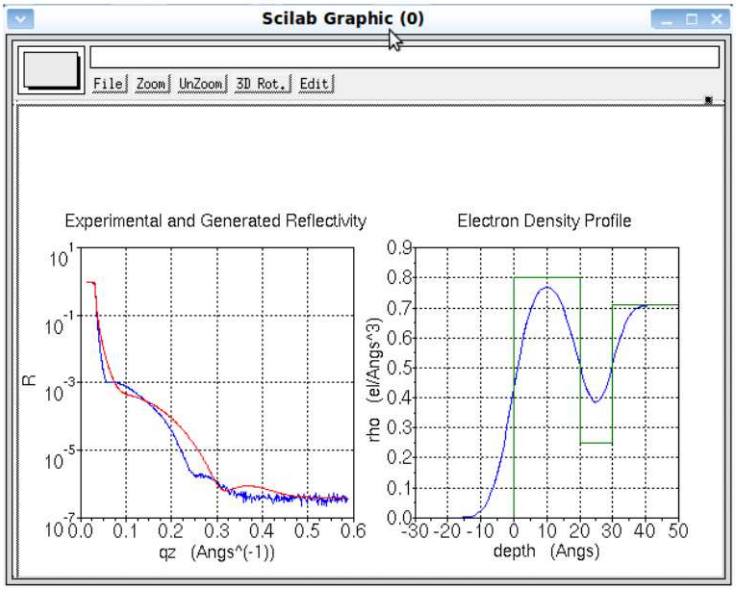

Figure 3.7: Graph showing the experimental , generated reflectivity data along with the electron density profile.

a second a graph showing the experimental data, the generated reflectivity along with the Electron Density profile will pop up as shown in Figure 3.7. The generated reflectivity and EDP file will be saved automatically (for example "datafile_gen.dat" and "EDPfile_gen_conv.dat)

The third third column of the GUI is for fitting the experimental reflectivity data either by Parratt Recursion formula or Born approximation as shown in Figure 3.5 by clicking the "Parratt Fitting Wizard" or "Born Fitting Wizard" respectively. "Parratt Fitting Wizard " will fit the data as per the parameters mentioned by the value of flags P1-P4 in the EDP file and pop-up a similar plot showing *fitted* reflectivity plot as well as EDP after fitting as shown as Figure 3.7. The fitted reflectivity and corresponding electron density will be saved automatically (for example "datafile_fit.dat" and "EDPfile_fit.dat"). When the "Born Fitting Wizard" is clicked a window opens up asking for the number of points to be used for using

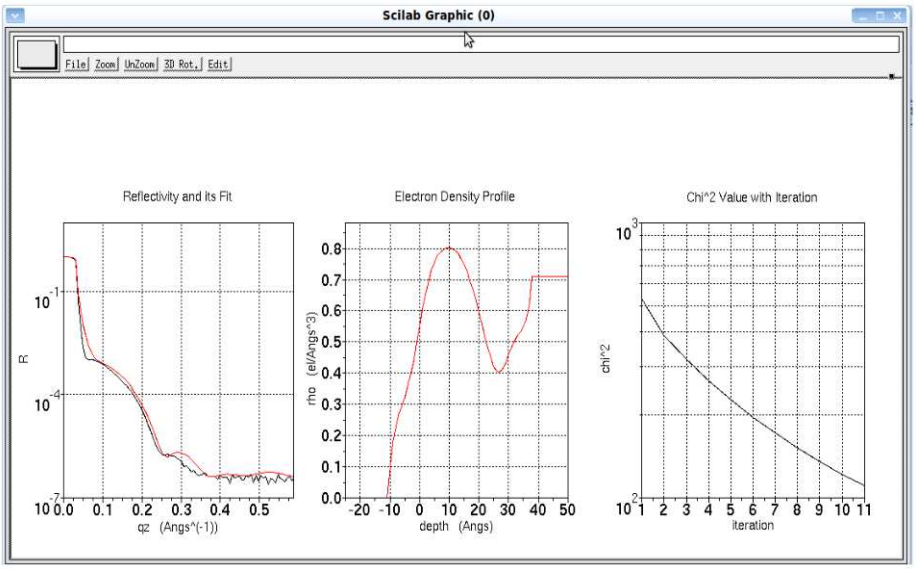

Figure 3.8: Graph showing the experimental , generated reflectivity data along with the electron density profile and the χ^2 value as a function of iterations.

Fourier transform and number of iterations to be done. One needs to provide a positive integer value which is multiple of 2 for the number of points and and positive integer also for the number of iterations. The one needs to click the "OK" button to proceed further and soon a graph showing three plots of reflectivity, electron density and χ^2 value with iterations will pop up as shown in Figure 3.8. The output files in this case will be automatically saved (for example "datafile_born_fit.dat" and "EDPfile_born.dat). The standard Fast Fourier Transform (FFT) routines available in Scilab are used for doing the Forward and Inverse Fourier transforms. In order to use the FFT package the experimental reflectivity data is first interpolated to have required number of points to give the finer details of the EDP when inverse transform is done. A model EDP of the film having thickness and electron density closed to the actual EDP is generated with as many points as the interpolated reflectivity data. The total thickness including the film and substrate is taken to be 2π times the inverse of $\triangle q_z$ (distance between neighbouring points in the interpolated data). The minimum distance between two adjacent points in EDP corresponds to 2π times the inverse of q_{zmax} (the maximum value of q_z in the interpolated data). In the iterative process using Equation 3.37 the part of the EDP corresponding to the film is only allowed to change and the electron density of the substrate are kept fixed

throughout the iterative process. At each iteration, the last point in the EDP near the substrate which is allowed to change is normalized to be equal to the density of the substrate. After each iteration Merit function (χ^2) is calculated and compared with its value in the previous iteration. The iteration procedure is continued for getting the minimum value of Merit function. The EDP for which is the minimum is reached is then said to be the EDP corresponding to the experimental reflectivity.

Testing the Inversion Scheme of the Software

Before applying the program, so developed to invert the experimental reflectivity data to obtain the actual EDP, it must be tested with some known EDPs. The testing is done on some reflectivity curves generated by Parratt formalism with known EDPs. The trial EDP for those cases are taken to be little bit different from the actual one. It is observed that after running few iterations of our program the actual EDP can be extracted from the trial one. Two systems are taken to check the efficiency of the scheme as well as the program. First system shown in Figure 3.9(a) is a bilayer system of thicknesses 50 Å each but different electron densities on silicon substrate. As a trial EDP again a bilayer system of same thicknesses is considered but with electron densities other than the actual one. This trial EDP is then fed to the program to generate the actual EDP and fit the reflectivity curve. In the second system shown in Figure 3.9(b) a film of thickness 100 Å is considered with oscillating electron density. The trial EDP for this case is taken to be a film of same thickness 100 Å but with uniform average density. The reflectivity curve so obtained after 30 iterations matches well with the generated reflectivity curve and the final EDP so obtained also fall on the actual EDP shown in the inset of Figure 3(b). These two examples showed that the scheme works very well to obtain an actual EDP starting from a trial EDP close to the actual one.

After successfully testing the program with the known EDPs the program can be used to obtain the actual EDPs from the experimental data. The first application of this inversion technique of the program is to invert the reflectivity data obtained from bare silicon surface. The reflectivity data is shown in Figure 3.10. The trial EDP consider here for fitting is silicon surface with electron density 0.71 el/Å^3 with

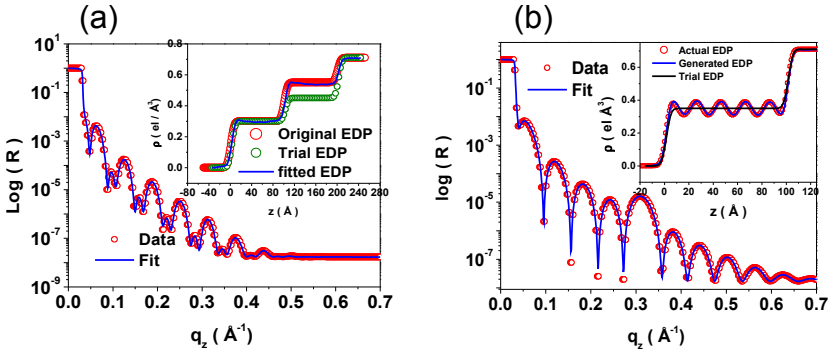

Figure 3.9: (a) Reflectivity calculated from Parratt formalism (symbols) and obtained after the inversion (solid line) of a bilayer system of thickness 50 Å each. Inset: The actual (red circles), trial (green circles) and EDP obtained after the successful inversion (solid lines). (b) Reflectivity calculated from Parratt formalism (symbols) and obtained after the inversion (solid line) of film of oscillating EDP of thickness 100 Å. Inset: The actual (red circles), trial (green circles) and EDP obtained after the successful inversion (solid lines).

roughness 4 Å. The EDP obtained after the minimization of the merit function is reached and shown in the inset of Figure 3.10. The electron density so obtained show that there a modulation of the electron density near the silicon surface.

3.3 X-ray Diffuse Scattering from Surfaces/Interfaces

In the previous section we dealt with Specular X-ray Reflectivity from smooth surfaces and interfaces. Although the effect of roughness is introduced by using Born approximation with a single parameter σ_n to define the surface/interface roughness. The roughness of a surface/interface manifests itself in the form of scattered intensities in the non-specular directions reducing the intensity in the specular direction and this scattering is termed as Diffuse Scattering. From the surfaces/interfaces on which the in-plane correlations are weak like solid surfaces, the diffuse scattering is weak and can be separated from the Specular component [156,148]. This is different in liquids for which the gravity determined length scale for roughness associated with *thermal capillary waves* is typically of the order of a millimeter. Since the reciprocal of this length is smaller than the spectrometer resolution, a major fraction of the intensity that is measured at the specular condition is due to diffuse scattering from thermal capillary waves [156, 112, 149, 148, 118].

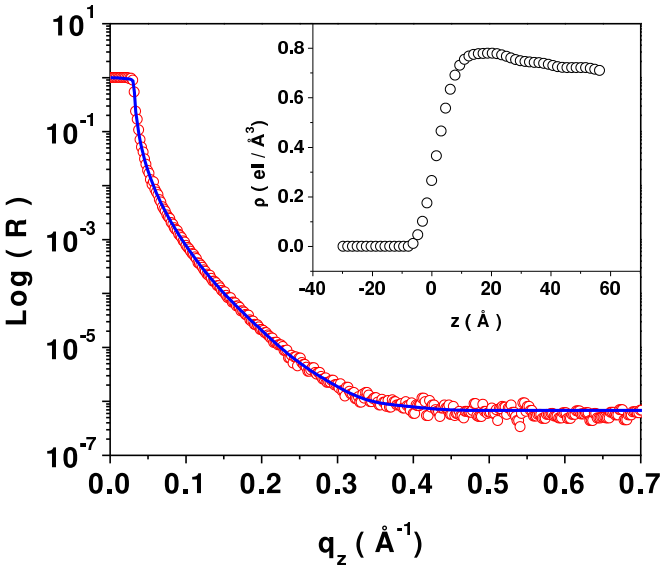

Figure 3.10: The reflectivity data (symbols) obtained from a bare silicon surface and the fit (solid line) after the convergence of Merit function. Inset: The EDP (symbol) obtained after fitting.

The manner in which surface/interface roughness gives rise to off-specular diffuse scattering is best discussed in terms of differential scattering cross section $d\sigma/d\Omega$ [148, 156, 117]. As the interaction of X-rays with with matter and hence calculation of differential scattering cross-section with Born approximation can give reasonable results. Under Born approximation the differential scattering cross-section can be written as

$$\frac{d\sigma}{d\Omega} = r_e^2 \left| \int d\vec{r}\rho(\vec{r}) \exp\left[i\vec{q}\cdot\vec{r}\right] \right|^2, \tag{3.38}$$

3.3.1 Scattering from a Single Surface/Interface

For a single interface defined by the height $h\left(\vec{r}(x,y)\right)$ as shown in Figure 3.11, the differential scattering cross-section can be written as

$$\frac{d\sigma}{d\Omega} = r_e^2\rho^2 \left| \int_{-\infty}^{h(x,y)} dz \exp[iq_z z] \int_{-\infty}^{+\infty} dx \exp[iq_x x] \int_{-\infty}^{+\infty} dy \exp[iq_y y] \right|^2, \tag{3.39}$$

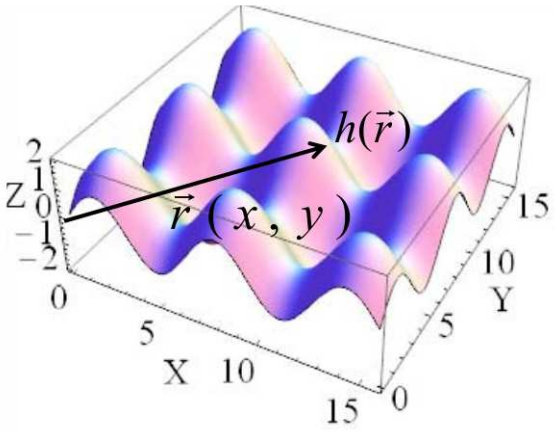

Figure 3.11: Schematics of Single interface defined by height $h(\vec{r}(x,y))$.

where ρ is the electron density of the medium having the interface. The above equation can be further simplified to

$$\frac{d\sigma}{d\Omega} = \frac{r_e^2\rho^2}{q_z^2}\int_{-\infty}^{+\infty} dxdy \int_{-\infty}^{+\infty} dx'dy' \exp[iq_z(h(x,y)-h(x',y'))] \times \exp[iq_x(x-x')]\exp[iq_y(y-y')], \quad (3.40)$$

In order to proceed further we need to introduce the statistical description of an interface. Considering the difference in heights for the interface at two different positions (x,y) and (x',y') as a *Gaussian Random Variable* [163], one can define a height difference correlation function as

$$g(X,Y) = \left\langle [h(x,y)-h(x',y')]^2 \right\rangle, \quad (3.41)$$

with $X = x - x'$ and $Y = y - y'$. Accordingly, a configuration average has to performed over all possible configurations of the interface to calculate the scattering cross-section. Then by performing appropriate change of variables one can write Equation 3.40 as [156, 148]

$$\frac{d\sigma}{d\Omega} = \frac{r_e^2\rho^2}{q_z^2}\mathcal{A}\int_{-\infty}^{\infty}\int_{-\infty}^{\infty} dXdY \exp\left[-\frac{q_z^2 g(X,Y)}{2}\right]\exp\left[iq_xX + iq_yY\right] \quad (3.42)$$

Here, $\mathcal{A}$ is the area of the interface illuminated by the incident beam. If the interfacial is statistically isotropic in the in-plane direction i.e $g(X,Y)$ can be written as

$g(r)$ with $r = \sqrt{X^2 + Y^2}$ (the radial in-plane co-ordinate), the above equation can take the form

$$\frac{d\sigma}{d\Omega} = \frac{2\pi r_e^2 \rho \mathcal{A}}{q_z^2} \int r \exp\left[-\frac{q_z^2 g(r)}{2}\right] J_0(q_{||} r) dr \tag{3.43}$$

Here, $J_0(x)$ is the zeroth order Bessel function with $q_{||}$ defined by Equation 3.7. Now we can calculate the differential scattering cross-section given by Equation 3.43 for surfaces of different types having different $g(r)$.

- *Ideally flat surface*: For totally flat surface, $g(r) = 0$, and scattering cross-section calculated form 3.42 becomes [156, 148]

$$\frac{d\sigma}{d\Omega} = \frac{4\pi^2 \rho^2 r_e^2}{q_z^2} \mathcal{A} \delta(q_x) \delta(q_y) \tag{3.44}$$

  where, $\delta(x)$'s are *Delta functions.*

- *Isotropically self-affine rough surface*: For an isotropically rough surface with a finite cut-off the height-height correlation can be written as [156, 148]

$$g(r) = A r^{2h} \tag{3.45}$$

  with h being the Hurst exponent with value between 0 and 1. The value of h determines how smooth or jagged as surface is. lower value of h shows the surface to be extremely jagged and higher values close to 1 means the surface is having smooth hill and valleys. Then the scattering cross-section can be calculated analytically with some particular values of $h = 1$ and $h = 0.5$ respectively as [156, 148]

$$\frac{d\sigma}{d\Omega} = \frac{A\pi \rho^2 r_e^2 \mathcal{A}}{\left[q_{||}^2 + (A q_z^2/2)^2\right]^{3/2}} \tag{3.46}$$

  and

$$\frac{d\sigma}{d\Omega} = \frac{2\pi \rho^2 r_e^2 \mathcal{A}}{A q_z^4} \exp[-q_{||}^2 / 2A q_z^2] \tag{3.47}$$

Liquid surfaces/Interfaces: In the intermediate length scales between the molecular size and gravity waves liquid surfaces/interfaces are mainly characterized by a long range correlations due to thermally excited capillary waves [148, 156, 112, 149]. Due to the capillary wave a liquid surface/interface has a logarithmic height-height correlation such that the height difference correlation function has the form [156]

$$g(r) = A + B\ln(r) \tag{3.48}$$

and corresponding scattering cross-section becomes

$$\frac{d\sigma}{d\Omega} = \frac{2\pi r_e^2 \rho^2 \mathcal{A}}{q_z^2} \exp[-q_z^2 A/2] \frac{2^{1-\eta}}{q_{||}^{2-\eta}} \frac{\Gamma(1-\eta/2)}{\Gamma(\eta/2)}, \tag{3.49}$$

where $\eta = Bq_z^2/2$. Apart from the finite size effects coming form the finite size of molecules and gravity waves in general X-ray scattering measurements are mainly limited by the length scale corresponding to the coherence length ζ of the photon. The effect of coherence length can be incorporated by convoluting the scattering cross-section with a Gaussian function having width ζ and cross-section becomes [156]

$$\frac{d\sigma}{d\Omega} = \frac{r_e^2 \rho^2 \mathcal{A}}{q_z^2} \exp[-q_z^2 A/2] \Gamma(1-\eta/2) \pi^{\eta/2} \zeta^{2-\eta} \Phi\left[(1-\eta/2); 1; -q_{||}^2 \zeta^2/4\pi^2\right] \tag{3.50}$$

where Φ is the Kummer Function [164].

3.3.2 Scattering from Multiple Interfaces

Like in the calculation of Specular reflectivity one needs to divide the film or interface into multilayer and calculate the scattering cross-section. In multilayer films, apart from in-plane correlation length discussed in previous section, another correlation length, ξ_z , in the growth direction comes into play. Generally, an interface in a multilayer film tends to follow the morphology of the interface just below it and if the total thickness of the film $d < \xi_z$, all the interfaces become statistically similar and the interfaces are called conformal [165, ?]. All the expressions for scattered intensity derived for single surface can be extended for multiple interfaces [165, 166]

with necessary modifications in the formalism.

For multilayer systems, where diffuse and specular components of scattered intensity cannot be separated, the scattering cross-section assuming conformal to the lowest layer's or substrate's surface can be written as [117]

$$\frac{d\sigma}{d\Omega} = \frac{2\pi r_e^2}{q_z^2} \sum_{i,j} \triangle\rho_i \triangle\rho_j \exp\left[iq_z(z_i - z_j)\right] \int r \exp\left[-\frac{q_z^2 g(r)}{2}\right] J_0(q_{||}r)dr \quad (3.51)$$

and in the continuum limit by using the reflectivity in the Born approximation [117], the cross-section for conformal multilayer can be approximated to

$$\frac{d\sigma}{d\Omega} = \frac{R(q_z)q_z}{2k_0} \int r \exp\left[-\frac{q_z^2 g(r)}{2}\right] J_0(q_{||}r)dr, \quad (3.52)$$

where $R(q_z)$ is the specular reflectivity of the multilayer and can be calculated using either Parratt Recursion Formula (Equation 3.22) or Master formula (Equation 3.36).

Born approximation gives reasonably good results if we are not calculating the scattering cross-section near the critical angle. Since around critical angle multiple-scattering comes into play one needs to go beyond Born approximation by using perturbation theory [156, 118, 148] and then the approximation is termed as Distorted-Wave Born Approximation (DWBA). In the first order DWBA, the scattering cross-section form an interface is a product of the cross-section with Born approximation (BA) and transmission coefficients (transmittance) between the two media separated by the interface (Equation 3.18) and written as [148, 118, 156]

$$\frac{d\sigma}{d\Omega}_{DWBA} = \left|t_{1,2}(\theta_i)\right|^2 \left|t_{2,1}(\theta_f)\right|^2 \frac{d\sigma}{d\Omega}_{BA} \quad (3.53)$$

In order to obtain an exact expression for intensity collected by the detector one needs to integrate the scattering cross-section, obtained either by BA or DWBA, over the solid angle, Ω_D, of the detector from the center of the sample and multiply it with the incident flux $I_0/\left(\mathcal{A}\sin\theta_i\right)$ as

$$I = \frac{I_0}{\mathcal{A}\sin\theta_i}\int_{\Omega_D}\frac{d\sigma}{d\Omega}d\Omega \tag{3.54}$$

The following techniques are generally employed to collect the diffuse scattering data from any interface:

1. *Grazing Incidence Small Angle X-ray Scattering (GISAXS)*: In this technique X-rays is allowed to incident on an interface with a grazing angle less than that of the critical angle of the interface and scattered intensities are measured as function of out-of-plane and in-plane angles. The necessary conditions are, $\theta_i < \theta_c$ and $(\theta_f,\phi) \neq 0$. This method is generally used to study to study non-crystalline systems and provides geometry, size distributions and spatial correlations on nanometer length scales. For this measurements either a Linear Position Sensitive Detector (PSD) or a two dimensional Area detectors are used.

2. *Grazing Incidence Diffraction (GID)*: This technique is similar to that of GISAXS in which the scattered intensity form any interface is measured as a function of in-plane angles provided the angle of incidence (θ_i) is less than or close to the critical angle (θ_c). This is done either by collecting the total count of a PSD detector as a function of in-plane angles. GID is used is used to study structure of two dimensional crystalline systems and gives information about lattice parameters, structure of molecules/nanoparticles, angle and azimuth of molecular tilt and in-plane correlations.

3. *Grazing Incidence X-ray Off-Specular Scattering (GIXOS)*: In this technique, the scattered intensity is measured as a function of the out-of-plane angles provided that the angle of incidence (θ_i) is less than or close to the critical angle (θ_c) and the in-plane angle (ϕ) is very close to zero. This measurement is considered to be the replacement of XRR to provide the information about electron distribution in the out-of-plane direction but only when the structures developed at the interface are conformal to the interface. The advantage of

this method is its ability to collect of data quickly and one can apply this method to study time dependent studies of a system having time dependent electron density distribution in the out-of-plane directions.

Chapter 4

Gold Nanoparticles on Air-Water Interface

4.1 Introduction

Chemically synthesized nanoparticles with a metal core surrounded by a dielectric ligand shell have received a lot of interest in recent years because of their unique electrical, magnetic and optical properties [17,167,43,44,21]. One of the major challenges to exploit these novel properties in nanotechnology is to form a dense monolayer film of these nanoparticles onto a chosen substrate. These ligand-stabilized nanoparticles have been found to self assemble on a substrate with the interdigitation of ligand shell up to its hard sphere limit [168]. The van der Waals interaction among the metal cores gives rise to an attractive force whereas the steric repulsion between the interdigitated thiol molecules balances it to form a stable structure on a substrate [169]. It is also known that for a large ratio of metal core diameter to ligand shell thickness a hexagonal ordered phase is obtained in deposited monolayers [170, 78]. But nanoparticles with smaller (few nanometers) diameter of metal core with organic capping of about 1 nm thickness, which exhibit interesting physical properties [17, 167, 43, 44, 21], do not exhibit long-range positional order and the coverage remains about 60% in the deposited monolayer films. Although several other techniques have been used earlier [170, 171], perhaps the best method for formation of monolayer film of these smaller nanoparticles is to transfer

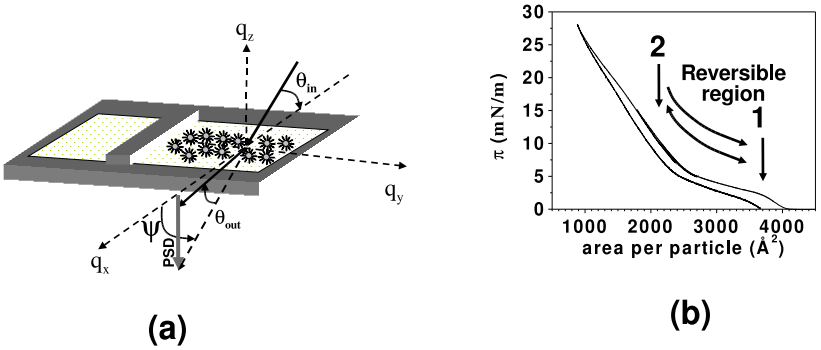

Figure 4.1: (a) Schematic diagram of the experimental arrangement. (b) Pressure-area isotherm of the Langmuir monolayer of gold nanoparticles. The vertical arrows marked 1 and 2 indicate the reversible region of the isotherm.

the Langmuir monolayer of nanoparticles from the air-water interface to a substrate following Langmuir-Blodgett (LB) deposition technique [21, 172, 80]. The packing density of a monolayer deposited using LB technique is expected to depend strongly on monolayer pressure on water surface ($\pi = \gamma_0 - \gamma$, with γ_0 being surface tension of bare (monolayer covered) water) at which the particles are transferred to a substrate. However it was observed that the morphology of the transferred monolayer films and coverage of nanoparticles (about 60%) remain almost the same for deposition over large reversible region (1 to 15 mN/m) of pressure-area isotherm of gold nanoparticles on water surface [80]. Films deposited at higher pressure (>15 mN/m) exhibit continuous formation of the second upper layer of gold nanoparticles. In this pressure range the measured isotherm also shows irreversibility [80] indicating the formation of the upper layer on the water surface itself, as reported in a study [61] of hydrophilic-shell–covered gold nanoparticles.

The primary purpose of this work is to understand the structure and morphology of the monolayer of thiol-capped gold nanoparticles (with ≈2 nm core and ≈1 nm thiol shell) on water surface over the large reversible region of isotherm (1–15 mN/m) and to develop a method to improve coverage of these nanoparticles in deposited monolayer films. Our results show that, before irreversible monolayer-to-bilayer transition, representing fracture or break, the monolayer of gold nanoparticles with hydrophobic thiol shell exhibits reversible buckling on water surface even at a relatively low surface pressure of 5 mN/m. Reversible buckling of monolayers of

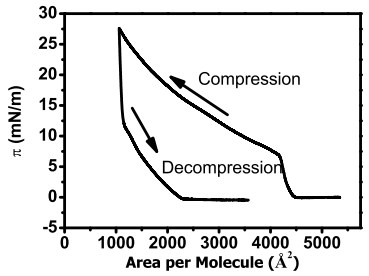

Figure 4.2: Pressure-area isotherm of the Langmuir monolayer of gold nanoparticles having gold core of 2.4 nm.

amphiphilic charged-neutral diblock copolymers on water at the air-water interface has been recently reported [173] at the moderate surface pressure of 15 mN/m. The buckled diblock copolymers however formed strips of width about 30 μm perpendicular to the direction of compression but no short-range order was observed. In our present study we found an in-plane Bragg peak that retains its position and exhibits an "arc" of intensity instead of a "rod" observed in two-dimensional systems. This occurs due to buckling of monolayers of gold nanoparticles on water under in-plane pressure —the "arc" of intensity reversibly come back to its original "rod" structure either with decompression or with thermal annealing at fixed monolayer pressure. We also present Atomic Force Microscopy (AFM) images which indicate remarkable improvement in surface coverage of the monolayer film deposited from the annealed compressed monolayer, though the monolayer breaks into circular patches.

In order to observe the effect of gold core size in the ordering and nature of buckling we also performed experiments with similar conditions on monolayer of gold nanoparticle with larger core diameter i.e 2.4 nm and same capping ligand i.e Dodecanethiol of length ∼1 nm. The pressure-area isotherm obtained with the monolayer of these nanoparticles is shown in Figure 4.2.

4.2 Experimental Details

Dodecanethiol-encapsulated gold nanoparticles were prepared by reducing an aqueous solution of hydrogen tetrachloroaurate ($HAuCl_4$) with sodium borohydride ($NaBH_4$) in the presence of tetra n-octyl ammonium bromide (TOABr) and Dodecanethiol

as described earlier in Chapter 2. Approximately 1 ml of the toluene solution of the gold nanoparticles (2 nm diameter) was spread on the water from a Millipore MilliQ system (resistivity >18 MΩ.cm) in a Langmuir trough (schematically shown in Figure 4.1(a)). The X-ray scattering measurement was performed at using a liquid spectrometer at the ID10B beamline of the European Synchrotron Radiation Facility (ESRF). The Langmuir trough was mounted on a diffractometer using an active anti vibration system and a 8.06 keV X-ray beam was used [75]. The surface-pressure area isotherm (refer to Figure 4.1(b)) was taken up to the pressure of 28 mN/m. The isotherm shows that up to the surface pressure of 15 mN/m (marked by the region between 1 and 2) the compression and decompression curves superimpose with each other. The hysteresis in the isotherm is evident when the film is decompressed from above 15 mN/m (in our case we decompressed from 28 mN/m).

The effect of gold core-size is evident from the different nature of isotherm with 2.4 nm gold core as compared to that of 2 nm. The X-ray scattering measurements namely XRR and GIXOS data collected from the monolayer of 2.4 nm gold nanoparticles on water surface at 10 °C are performed at 15-ID-C beamline of Advanced Photon Source, Argonne National Laboratory, USA.

4.3 Results and Discussions

We have shown in Figure 4.3(a) the normalized X-ray scattering intensity of a bare water surface and a water surface having a monolayer of gold nanoparticles at the two surface pressures of 1.0 mN/m and 10.0 mN/m as a function of $q_{||}$ by integrating position sensitive detector (PSD) data that provide q_z-dependence. The horizontal and vertical components of the wave-vector transfer $q_{||}$ and q_z are related to the out-of-plane and in-plane angles θ_f and ϕ(refer to Figure 1(a)) [112, 115, 117, 118]. Large diffuse scattering intensity with power law dependence on $q_{||}$ due to long-range capillary wave is evident in all the data shown in Figure 4.3(a). An in-plane Bragg peak was observed at 0.19 $Å^{-1}$ and the position of this peak was found to be almost independent of surface pressure. We have shown in Figure 4.3(b) the calculated and measured GIXOS profiles taken at in-plane angle ϕ= 0.11 degree for various surface

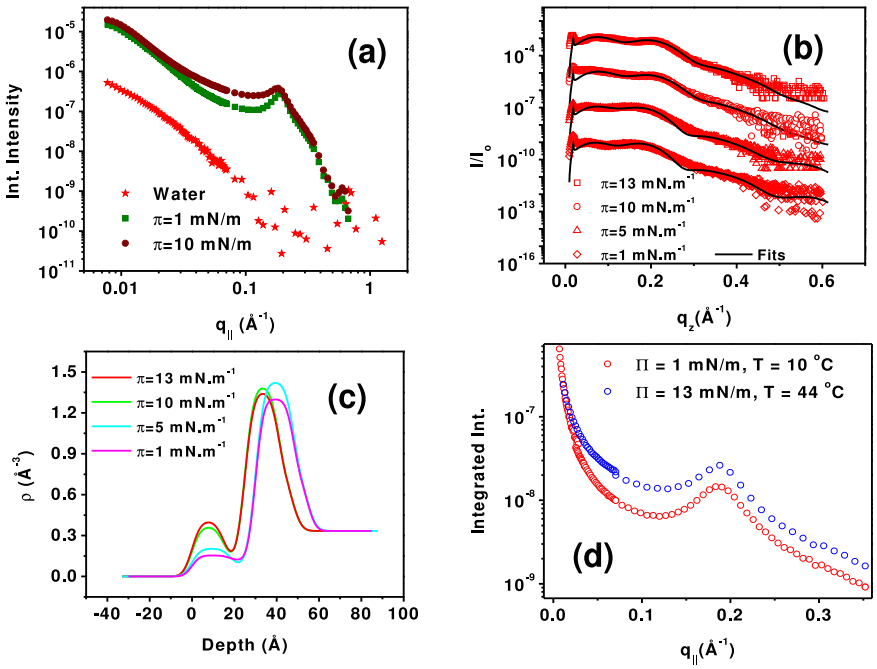

Figure 4.3: (a) The scattered intensity integrated over q_z plotted as a function of $q_{||}$ for bare water and nanoparticle-covered water at surface pressures of 1 mN/m and 10 mN/m. (b) The scattered intensity (symbol) as a function of q_z at ϕ=0.11 degree and the corresponding fitted curves (solid lines) for different surface pressures (1, 5, 10 and 13mN/m) (The curves are shifted vertically to improve clarity). (c) The EDP as a function of depth obtained by fitting for different surface pressures. (d) The integrated GID peaks (symbols) plotted as function of $q_{||}$ at surface pressures 1 mN/m with temperature 10 °C and 13 mN/m with temperature 44 °C.

pressures. The incidence angle θ_i was kept fixed at 0.19 degree and the data was collected far from specular condition ($\phi = 0$, $\theta_i = \theta_f$). We have assumed conformal interfaces and calculated the scattering cross-section away from specular condition as [112, 115, 117, 118]

$$\frac{d\sigma}{d\Omega} = \mathcal{A} \times \mathcal{G} \times F(q_z) \times \frac{2\pi}{q_z^2} \left[\frac{\exp[-\Gamma_e]}{q_{max}}\right]^{\eta} \frac{\Gamma(1-\eta/2)}{\Gamma(\eta/2)} q_{||}^{\eta-2} \tag{4.1}$$

Here $\mathcal{A}$ represents the area of scattering volume projected on the surface, which is fixed here by the incident slits and angle, $\mathcal{G}$ is the geometric function, which can be approximated by $\mathcal{G} = r_e^2 \rho_w^2 \left|t(\theta_i)\right|^2 \left|t(\theta_f)\right|^2 \cos^2\phi$. In Equation 4.1 is Γ_e (=0.5772) is the Euler constant, the transmission coefficients $t(\theta_i)$ ($t(\theta_f)$) represent the scattering intensity as the incident (scattered) angle approaches the critical angle, the $\cos^2\phi$ factor comes from the polarization of the incident and scattered beam and ρ_w is the electron density of water. The exponent which is also present in the Γ-functions can be written as [112] $\eta = Bq_z^2/2$ with $B = k_B T/(\pi\gamma)$ given by surface tension (γ) and temperature (T). The reciprocal of the size of nanoparticles multiplied by 2π was taken as the maximum wave vector q_{max} that sustains capillary wave. The derivative of x -y averaged electron density profile (EDP) $\rho(z)$ along depth (z) including the conformal roughness of the monolayer of gold nanoparticles on water are used to generate a good approximation [117] of the function $F(q_z)$ as

$$F(q_z) = \left|\frac{1}{\rho_w}\int \frac{d\rho}{dz}\exp[iq_z z]dz\right|^2 \tag{4.2}$$

Calculated GIXOS profiles at surface pressures 1.0, 5.0, 10.0, 13.0 mN/m are shown in Figure 4.3(b) with measured data and the corresponding EDPs of the film $\rho(z)$ as a function of depth are shown in Figure 4.3(c). From the fitting away from Yoneda wings [117, 118] of the data it is clear that for $<$ 5 mN/m the film remains primarily a monolayer. Above this pressure the electron density shows a bimodal distribution having the two centers separated by 30 Å. With the increase in surface pressure there is also an increase in number density of nanoparticles about the upper center. At higher pressures (10 and 13 mN/m) position of the

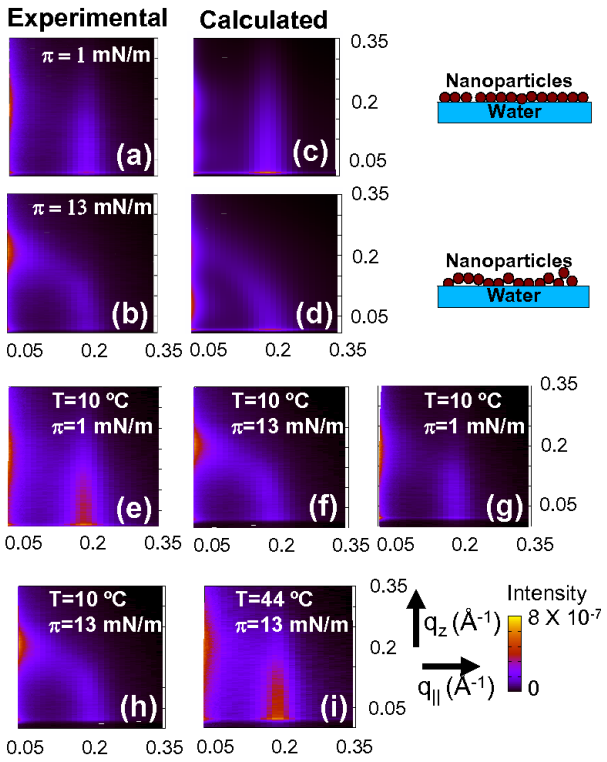

Figure 4.4: The ($q_{||}$—q_z) contour plots of measured data ((a) and (b)) and calculated intensity ((c) and (d)) for surface pressure 1 mN/m and 13 mN/m, respectively. The schematic of the models used to generate the calculated contour plots are shown beside (c) and (d), respectively. The scattered intensity is measured at 10 ℃ at surface pressures 1 mN/m (e) and 13 mN/m (f) during compression and 1 mN/m (g) during decompression. The scattered intensity at a surface pressure of 13 mN/m at the temperatures 10 ℃ (h) and 44 ℃ (i) is also shown. The horizontal and vertical arrows indicate the $q_{||}$ and q_z axes in $Å^{-1}$. The intensity scale is shown by the color bar.

top layer becomes more defined than that observed at lower pressures (1 and 5 mN/m) (refer to Figure 4.3(c)). It is evident that the electron density of the top layer increases systematically with the increase in surface pressure whereas for the bottom layer it remains almost unchanged. We also found that EDPs obtained for lower pressure and higher pressure is reversible in nature through compression-decompression cycles. This gives the initial evidence of buckling and the lower number density of top layer indicates coexistence of buckled and flat monolayer even at low surface pressure.

In Figure 4.4 we have shown some of the observed and calculated ($q_{||}$—q_z) contour plots of scattered intensity for different pressures and temperatures. For π=1 mN/m

(refer to Figure 4.4(a)), a Bragg rod is seen to be at $q_{||} = 0.19$ Å^{-1} indicating a purely two-dimensional nature of the nanoparticles on water surface at this low pressure. This is consistent with a model of a flat monolayer shown in the cartoon (beside Figure 4.4(c)). For the analysis of the GID peak and the Bragg rod the monolayer is assumed to be a free-standing 2D film composed of the identical spherical particles of radius R. Then for higher in-plane angles , Equation 4.1 becomes

$$\frac{d\sigma}{d\Omega} = \mathcal{A} \times \mathcal{G} \times F(q_z) \times \rho \left\langle 1 + 2\pi\rho \int [g(r_{||}) - 1] J_0(q_{||} r) r_{||} dr_{||} \right\rangle \tag{4.3}$$

where, $F(q) = [\sin(qR) - qR\cos(qR)]^2 / (q)^6$, is the form factor due to the spherical shape of the particles, ρ being the electron density of gold. Here $\langle\rangle$ stands for averaging over fluctuations in the incidence angle in between the incident beam and the locally buckled film (refer to the cartoon beside Figure 4.4(d)) and the fluctuations are considered to be Gaussian in our calculation. In the above expression $g(r_{||})$ is the conventional 2D isotropic pair distribution function (PDF) and we have used an analytical form of the PDF [174] here as

$$\begin{aligned} g(r_{||}) &= 1 + \frac{\chi - 1 + \lambda}{y^m} + \frac{(y - 1 + \lambda)\exp[-\alpha(y-1)]}{y} \\ &\quad \times \cos[2\pi(y-1)] \text{ for } m \geq 1, y \geq 1 \\ &= \chi \exp[-t(y-1)^2] \text{ for } y < 1, \end{aligned} \tag{4.4}$$

where $y = r_{||}/d$, $\alpha = 2\pi d/\xi$. Here d, ξ are the lattice constant and correlation length of the structures formed by the particles.

We performed first a detailed analysis (refer to Figure 4.5(a)) of the GID peak at 0.19 Å^{-1} and its intensity profile along q_z (refer to Figure 4.5(b)) for the surface pressure 1mN/m using Equation 4.3 and 4.4. The width of the Gaussian distribution used for averaging is taken to be zero assuming a flat monolayer at low surface pressure. The center-center distance of gold nanoparticles obtained from the GID peak comes out to be 34 Å. This distance indicates interdigitation [168] of thiol chains as two of them, each having fully extended chain length 14.4 Å, are squeezed within 15.0 Å. The broadening of the in-plane peak indicates the absence of long-range order as

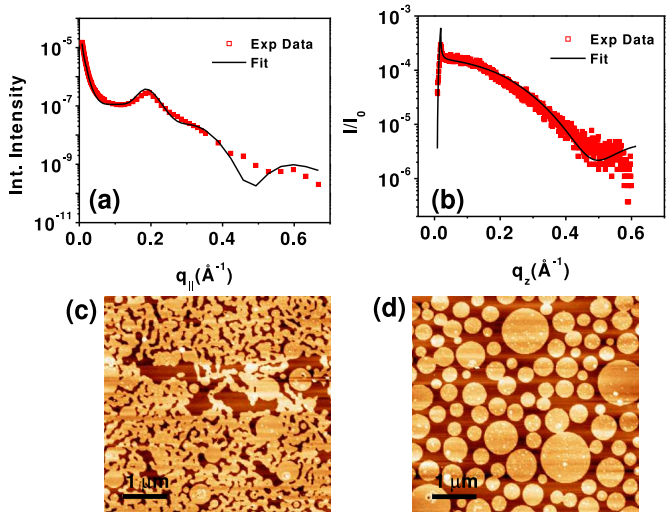

Figure 4.5: (a) The integrated GID peak (symbols) plotted as a function of $q_{||}$ at surface pressure 1.0 mN/m and the fit (solid line) from our model. (b) The Bragg rod (symbols) plotted as a function of q_z and the corresponding fit (solid line) from our model. (c) The AFM images of the film of gold nanoparticles horizontally deposited from LB trough on a silicon surface with surface pressure 13mN/m and temperature 16 °C and (d) with same surface pressure but with temperature 33 °C.

expected for the core-shell ratio used here. The correlation length of the structure formed by the particles is found to be 140 Å. At higher surface pressure (π= 13 mN/m), the Bragg rod shows "arc formation" in the $q_{||} - q_z$ plane (refer to Figure 4.4(b)). This type of contours, similar to that observed in "powder patterns", can be generated either from randomly oriented three-dimensional crystallites or from a buckled monolayer as shown in the model (beside Figure 4.4(d)). The existence of the three-dimensional crystallites, as observed in vapour-deposited [170] or dip-coated [171] films, is ruled out in our case from the low-$q_{||}$ results shown in Figure 4.3. Moreover, crystallite formation is essentially an irreversible process and the reversibility observed here rules this out completely. The formation of regular strips like in buckled diblock copolymers [173] is also ruled out because of the random nature of the locally buckled monolayer of nanoparticles. Moreover, the correlation length of the structures formed by the nanoparticles is much less in comparison to the width of the strips for copolymers. The reversibility of the buckled monolayer is confirmed by taking the monolayer through a compression-decompression cycle. In the first sequence of Figure 4.4(e)-(g) we have followed a compression (from 1

mN/m to 13 mN/m) and a decompression (back to 1mN/m) of the monolayer. The intensity contour in the $(q_{||} - q_z)$ space exhibited continuous transition from "rod" to "arc" formation as the monolayer is buckled. Hence, the only explanation of the observed "arc formation" in the scattered intensity contour can be the buckling of the gold monolayer on water surface.

We have calculated the scattered intensities for large $q_{||}$ values for both the flat and buckled monolayers by using the information obtained from the fitting of Bragg rod and GID peak at low surface pressure. In case of buckled monolayer the averaging over fluctuations in incidence angle is done with a Gaussian distribution of finite width of about 30 degrees. The calculated intensity contour (refer to Figure 4.4(c) and (d)) matches well with measured data (refer to Figure 4.4(a) and (b)). In Figure 4.4(h)-(i), we have shown that a buckled monolayer can be annealed by raising the temperature from 10 ℃ to 44 ℃. Then the two-dimensional nature of the monolayer is regained, exhibiting the Bragg rod in the scattered intensity contour. We also found that there is an increase in intensity (refer to 4.3(d)) of the GID peak from the annealed monolayer which clearly demonstrates a higher packing fraction of the monolayer. Both our observations of reversal of monolayer buckling and increase in packing fraction by thermal annealing may provide a route to improve the coverage of nanoparticles in a monolayer. This enhancement in coverage is further investigated by transferring the monolayers of gold nanoparticles on a silicon substrate by horizontal deposition [75] with a fixed surface pressure of 13 mN/m at two different temperatures 16 ℃ and 33 ℃. The AFM images of the as-deposited films (Figure 4.5 (c),(d)) clearly show that at 16 ℃ the nanoparticles form percolating structures while for films deposited at 33 ℃ these percolating structure are replaced by well-separated bigger compact islands. Due to the release of in-plane pressure on the monolayer after deposition the compressed film breaks in to circular islands. In order to understand the structure of the monolayer film of these gold nanoparticles transferred onto a Solid substrate from air-water interface a study is carried out and presented in the next Chapter of this thesis.

The XRR data collected from monolayer of gold nanoparticles having gold-core of 2.4 nm are shown in Figure 4.6(a). The data were collected at different surface

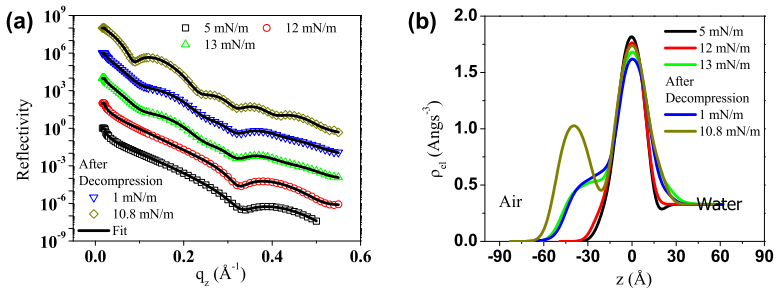

Figure 4.6: (a) XRR data obtained from monolayer of nanoparticles having 2.4 nm gold-core at different pressures 5 mN/m , 12 mN/m , 13 mN/m during compression and 1 mN/m, 10.8 mN/m after decompression. Both data and corresponding fitted curves were multiplied by factors of 10 for clarity. (b) The electron density profiles obtained from the fitting of the XRR data (shown as solid lines) collected at different pressures.

pressures during the first and second compression cycles after decompressing the film to the maximum possible area of the trough to check the reversibility. From the data itself it is quite clear that the monolayer nature of gold nanoparticles changes when compressed up to 13 mN/m and retains its nature even after total decompression. We fitted the reflectivity data with Parratt Formalism as discussed in Chapter 3 using discrete box model. The EDP obtained from the fitting is shown in Figure4.6(b) along with the fitted curves in 4.6(b). The EDPs show that the film remain as monolayer till the surface pressure is below 13 mN/m and it undergoes a transition from monolayer to bilayer at 13 mN/m and the transition is not reversible unlike the gold nanoparticles with 2 nm gold cores. When the film is decompressed after attaining surface pressure 13 mN/m the bilayer structure remained intact and become more prominent when the pressure is increased in the second compression cycle to 10.8 mN/m.

We have also collected GIXOS data for the monolayer of 2.4 nm gold nanoparticles at the same surface pressures for reflectivity data and shown in Figure 4.7. A peak around $q_z = 0.15$ Å^{-1}is observed when the surface pressure is increase to 12 mN/m and become prominent for higher surface pressure. The appearance of this peak is due to the formation of out-of-plane movement of nanoparticles and becomes strong when bilayer forms. The most interesting observation here is the data col-

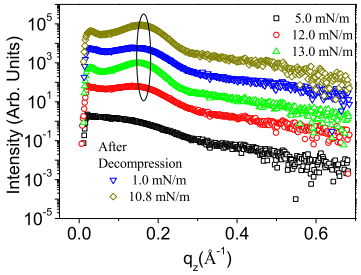

Figure 4.7: GIXOS data collected at in-plane angle ϕ=0.3 $^\circ$ with different surface pressures 5 mN/m, 12 mN/m, 13 mN/m during first compression cycle and 1 mN/m, 10.8 mN/m during second compression cycle after decompression.. The peaks around $q_z = 0.15$ Å^{-1} are highlighted by an ellipse.

lected at 12 mN/m. From the reflectivity data we know the film is monolayer but the appearance of the peak at $q_z = 0.15$ Å^{-1}indicate the out-of-plane movements of the nanoparticles. These observations show that the monolayer of 2.4 gold nanoparticles becomes bilayer above 13 mN/m and undergoes through a buckled phase from monolayer phase at 12 mN/m.

4.4 Conclusions

We have shown that monolayer films of organic capped gold nanoparticles of 2 nm exhibit buckling of different kind than copolymers on water surface over a large portion of the pressure-area isotherm. This buckled phase is reversible in nature and can be annealed thermally below 15 mN/m. The stored energy in the buckled phase forces the film to relax as the film is transferred on to a substrate from the air-water interface. This explains the observation of about 60% coverage of nanoparticles in the LB films deposited over a wide range of the isotherm. We have demonstrated a possible route to improve the coverage of the deposited monolayer film of these technologically important nanoparticles. We have also shown that when the size of the gold core is increased from 2 nm to 2.4 nm the monolayer formed by them does not show reversible region in the pressure-area isotherm. We have shown that the monolayer of 2.4 gold nanoparticles exhibits a buckled phase below 13 mN/m and undergoes bilayer transition beyond that.

Chapter 5

Gold Nanoparticles on Air-Solid Interfaces

5.1 Introduction

Till date the research on metallic nanoparticles showed [19, 21, 22, 20, 6, 45, 44, 43, 22, 25, 175] us that how important is to find out the ways to anchored them on a solid substrate to use them in possible device applications. In the last Chapter, I have discussed our studies on the structural properties of thiol encapsulated gold nanoparticles on air-water interface and showed a possible route to increase their coverage. But between the formation of a stable film of these nanoparticles on a substrate, either by transferring them from air-water interface or by spun casting, there lies many phenomena like drying of underlying water or solvent molecules and the random movements of the nanoparticles which can change the structure of the monolayer of the nanoparticles after deposition.

It is known that during the self-assembling processes of colloidal systems like thiol encapsulated gold nanoparticles, internal stress is generated by drying/de-wetting forces as well as the underlying interfacial interactions [176] which induces patterning in monolayers of such colloids when transferred over solid substrate [85, 68, 87]. Self-assembling processes are universal in nature and a lot of materials with vastly different physical properties are known to self-assemble in a very similar fashion. A lot of interest has been aroused lately on the self and directed-assembly

of gold nanoparticles. Sequence of structural transformation from n$\triangle \rightarrow$(n+1)$\square$ $\rightarrow$ (n+1)$\triangle$, of such colloidal systems when trapped within optically flat surfaces have been observed with increasing separation between the surfaces [99, 100]. Here n is the number of layers and $\triangle$ and $\square$ are layers corresponding to triangular and square symmetry respectively. It is known from various experiments [61, 177, 90] and the results presented in the last Chapter of our thesis that monolayer of gold nanoparticles generally form two dimensional Hexagonal Closed Packed (HCP) structure. There are no reports yet to the best of our knowledge regarding the structure of the monolayer of gold nanoparticles just after transferring them on to a solid substrate. In this Chapter, I discussed some of our X-ray scattering results to show the structural transitions in the monolayer of gold nanoparticles with time, when transferred on to a Silicon substrate.

On the other hand, metallic nanoparticles decorated inside polymer matrices are the new generation materials, having novel electronic, magnetic and mechanical properties [178, 179, 180] . The presence of long chain macromolecules like polymers alters the external environment of the nanoparticles resulting in change of the interaction amongst them [101, 102]. There are many experimental observations [103] in which the non-adsorbing polymer environment induces phase separation of the colloidal particles dispersed in it. The depletion of polymer molecules from the inter-particle region leads to an attractive force between the particles [101, 103]. The nature of the interacting force becomes more complex when nanoparticles are deposited on a thin polymer film. The inhomogeneous nature of the polymer-air interface leads to movement of the nanoparticles on or inside the polymer film. In plane diffusion of gold atoms on polystyrene films to form nanoparticles is already reported in many studies [104, 105] either by annealing or waiting for long time. The out-of-plane movement of nanoparticles inside a polymer thin film is used in many studies to probe the glass transition temperature [181] and viscoelasticity [182] of polymer surfaces with temperature. These in-plane and out-of-plane movements are the results of diffusion of some complex kind. Recently by using resonanced enhanced x-ray scattering [106] and x-ray photoelectron spectroscopy [107] the motion of gold nanoparticles embedded in a hydrophobic polymer matrix of polystyrene has

been studied. The results show that the in-plane diffusion coefficient of nanoparticles is 1 order of magnitude larger than the out-of-plane and diffusion dynamics differ from Stokes-Einstein Brownian motion. In all the studies above the diffusion of the nanoparticles are observed near the glass-transition temperature of the polymer matrix. Due to complex interactions it is interesting to monitor the dynamics of monolayer of gold nanoparticles on a thin polymer surface. So I have also included in this Chapter, our study on dynamics of monolayer of gold nanoparticle thin film to demonstrate a morphological transformation of structures formed by them when dispersed on a surface of hydrophobic thin Polyacrylamide film at normal temperature and pressure (NTP) and is interesting because of its direct possible applications. Though the polymer matrix is hydrophobic but under constant temperature, pressure and humidity conditions the morphology of the polymer film does not change with time. We deposited an monolayer of thiol passivated gold nanoparticles on a polyacrylamide film and perform both x-ray reflectivity (XRR) measurements and atomic force measurements (AFM) to probe the morphological changes of the monolayer of nanoparticles.

5.2 Gold Nanoparticles on Si Substrate

5.2.1 Experimental Details

About 200 μL of toluene solution containing gold nanoparticles having gold-core of size ~2.4 nm with concentration of 0.44 mg/mL was spread carefully on a Langmuir trough (KSV, Mini-Micro) placed on an anti-vibration device over the spectrometer. The X-ray scattering experiments were performed on the liquid spectrometer using linear position sensitive detector (PSD) at ID10B, Troika II beamline, European Synchrotron Radiation Facility (ESRF), using high energy (8 KeV, λ =1.54 Å) synchrotron source. To facilitate measurements from the transferred film of nanoparticle on a substrate, a bare hydrophillized Si substrate mounted on the dipper unit of the Langmuir trough was aligned with respect to the incident X-ray beam. The pre-alignment ensured that once the monolayer is transferred, the measurements could be performed instantaneously. After the alignment, the substrate was sub-

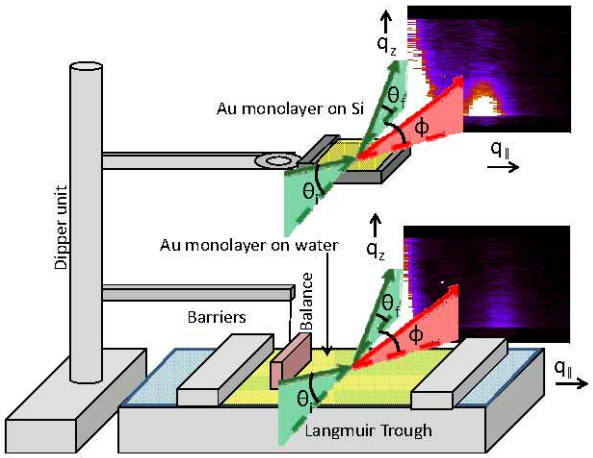

Figure 5.1: Schematic representation of the experimental setup. The substrate was dipped inside the water before the particles were spread. The monolayer was compressed and data taken from the water surface initially. The substrate was then lifted out and the measurements were performed on the transferred monolayer as a function of time.

merged below the air-water interface and the solution containing gold nanoparticles dispersed in toluene solution was spread over the water surface. Once the toluene evaporated, the barriers were compressed slowly (at a speed of 1 mm/min) to attain a target pressure of 3 mN/m. On achieving the target pressure, scattering measurements were performed on the monolayer of nanoparticles at the air-water interface. The monolayer was then transferred to the substrate at the same pressure by horizontal deposition technique [75] by pulling out the substrate slowly at a speed of 1 mm/min and scattering measurements were performed repeatedly at frequent intervals of time. The scattering measurements were performed by collecting the scattered intensity from the monolayer, either from water surface or Si substrate, as function of in-plane (ϕ) and out of plane (θ_f) angles by using a Linear Position Sensitive Detector (PSD). The incident angles for both of the measurements performed on water surface and silicon substrate are kept fixed at 0.13 degrees which is less than the critical angle of water (0.15 degrees) and Si (0.22 degrees). This condition is maintained in order to get the scattering information mainly from the surface due to low penetration of X-rays below the critical angle. The scattered intensities are then plotted as function of in-plane and outof- plane components ($q_{||}$, q_z) of the wave transfer vector ($\vec{q}$) which are related to the in-plane and out-of-plane

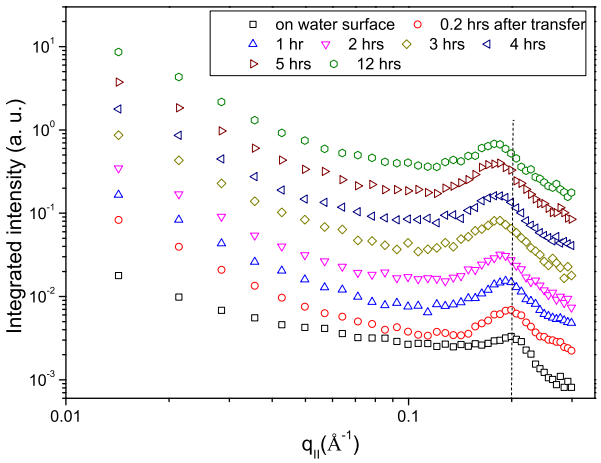

Figure 5.2: GID plots obtained from monolayer of gold nanoparticles transferred on to Si substrate. The peak shifts towards the lower in-plane momentum transfer value.

angles respectively [18] as shown in Figure 5.1. In order to obtain the GID data, which provides in-plane correlation of the the nanoparticles, we integrated over the whole length of PSD (i.e integrated over the entire range of θ_f or q_z) and plotted the integrated intensities as a function of $q_{||}$. We performed AFM measurements of a transferred film of these gold nanoparticles with time. The measurements were done in the tapping mode using etched Silicon Nitride cantilevers to minimize tip-induced damages.

5.2.2 Results and Discussions

In Figure 5.2, we have shown GID plots of scattered data collected from monolayer of gold nanoparticles on both water surface as well as Si substrate as a function of time. There are two important observations. Firstly, there is a power law region at low $q_{||}$ values and the slope in log-log plot of which is found to change when the nanoparticles are transferred from water to Si surface and remained fixed after that. Secondly, the peak due to correlation between nanoparticles at $q_{||}$ =0.197 $Å^{-1}$ is found to change its position gradually after transferring to the Si substrate from 0.197 $Å^{-1}$ to 0.180 $Å^{-1}$. The power law behavior of the GID plots indicate a long range correlation of the average interface formed between the monolayer of gold nanoparticles and air. This long range correlation can be due to the capillary wave

fluctuations on water surface [112] and arrested capillary wave fluctuations [117] on Si substrates. As our main theme of this experiment is to study the structural changes of the monolayer of the gold nanoparticles when transferred on to a solid substrate as a function of time, we focused ourselves to the analysis of in-plane correlation peak only.

It is known that gold nanoparticles prefer a hexagonal closed-pack (HCP) array when floating over water as a monolayer [61,177,90]. For a HCP structure, the correlation peak should correspond to$\sqrt{3}/2$ times the nearest neighbour distance (a) and appear at $q_{||} = 2\pi/d_{liq}$ with d_{liq}=$\sqrt{3}a/2$. The separation between the nanoparticles in the monolayer on water surface from our experiment came out as 37 Å corresponding to $d_{liq} = 32$ Å. The peak remained stationary immediately after transfer of the monolayer from the water surface to the Si surface, but started shifting towards the lower $q_{||}$ value with time as shown in Figure 5.2. Systematic changes were observed for the peak position at 0.2 hrs, 1 hr, 2 hrs, 3 hrs and 4 hrs. After 5 hrs the peak shifted to a $q_{||}$ value of 0.18 Å^{-1} and there was no more shift in the peak position even after 12 hrs. The width of the peaks were almost constant throughout the process of stabilization of the structure. The separation of the nanoparticles after 5 hours of transfer to Si (d_{5th}^{sol}) corresponding to the peak position of $q_{||}$ at 0.18 Å^{-1} comes out to be 35 Å. The ratio d_{5th}^{sol}/d_{liq} is found to be 0.9 and close to the ratio of the nearest-neighbor distance in the hexagonal array to that in the Square Lattice (SL) ($d_{HCP}/d_{SL} = \sqrt{3}/2 = 0.87$). The shift in the peak position towards lower $q_{||}$ value, signifies that the inter-particle distance has increased and more interestingly, the value of the initial, intermittent and final values of the inter-particle spacing imply a smooth crossover from a 2-D hexagonal structure to a square structure.

In order to do quantitative analysis of the correlation peaks we fitted the peaks after a linear background subtraction with a pair of Lorentzians corresponding to the peaks for HCP and SL. A reasonable fit to the peaks were obtained by the sum of these Lorentzian functions with fixed centers at 0.197 Å^{-1} (say L_1) and 0.18 Å^{-1} (say L_2) and fixed width as shown in Figure 5.3. The factors determining the height of the two Lorentzian functions, which provide information about the fraction of domains which correspond to the area occupied by the square (f_{SL}) or

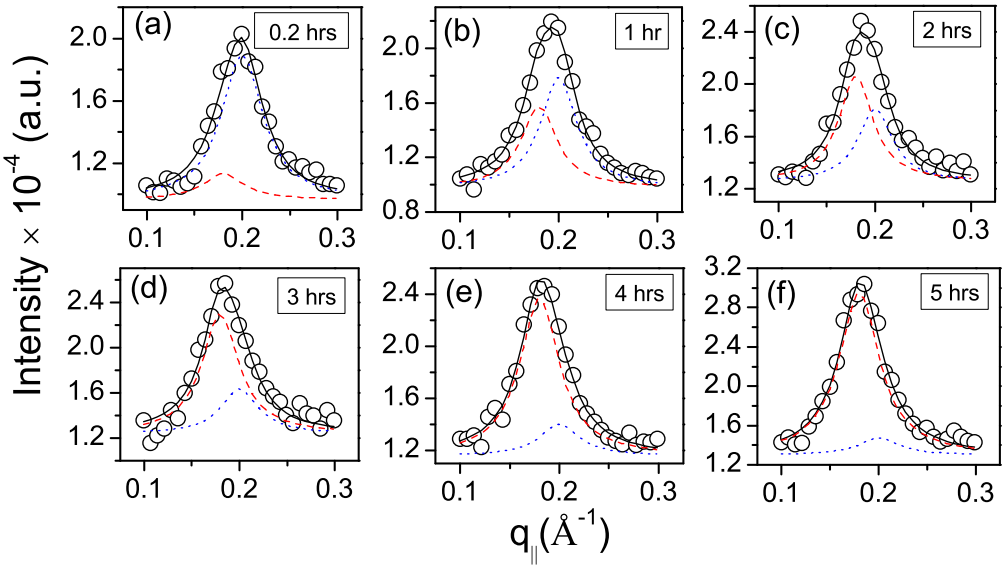

Figure 5.3: The peaks fitted with the sum of two Lorentzian functions with centers fixed at 0.197 $Å^{-1}$ and 0.18 $Å^{-1}$. The contribution to the peak just after transfer from the hexagonal closed pack structure (L_1) is dominant in (a) but with time it becomes weak and the contribution from (L_2) corresponding to the square lattice becomes stronger (b-e) until it is dominant in (f).

the hexagonal lattice ($f_{HCP}(= 1 - f_{SL})$), were taken such that the sum of the factors would be unity. We see that immediately after transfer, the major contribution to the peak comes from L_1 where the particles are in the hexagonal ordering with very small contribution from L_2 where the particles are in square symmetry. However, the number of domains corresponding to the square symmetry increases with time until it is dominant after 5 hours of transfer.

Fig. 5 demonstrates the increase in the domain population corresponding to the square symmetry (f_{SL}) as a function of time. The width of L_1 and L_2 were fixed around 0.1 $Å^{-1}$. This immediately suggests that although the fraction of domains in the square lattice arrangement increase in time, the correlation length of the domains (given by the width of the Lorentzian) remains unchanged. This implies the formation of a large number of small domains corresponding to the square lattice packing which are correlated over a small length scale. Although the structural transition proceeds over a substantial period of time and we find that almost all particles which were initially hexagonal close-packed are now rearranged into square packing, the fact that the correlation length remains unchanged, that is to say that

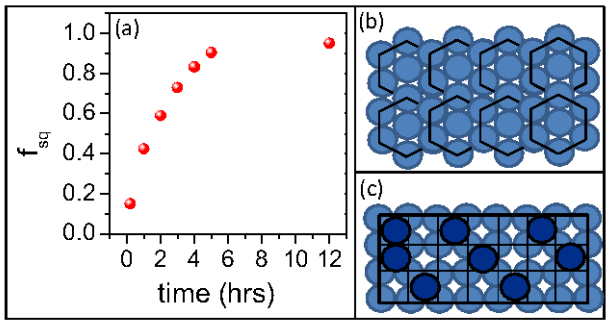

Figure 5.4: (a) Population fraction (f_{SL}) of the domains corresponding to the square symmetry. 1-f_{SL} denotes the contribution from the particles in hexagonal symmetry. (b) and (c) represent the initial and final configuration of the particles as a result of structural transition from hexagonal to square lattice packing.

the domains do not grow beyond a certain length scale, is not surprising. There are a considerably high regions of the monolayer which are rendered non-affine and/or inaccessible due to inhomogeneous lateral pressure which builds up as the drying proceeds. The presence of numerous jammed sites [93] created by fast evaporation of the liquid also obstruct any kind of movement of the nanoparticles. This restricts the domain growth beyond a certain limit.

Apart from the fact that the correlation peak shifts towards lower $q_{||}$ value we also observe that the intensity of the correlation peak increases as the monolayer dries (see upper panel of Figure 5.5). A plausible explanation seems to be due to the fact that the vibration of the nanoparticles about their mean positions which contributes to the Debye-Waller term [122] is enhanced due to the presence of trapped water causing blurring and suppression of the scattered intensity. As the water dries-off with time, the fluctuations are arrested, leading to the observed increment in the intensity. The fall of the intensity as a function of q_z was plotted for different times sitting at the Bragg rod as shown in the lower panel of Figure 5.5. We have used the form factor of the nanoparticle to fit the data. We did not observe any change in the nature of the q_z scans at the Bragg rods although there appears to be some material movement in the out-of-plane direction, however the form factor of the nanoparticles used to fit the data corresponds to a value of 2.6 nm, which is quite close to the value obtained from TEM measurements as discussed in 2.

Successive AFM measurements, as shown in Figure 5.6, were also performed on

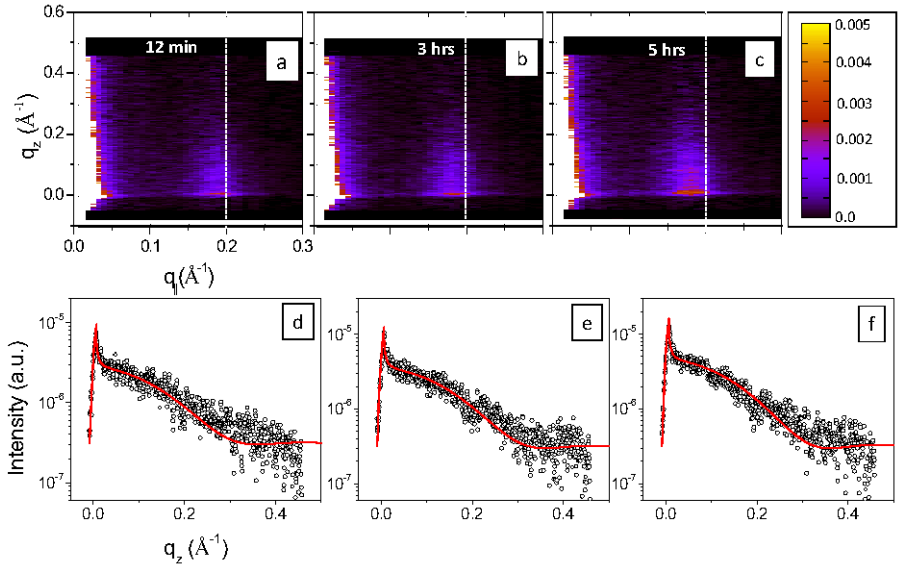

Figure 5.5: The 2D X-ray scattering profile of the monolayer on substrate as a function of $q_{||}$ and q_z. The peak shifts towards low in-plane momentum transfer value and becomes stronger with time. Lower panel (scattered plots) depicts the fall of intensity with q_z sitting on the Bragg rod. The corresponding fits (solid line) are done using the form factor of the nanoparticle.

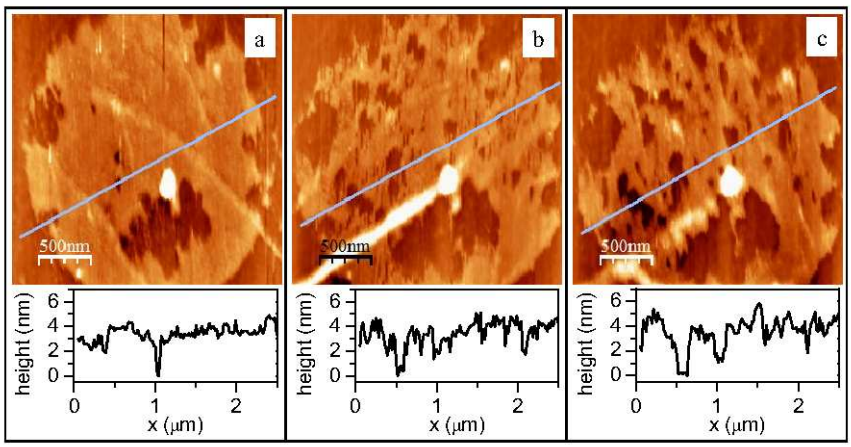

Figure 5.6: Successive AFM images of the monolayer acquired as a function of time. (a) is after 1 hour, (b) after 3 hours and (c) after 6 hours of transfer. The area occupied by the monolayer on the substrate decreases with time but the fraction of particles constituting the bilayer increases. Shown below are the typical line profiles of the scans.

the sample immediately after transfer at an interval of 30 minutes. We see that initially there is a large cluster of gold nanoparticles but after some time pin-holes start appearing within them. Images at later stage of time show that these pinhole keep growing in dimension and finally we see that the cluster assumes a patterned look. The coverage area of the sample decreases but the average height of the film increases (as evidenced by the line profiles in the lower panels of Figure 5.6). From AFM analysis [183] it is observed that the coverage of the monolayer is 76% in the first hour, 67% in the third hour and 60% in the sixth hour. The occupied area is depleted by growth of holes and there is an increment in the fraction of particles constituting the bi-layer as a function of time. The ratio of the area covered by the monolayer in the first hour to that in the sixth hour comes out to be 1.27:1. If we assume that initially the nanoparticles in the monolayer were arranged in a HCP structure and in about six hours they re-organize into rectangular structure (formed out of two adjacent SL) due to changes in the lattice induced by lateral pressure due to nucleation and growth of holes in the islands, the ratio of the occupied area comes out to be $Area_{HCP} : 2Area_{SL} = 1.3 : 1$. Here we assume that the number density of the nanoparticles is conserved, so six of the nanoparticles initially at the vertices of the HCP structure will form two adjacent SL structure and the one at the center is pushed out as an overlayer. This is also a direct evidence of the fact that during the process of drying, the particles which were initially in a hexagonal symmetry are laterally pressurized to assume square symmetry and some of the particles are squeezed out to form bi-layers. The particles in the overlayer also should organize into square symmetry in a transition from $1\triangle \rightarrow 2\square$ [99]. However, with the present set of measurements there seems to be no direct evidence of the square symmetry of particles in the overlayer.

The experimental results and observations based on X-ray scattering and AFM measurements suggest that a monolayer of nanoparticles transferred from a liquid surface to a solid surface undergoes a continuous structural transition due to the drying of water trapped underneath the nanoparticles during the process of transfer of the monolayer from the trough. The drying accompanied with formation and growth of holes induces a lateral pressure on the monolayer and in all probability is

the driving force behind the structural changes from HCP to SL structure.

5.3 Gold Nanoparticles on Polymer surface

5.3.1 Experimental Details

Water soluble polymer Polyacrylamide of molecular weight 5×10^6 (Radius of gyration, $R_g \sim 80$ nm), supplied by Polysciences, Inc. USA, is used for preparing the thin polymer film. A solution of density 4 mg/ml is prepared by PAM in water. About 100 μL of the solution is then spun cast onto a polished silicon (100) substrate with spin speed of 2500 revolutions per minute (RPM). Before the deposition the substrate has been chemically treated with ammonia (NH_4OH) and hydrogen peroxide (H_2O_2) solution (NH_4OH:H_2O_2:H_2O = 1:1:2) to make the surface hydrophilic. A colloidal solution of 50 μL in toluene of chemically synthesized gold nanoparticles, having gold core of size ~ 2 nm encapsulated with dodecanethiol, of density 0.95 mg/ml is spun coated with spin speed 1000 RPM. X-ray specular reflectivity and Atomic Force Microscopy (AFM) measurements are done at different times, after the day of deposition, to observe the time evolution of the film and its surface respectively. The X-ray measurements were performed with 8.06 keV (1.54056 Å) Cu anode source of Nonius Enraf at Surface Physics Division of Saha Institute of Nuclear Physics.. Specular reflectivity data for the as deposited polymer film was first collected and data were taken for the film with deposited nanoparticles on the polymer film. Both AFM and X-ray reflectivity measurements were performed on 2nd, 4th, 5th, 8th, 10th and 19th day after deposition of the nanoparticles for the same film to see the time evolution of the morphology of the film. Multimode Nanoscope IV from Digital Instruments is used in tapping mode with a Silicon tip is used for the AFM measurements. The AFM images are taken just before the collection of each reflectivity data to see the modification of the top surface, if any.

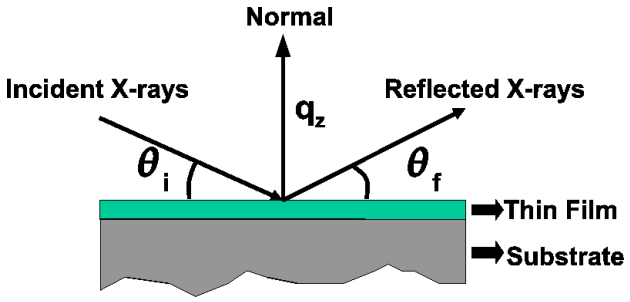

Figure 5.7: Schematics of X-ray reflectivity measurement.

5.3.2 Results and Discussions

The X-ray specular reflectivity ($\theta_i = \theta_f$) data collected from the bare polymer film and nanoparticle deposited polymer film as a function of vertical wave vector transfer $q_z = (4\pi/\lambda)\sin\theta_i$ as shown Figure 5.7. θ_i and θ_f being the angle of incidence and angle of reflection with respect to the surface and , the wavelength of X-rays. The x-ray reflectivity data provides us the information of variation of electron density along the depth of a film. In order to obtain the electron density profile along the depth of the films the inversion technique based on Born Approximation [158] is used as discussed in Chapter 3.

Applying the inversion technique we fitted all the reflectivity data obtained. Figure 5.8(a) shows the reflectivity data from the bare polyacrylamide film and nanoparticles covered polyacrylamide film collected after different time intervals starting from the day of deposition. The EDPs obtained by using the inversion technique are shown in Figure 5.8(b). In order to observe the changes in the EDP, all the EDPs are plotted by setting the substrate polymer interface as zero. The initial thickness of the polyacrylamide film and the nanoparticle layer just after deposition obtained from the fitting are 117 Å and 15 Å. The EDPs obtained from bare polymer film and the polymer film in the presence of nanoparticles on its surface show that the presence of nanoparticles modulated the electron density of the polymer film along its depth. The modulation is evident from the concave nature of the central part of the polymer layer in the presence of nanoparticles which was convex in the bare polymer film. Further the nanoparticle polymer composite system is allowed to relax for few days under observation, a gradual change in the EDP is observed. Figure 5.9(a) & (b) shows the change in the position of the electron density peak corresponding

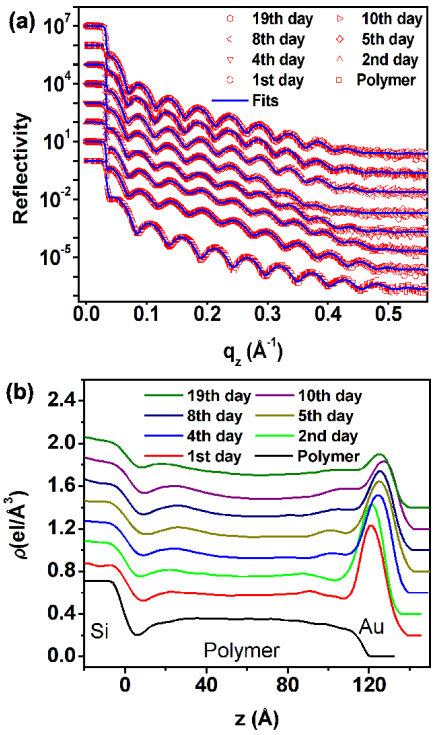

Figure 5.8: (a) Reflectivity curves (symbols) and the fits (solid lines) of the bare polymer film and the polymer film with gold nanoparticles on dispersed on its surface collected after regular interval of time. (b) The EDP obtained for the bare polymer film and the film with nanoparticles on its surface at different times. All the reflectivity data and the EDP are shifted for clarity.

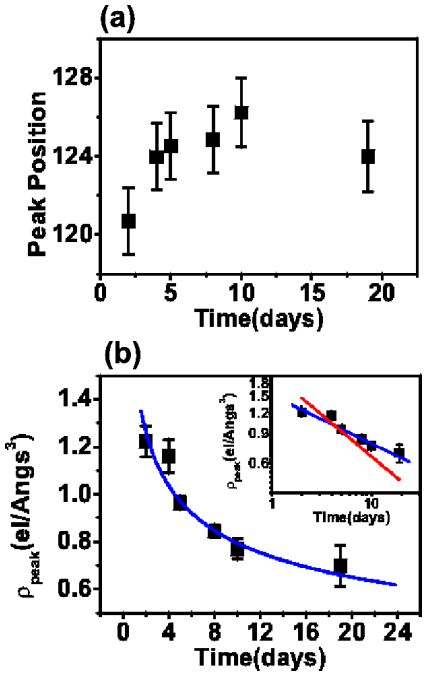

Figure 5.9: (a) The position of gold peak with error bars as a function of time in days. (b) The value of electron density of the top layer with error bar (symbols) as a function of time and the fitted power law curve (blue solid line) $t^{-\beta}$ with $\beta = 0.29$. The inset in (b) is the log-log plot of the same with both $\beta = 0.29$ (solid blue line) and $\beta = 0.5$ (solid red line).

to the gold layer and its value. There is a gradual shift of the nanoparticles in the positive direction (shown in Figure 5.9(a)) which is an indication of increase in overall thickness of the film by 5 Å . With the increase in film thickness a decrease in electron density of the peak corresponding to gold nanoparticles as a function of time is also observed. These two observations are the first indication of movement of gold nanoparticles inside polyacrylamide. During this sinking process another prominent layer of nanoparticles just below the polymer surface is formed at the depth of about 100 Å. Formation this kind of layer just beneath the polymer surface is reported earlier in a study of embedment of sub-micron sized Se or Sn particles inside a heated polymer [184]. The diffusion of nanoparticles in the out-of-plane direction from a monolayer film deposited on a polymer surface can be modeled as a one dimensional diffusion problem along the out-of-plane direction. The diffusive motion in the out-of-plane direction of the nanoparticles reduces the density of the monolayer with time. In order to know the nature of diffusion of these nanoparticles inside the polyacrylamide film we fitted the peak density as a function of time with

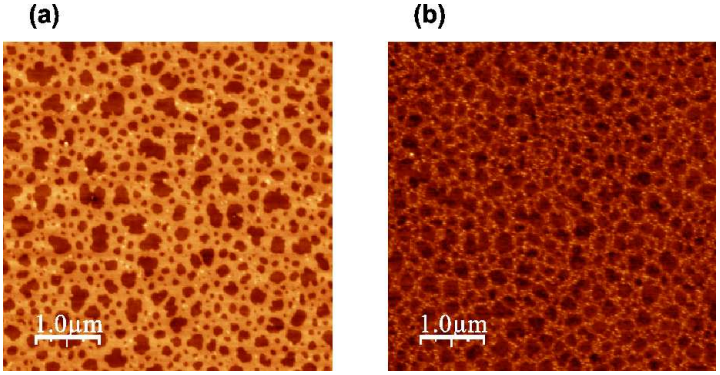

Figure 5.10: (a) The AFM image of nanoparticle dispersed polyacrylamide film just after deposition on a Silicon substrate. (b) The same film after 19 days of deposition. The scan sizes are 5 μm × 5 μm.

a power law $t^{-\beta}$. The value of for the best fitted curve (shown in Figure 5.9(b)) is 0.29 which is different from a Fickian dynamics. For the dynamics to be fickian the value of has to be 0.5 in one dimensions. We have also shown a curve with $\beta = 0.5$ in the inset of Figure 5.9(b) which is not at fitting. The value of alpha show the diffusion to be non-fickian and very slow dynamics.

We also found considerable changes in the in-plane structure of the nanoparticles. Figure 5 shows the AFM images of nanoparticle-covered polymer film taken just after deposition and after 19 days. Initially a well defined connected network structure of monolayer of nanoparticles is formed. Finally due to the combined effect of in-plane and out-of-plane movements, some of the nanoparticles, which are close to each other, aggregate and remaining sink inside the polymer film. The aggregates of nanoparticles are of sizes of about 60 nm. The formation of these aggregates is due to the increase in effective inter-particle attraction in the presence of polymer film [103]. The change in the in-plane structure is further confirmed by the calculation of height-distribution from the AFM images. The height-distributions are shown in Figure 5.10. In Figure 5.10(a) the height distribution of the film, just after deposition, is shown. The distribution is found to be a bimodal distribution. The individual peaks signify two interfaces. The peak at lower z values corresponds to the polymer-nanoparticle and that at higher value is for nanoparticle-air interface. This bimodal distribution shows that the nanoparticles have formed a uniform film on the polymer surface. The height distribution for the latter case did not show such kind of bimodal

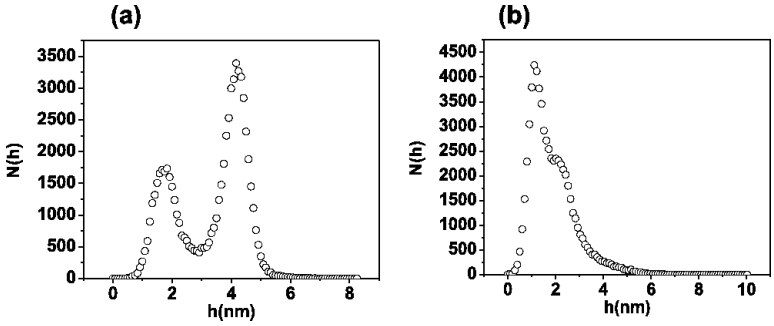

Figure 5.11: (a) The height distribution calculated from form the AFM images shown in Figure 5.10(a). (b) Height-distribution for the image shown in Figure 5.10(b).

distribution. There is a peak at a lower z value which now corresponds to the polymer surface embedded by nanoparticles. There is a long tail of this peak for the higher z-values which shows the reduction of number density of nanoparticles on the polymer surface. This observation supports our result from x-ray reflectivity data that some nanoparticles are gradually embedding inside the polymer along with the formation of aggregates of nanoparticles which are still remaining on the surface. The formation of these aggregates due to the dominant inter-particle interaction prevents the nanoparticles to embed inside the polymer film.

5.4 Conclusions

In conclusion, in this Chapter I have presented our studies on dynamics of ordering of thiol encapsulated gold nanoparticles on a Silicon substrate just after transfer from air-water interface and on a surface of thin film of Polyacrylamide. A time-resolved x-ray scattering and AFM measurements are performed to probe the dynamics of structural phase transition from hexagonal to square symmetry in the transferred monolayers of gold nanoparticles. We observe that the particle-particle correlation peak obtained from GID measurements shifts towards lower $q_{||}$ value indicating that the distance between nearest neighbours increases with time. AFM measurements however reveal compactification of the monolayer as well as increase in the average height of the monolayer. As drying of the colloidal particles progresses pinholes are created in the large islands which nucleate and grow, dragging along the

nanoparticles at their peripheral fronts until meeting of similar adjacent holes. The lateral pressure exerted by the growing voids due to inhomogeneous drying cause the monolayer to buckle and form bi-layer and in the process brings about a continuous structural transformation of the nanoparticles from hexagonal to square symmetry.

The embedment of gold nanoparticles having hydrophobic ligand shell inside a hydrophilic polymer film of polyacrylamide is shown. The AFM and X-ray reflectivity measurements show the dynamics of both in-plane and out-of plane morphology of the film with time. The out-of- plane diffusion of nanoparticles is shown to be non-fickian and slow with $\beta = 0.5$ in comparison to the fickian dynamics with $\beta = 0.29$. The in-plane movement of nanoparticles at the top surface leads to cluster formation, starting with a network structure. Both the in-plane and out-of-plane change in morphology are the resultant of complex interacting forces developed due to polymer itself and the density in-homogeneity across the interface. The understanding of these complex forces definitely increases the understanding various natural phenomena and helps us to synthesize materials with novel properties.

Chapter 6

Gold Nanoparticles at Toluene-Water Interface

6.1 Introduction

Exhibition of unique electrical [19,21,22,20,6] magnetic [45,43,44] optical [22,25,175] and catalytic [185, 51] properties by gold nanoparticles makes them important for both basic and applied research. Due to these unique physical properties, the controlled synthesis, growth and structural properties of these nanoparticles motivated both physicists and chemists for the last three decades. Many methods have been developed [5,13,14,2,126,64,65,111] so far to prepare these gold nanoparticles. Out of these, the method utilized by Rao et al [65, 66] to produce gold nanoparticles involves interfacial reduction reaction at toluene-water interface, is unique and is not well understood till date. Though they standardized this method to produce not only gold nanoparticles but also nanoparticles of other metals, metal-oxides and metal-chalcogenides [64] but the formation, ordering and structure of nanoparticles formed at the interface are still a subject of research. The measurements such as Transmission Electron Microscopy (TEM), Atomic Force Microscopy (AFM) and absorption spectroscopy have been performed for characterizing the nanoparticles formed at the toluene-water interface but they are done only after transferring the interfacial film to either a solid substrate or a carbon grid or any other solvents. All these measurements provide us with the structural information of the nanoparticles

not during formation but after the transfer. Moreover, it has been found that [186] the coalescence of neighboring nanoparticles due to heating by electron beam in a TEM measurement could provide overestimated size of the nanoparticles. So in order to have information of growth and structure of nanoparticles formed at the interface one needs to perform in-situ measurements during formation at the toluene-water interface. The in-situ measurements will not only provide us with information of growth and structural properties of the film of nanoparticles formed at the interface but also the interfacial reaction mechanism which is of fundamental importance in several important research areas including drug delivery, diffusion through biological membranes.

Liquid-liquid interfaces provide an inhomogeneous environment between the two liquids and can alter the behavior of the reacting molecules [110, 187, 116, 188]. Formation of the nanoparticles at the interface is due to the reduction of metal ions dissolved in the toluene layer by a suitable reducing agent in the aqueous layer. This reduction at the interface is facilitated by transfer of ions across the interface and that depends on the interfacial structure. In other words, the nature of interfacial structure dictates the nature of interfacial reaction and consequently the formation and ordering of nanoparticles at the interface. One of the remarkable properties of the liquid interfaces which is very well studied so far is the long range correlations termed as 'Capillary wave fluctuations' [119, 112, 189, 120, 115] which are induced by inhomogeneity across the interface. Though there are no experimental evidences yet but computational studies [116] on the transfer of ions from one liquid to the other through there interfaces suggested the formation of finger-like protrusions into each other to facilitate the transfer. These protrusions are expected to be as large as 1 nm and last for tens of picoseconds. An in situ study of nanoparticle formation and ordering should provide us with a unique opportunity to probe the inhomogeneous chemical reactivity and associated ion/charge transfer processes across interfaces.

This chapter is devoted to our in-situ study of formation, ordering and structural properties of gold nanoparticles formed at toluene water interface by high energy GIXS techniques. Though the simulation results show that the ion/charge transfer mechanism is facilitated by microscopic fluctuations in the form of finger like

protrusions, the macroscopic fluctuations introduced by external mechanical vibrations during formation can alter the organization of the nanoparticles. The primary motivation of this study is to measure the size of the gold nanoparticles generated through the interfacial reduction reaction and to determine the nature of the ordering of these nanoparticles at the interface both in the absence and presence of external mechanical vibrations. The other aim of this work is to study the toluene-water interfacial tension as the nanoparticles form at the interface by measuring the GID [118] as a function of the in-plane wave vector transfer ($q_{||}$). Although liquid surfaces have been studied by diffuse scattering measurements of capillary wave fluctuations [112, 189, 115], it is only recently that the buried liquid interfaces are receiving attention [119, 120, 123, 124, 114]. Since X-ray scattering techniques sensitive to interfaces are carried out with a vibration isolation table and effect of external vibrations is not possible. Ex-situ Atomic Force Microscopy (AFM), and Scanning Electron Microscopy Measurements are performed on transferred films of gold nanoparticles from the toluene-water interface to monitor the effects of external mechanical vibrations on the film. A simple light scattering measurement in reflection geometry from the bare toluene-water interface is also done to monitor the nature of fluctuations both in the presence and absence of external mechanical vibrations. In order to obtain the in-situ growth and ordering of gold nanoparticles formed at the toluene-water interface in the presence of external vibrations, GISAXS measurements are performed.

We performed three independent measurements to study the growth, ordering and structural properties of gold nanoparticles formed at toluene-water interface by an interfacial reactions both in the absence and presence of external mechanical vibrations. In the first section of this Chapter, the in-situ GIXS measurements namely specular X-ray reflectivity (XRR), Grazing Incidence Diffraction (GID) are presented to study the ordering of gold nanoparticles formed at the toluene-water interface in the absence of external mechanical vibrations. We performed AFM measurements and SEM measurements on the transferred films from the interface to a Silicon substrate to study the effect of external mechanical vibrations on the growth and formation of nanoparticles. These measurements are presented in the

second section of this Chapter. Third section is devoted to the in-situ GISAXS measurements on the gold nanoparticle formation at the toluene-water interface by the same reaction in the presence of external mechanical vibrations to study the primary size of the nanoparticles and the nature ordering at the interface. In the concluding section, we will provide a brief picture of the gold nanoparticles formed at the interface by combining all the results of our experiments.

6.2 In-situ GIXS Measurements

6.2.1 Experimental details

In order to do the GIXS experiments to study the interfacial reactions we prepared freshly prepared solutions of the gold precursor, $Au(PPh_3)Cl$ (triphenylphosphine gold chloride), in toluene, an aqueous solution of NaOH (sodium hydroxide) and THPC (tetrakis-hydroxymethyl phosphonium chloride) of concentrations 0.25 mM (milli Molar), 0.625 mM and 50 mM respectively. THPC is the reducing agent used for this reaction. For carrying out X-ray scattering experiments from liquid-liquid interfaces one has to face two main problems. Firstly, to make the interface flat and secondly, to take care of absorption of X-rays while passing through the upper liquid. In order to overcome these two problems we prepared a special trough as discussed in Chapter 2 and used monochromatic X-ray beam of energy 21.9 keV corresponding to wavelength of 0.057 nm of ID10B beamline of ESRF, France. The energy of the monochromatic beam was set to 21.9 keV to allow the X-ray beam to pass through the upper liquid (toluene here) and reflectivity and diffuse scattering data were collected from the toluene-water interface. In this set up the X-ray intensity reduces by a factor of 0.142 and 0.0195 as the 21.9 keV beam pass through 7 cm of toluene and water, respectively. We also collected scattering data in the same geometry from the toluene bulk by moving down the interface 0.2 mm to subtract background arising from bulk scattering. We neglected the contribution of bulk water scattering in the analysis as incident angle of beam was low and absorption coefficient of water is much higher than toluene. The scattering intensity profile measured as functions of out-of-plane and in-plane components of the wave-vector

transfers q_z and q_y, being related to the out-of-plane and in-plane angles θ_f and ϕ given by Equation 3.6, provide information regarding the out-of-plane and in-plane ordering of nanoparticles formed at the liquid-liquid interface. The position of the interface was adjusted to minimize the meniscus by controlled addition and removal of water and monitoring sharpness of reflected beam at small θ_i. Reflectivity data of the toluene-water interface were collected using a point detector by changing the incident and reflected angles and keeping these two angles equal ($\theta_i = \theta_f$). For diffuse scattering measurements, position sensitive detector (PSD) was used to collect the data as a function of the in-plane angle (ϕ), keeping the incident grazing angle (θ_i) fixed at 80 millidegrees. . The process was repeated several times to confirm reproducibility of the scattering data. All the measurements were performed at room temperature (23 ℃) with the incident beam size of 0.017 mm×1.0 mm (V×H) defined using conventional slits. Details of the experimental arrangement are available in the literature [189, 120, 123].

6.2.2 X-ray Reflectivity (XRR) data

In Figure 6.1(a), we have shown six reflectivity curves collected after the initiation of the reaction and indicated the time of data collection. We have also presented in the insets of Figure 6.1(a) and (b), the reflectivity data and electron density profile of the bare toluene-water interface, respectively. We required around 30 minutes time to collect a reflectivity profile and have not presented the data collected within 194 min of initiation of reaction here because the profiles changed during the scans. The oscillations in the measured reflectivity curves indicate the presence of a thin film at the toluene-water interface.

These curves were fitted using the Iterative inversion technique (Equation 3.37) based on the Born approximation as discussed in Chapter 3. We used the water-toluene profile (with a small increase in toluene density due to presence of $Au(PPh_3)Cl$ to match the critical angle) shown in inset of Figure 6.1(b) as initial $\rho_m(z)$ and confirmed the stability of the solutions by setting various total film thicknesses. The extracted final electron density profiles, for these six reflectivity data, which always take the value of water density toward the end of the film, are shown in Figure

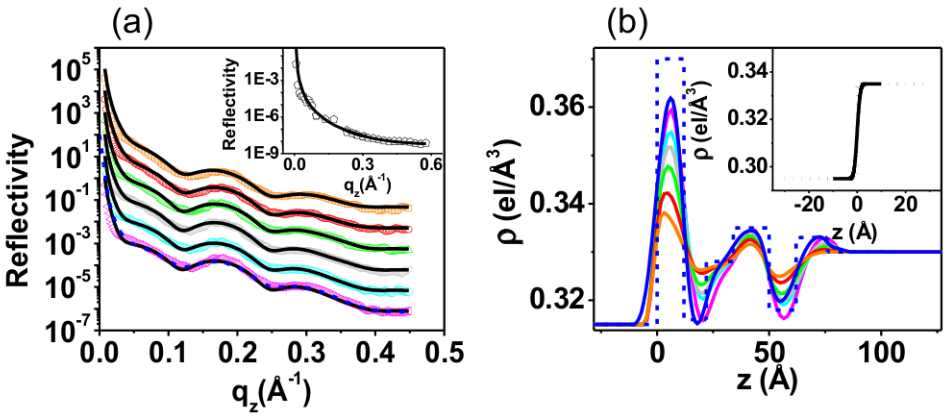

1

Figure 6.1: (a) Variation of reflectivity and fits as function of q_z after initiation of the reaction (pink, 194 min; light blue, 224 min; Grey, 253 min; green, 283 min; red, 312 min; orange, 364 min) and the fits (solid lines). The reflectivity (dashed line) generated from the simple box model is also shown. Inset: The reflectivity data (<) from the toluene-water interface and its fit (solid line). (b) The electron density profiles (EDPs) (colors same as those in a) as function of depth obtained from fitting. Positions of the two upper peaks as measured from the water interface (dashed line) 70 Å and 40 Å are marked. A simple model without (dashed line) and with roughness convolution (solid line, blue) are also shown.

6.1(b).

We also verified the solutions by simple models having a few slices; one such simple model having six slices for 194 minutes data is also shown with and without roughness convolution along with the corresponding calculated reflectivity data in Figure 6.1(a). The dip in the reflectivity data around 0.123 Å^{-1} and the subsequent modulation require a strong peak in the electron density around 70 Å above the water surface. The width of this peak and the simple model shown in Figure 6.1(b) suggest the size of the uppermost gold particle to be around 12 Å. There is a broad composite structure around the middle of the film (marked as 40 Å) and a small hump just before reaching the water density. Interestingly, these three layers have a vertical separation of about 30 Å from each other. The electron density between these layers takes the value (0.32 electrons/Å^3) of a typical organic material. The electron density of the uppermost layers reduces, and the peak electron densities of all of the peaks tend to become equal as time progresses, but the separation of the layers remains nearly constant.

The profiles obtained in Figure 6.1(b) with continuous reduction of electron

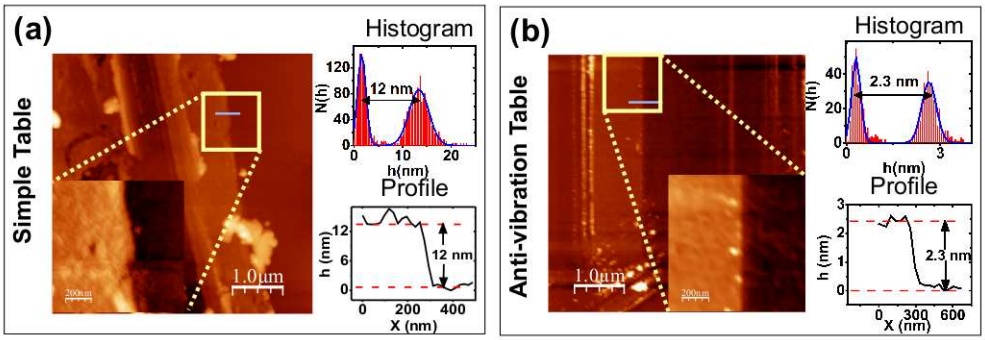

Figure 6.2: AFM images of the films formed on the toluene-water interface inside a beaker placed on (a) a simple table and (b) an anti-vibration table and deposited on a silicon substrate are shown. The enlarged views of the regions marked by yellow squares are shown as insets. The height distributions obtained from the enlarged views and height profiles corresponding to the marked blue regions of the films are shown beside the respective images.

density of the uppermost layer can be explained assuming coexistence of a monolayer of individual nanoparticles having around a 12 Å gold core with an 11 Å organic shell and a layer of a 13-member "magic cluster" of these nanoparticles. With the progress of reaction, the number of individual nanoparticles reduces and only the monolayer of the "magic cluster" remains at the toluene-water interface. To verify the presence of the monolayer of individual nanoparticles, we measured the thickness of the film after transferring it on to a silicon substrate using an AFM as discussed in Chapter 2. We transferred the films after carrying out the reaction for 15 min on both ordinary and anti-vibration tables (see Figure 2a and b). Although much thicker films (120 Å) were formed on an ordinary table, the film thickness obtained on an anti-vibration table was around 23 Å. A monolayer film of individual nanoparticles would have given a film thickness of 34 Å. We feel that the reduced thickness observed here is due to the partial removal of the organic layer during transfer from the toluene-water interface. The thickness of a film on the anti-vibration table grows slowly with time, and the rate of growth depends on the in-plane pressure. A detailed analysis of AFM results of the films transferred at various time intervals is presented in the next section.

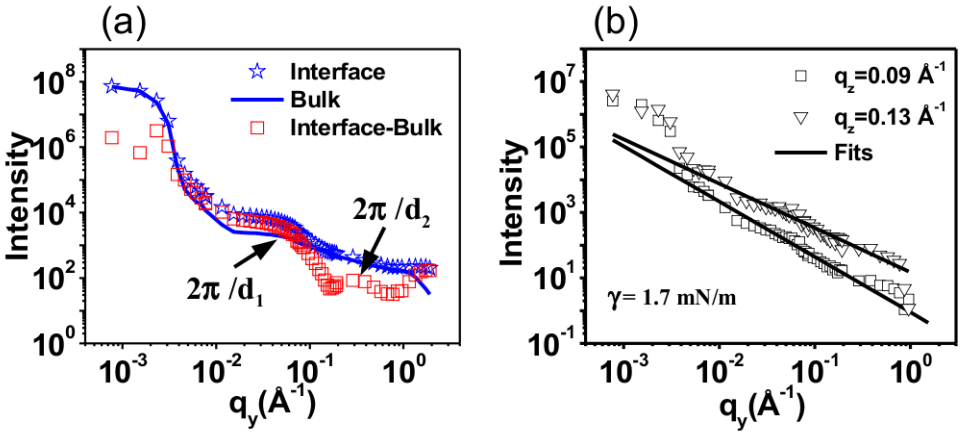

Figure 6.3: (a) Grazing incidence diffraction (GID) data integrated over q_z are shown as a function of q_y from the interface (☆), bulk (solid line) and interface - bulk (□). The GID peaks are also marked by $2\pi/d_1$ and $2\pi/d_2$. (b) The variation of scattered intensity from interface (symbols) at two different q_z values and the corresponding calculated intensity from capillary wave theory with a fixed interfacial tension.

6.2.3 Grazing Incidence Diffraction data

In Figure 6.3 (a), we have shown the measured Grazing Incidence Diffraction (GID) profiles from the interface and the bulk (obtained by lowering the interface by 0.2 mm) as a function of q_y by integrating the PSD data over q_z. The bulk scattering data was subtracted from the interfacial data (shown as "Interface-Bulk" in Figure 6.3(a), and a small peak around 0.29 Å^{-1} is observed. This peak corresponds to the separation (d_2) between two individual nanoparticles and is much weaker than the peak observed at 0.04 Å^{-1} that corresponds to the separation (d_1) of clusters discussed below. Because the measurement of diffuse scattering data takes a long time after initiation of reaction, the number of individual nanoparticles reduced and the clusters dominated the toluene-water interface. We could not detect any rod or arc scattering in the $(q_y - q_z)$ plane that represent (as discussed in Chapter 6) two-dimensional and three-dimensional aggregates of these particles and clusters due to strong bulk scattering.

The diffuse scattering data was analyzed using the capillary wave model of liquid interfaces for determining the effective interfacial tension of the toluene-water interface. The large diffuse scattering intensity in the low q_y region as well as the decay of the intensity as $q_y^{\eta-2}$ (where the η is equal to $k_B T q_z^2/(2\pi\gamma)$ and γ is the interfacial

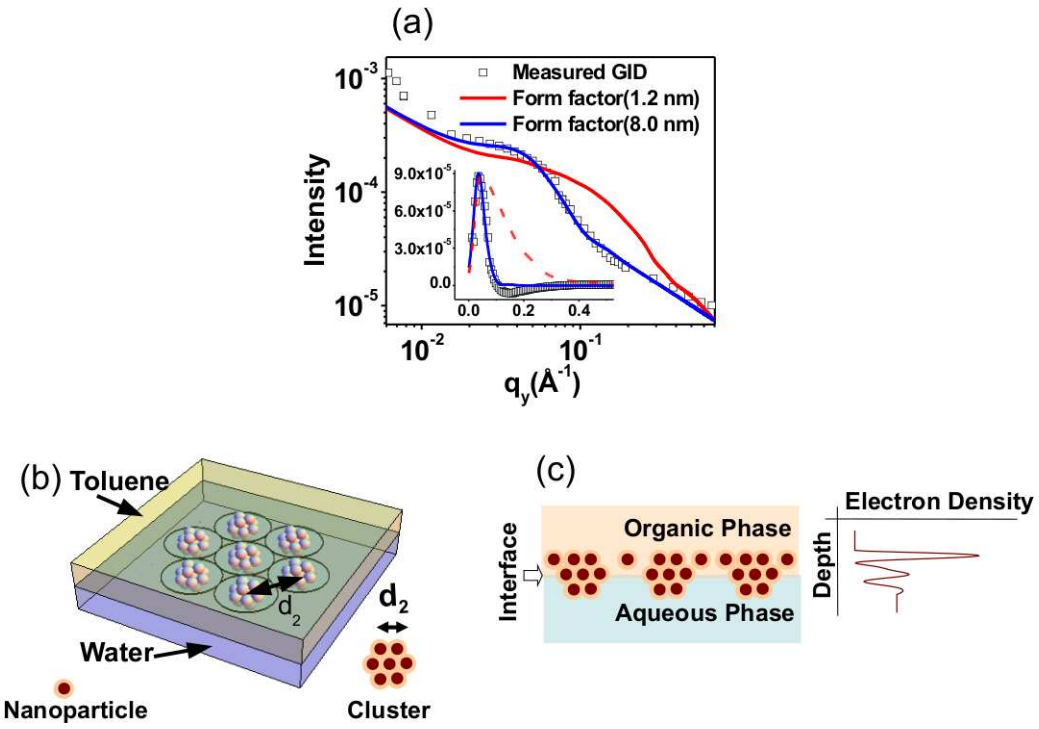

Figure 6.4: (a) GID data (□) normalized to unity and the fits obtained from our model with core sizes 80 Å (solid line) and 12 Å (dashed line). Inset: The GID peak and the fits are shown in linear scale after subtracting the capillary scattering contribution. (b) Three-dimensional schematics of our model that involve a 13-member cluster of organic capped gold nanoparticles at the toluene-water interface are shown along with the two-dimensional schematics of an individual nanoparticle and a cluster. (c) Two-dimensional schematics for the same model is also shown along with the three-layered electron density profile as a function of depth obtained from the fitting of specular reflectivity data.

tension) from a liquid surface can be explained using a logarithmic height-height correlation induced by capillary fluctuations without any fitting parameters as discussed in Chapter 3. In Figure 6.3(b), we have shown diffuse scattering data around q_z values of 0.09 and 0.13 Å^{-1} after subtracting the corresponding bulk scattering data. This data could be fitted with the two straight lines shown in the log-log plots. The slopes $(\eta - 2)$ gave [112] the value of the interfacial tension as 1.7 mN/m; this value is much lower than the expected value (27.8 mN/m) of the toluene-water interface. The small value of the interfacial tension indicates the enhancement of interfacial roughness probably due to the presence of the organic layer discussed below at the interface.

In Figure 6.4c, we have shown measured data near the grazing incidence diffrac-

tion (GID) peak and a fit to a calculated profile that includes scattering from a two-dimensional radial distribution function of gold nanoclusters and capillary scattering contributions; details of this formalism is already discussed in the previous Chapter. The position of this peak indicates an in-plane separation of 180 Å, but the calculated profile with a form factor of a 12 Å (the smallest size of nanoparticle obtained from XRR analysis) spherical nanoparticle is found to be broad and could not represent the measured data (dashed lines Figure 6.4(a)). A spherical cluster size of about 80 Å was required to fit the GID peak. The solid line shows the best fit that includes Gaussian broadening of 0.015 $Å^{-1}$ that represents coherent scattering surface area of islands of these clusters. In the lower inset, the GID peak and the fits are shown in linear scale after subtracting the capillary scattering contribution. It is to be noted that capillary scattering contribution is a sloping line in log-log scale.

We present a simple model in Figure 6.4(b) that can explain the electron density profile extracted from the reflectivity data and in-plane scattering around the GID peak. This model assumes a "magic cluster" of 13 Au nanoparticles of 12 Å diameter, one at the center and twelve surrounding it in a compact spherical shell, each having an organic capping of 11 Å. The central cross-section of this cluster is shown in the lower-right corner of Figure 6.4(b) with a particle-particle separation (d_2) 34 Å. For the GID fit, we approximated these clusters with a core-shell model having an 80 Å central core and an organic capping of 11 Å. If we assume that the location of the water-toluene interface is around the middle of the cluster, then the lower portion of the hydrophobic organic capping cannot stay in water and floats around the upper half of the spherical cluster to form a ring in toluene just above the interface, making the capping look like a "semi-spherical cap" on the metal cluster. The extension of the resultant capping is shown as black circles in Figure 6.4(b). Simple volume calculations indicate that a 5-Å-thick ring generates an average diameter of these circles or cluster-cluster separation d1) 180 Å, as observed in GID data. Earlier results [186, 65, 64] of similar nanoparticles formed at room temperature showed rather mono-dispersed larger particles (70 to 80 Å diameter) in TEM, but X-ray diffraction data from these transferred films did not show peaks expected from such

large particles These observations are also consistent with our present model because the 12 Å nanoparticles in the cluster cannot give distinct X-ray diffraction peaks but 13 of them can inter-diffuse within the cluster to form bigger particles due to electron irradiation in TEM [186].

In conclusion, we have shown by an GIXS study that a monolayer of clusters having 13 gold nanoparticles of 12 Å diameter with large (180 Å) in-plane cluster-cluster separation forms at the toluene-water interface. The electron density of such aligned clusters is expected to exhibit three layers along the depth with the central electron density values of 0.33, 0.37 and 0.33 electrons/Å^3. Reflectivity measurements confirm the presence of three layers with the lower two layers showing slightly less than the calculated values probably due to partial coverage. The presence of low electron densities in between these peak values confirms the monodispersity of these aligned clusters. The higher electron density of the top peak indicates the presence of individual gold nanoparticles with these clusters (refer to Figure 6.4(c)). The presence of individual nanoparticles in the initial phase of the reaction is evident from AFM measurements of early films. As the reaction progresses, the number of individual Au nanoparticles reduces and only magic clusters at the toluene-water interface remain. The presence of an organic layer (shown as black circles in Figure 6.4(b)) at the water-toluene interface lowers the interfacial tension as seen in diffuse scattering measurements. It seems that the presence of the clusters and the associated organic layer hinders the progress of the reaction unless the interface is disturbed by surface pressure and/or vibrations.

6.3 Effect of External Vibrations on the formation of nanoparticles

The model for the formation of films of gold nanoparticles proposed on the basis GIXS study assumes that 13-member magic-clusters of 1.2 nm gold nanoparticles are first generated at the interface. Although this model could explain out-of-plane and in-plane X-ray scattering data, direct evidence of the presence of 1.2 nm nanoparticle could not be obtained from this study. In this section we will show that 1.2 nm gold

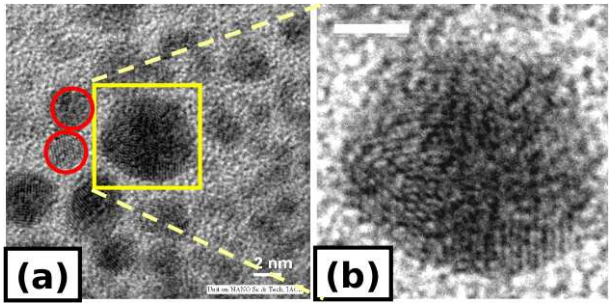

Figure 6.5: (a) TEM micrograph of nanoparticles. The nanoparticles with 2 nm gold core are shown by enclosing them under red circles. (b) High-resolution TEM micrograph of the 5 nm nanoparticle showing multiple grains. The scale shown in both the images corresponds to 2 nm.

particles are indeed formed in the reduction reaction on the basis of a high-resolution atomic force microscopy (AFM) study carried out in ultra-high vacuum (UHV) on films transferred on the silicon substrates from toluene–water interface. We will show that one can obtain a monolayer film of the 1.2 nm gold nanoparticles capped with 1 nm organic layer provided the reaction is carried out on a anti-vibration table that reduces macroscopic inter-diffusion and the film is transferred within few minutes. Thicker films are obtained if an anti-vibration table is not used to stabilize the interface as reported earlier [66].

6.3.1 Experimental Details

The reaction was carried out in two identical 25 ml beakers by keeping one on a vibration isolation table and the other on a regular laboratory table. In both the cases, 2 ml of 1.5 mM solution of triphenylphosphine gold chloride ($Au(PPh_3)Cl$) in toluene was allowed to stand in contact with 3.2 ml of 6.25 mM aqueous NaOH solution at room temperature. After the stabilization of the interface between the two liquids, 60 μL of 50 mM tetrakis-hydroxymethylphosphonium chloride (THPC) was injected into the aqueous layer with minimal disturbance to the toluene layer. The initiation of the reaction was assumed to be the instant at which the reducing agent THPC is injected into the toluene layer.

The time of termination of the reaction is the instant at which the toluene layer is removed from the beaker with the help of a syringe again with minimal

disturbance of the interface. Figure 6.5(b) shows a typical transmission electron micrograph (TEM) recorded with a 300 keV JEOL microscope by taking out the nanoparticles on a copper grid after 24 h of reaction. The micro-graphs primarily showed the presence of nanoparticles of about 5 nm diameter, as reported earlier [66] but, traces of 2 nm particles were also observed as marked by the red circles in Figure 6.5(b). A high-resolution image of a 5 nm particle in Figure 6.5(b) shows multiple grains which may be formed due to agglomeration of smaller nanoparticles due to the exposure of electron beam in TEM [186]. For this reason, we have used the UHV-AFM technique here to study the formation of small nanoparticles. However we find that the transfer of nanoparticles from the liquid–liquid interface on to a solid substrate disturbs the ordering as seen in the in-situ GIXS study and results in the formation of aggregates of nanoparticles. Although we could measure the film thickness over short distances, X-ray reflectivity study could not be carried out due to roughening of the film due to formation of aggregates. The aggregates also hindered extensive UHV-AFM measurements and better transfer methodology seems necessary.

We have investigated the formation of the nanoparticles at the initial stages of reaction with and without the vibration isolation table. Results of three such reactions in each of the sets carried out in six different beakers are presented here. The reaction was terminated by taking out top toluene slowly after three different durations of time - 15 minutes, 1 hour and 2 hours. After the termination of the reaction, the nanoparticle films formed at the interface were transferred on to silicon substrates (1 cm $\times$ 1 cm), which were cleaned earlier by sonicating with acetone and propanol. We first carried out ambient AFM measurements of the films using a silicon tip with tapping mode of Nanoscope IV. In order to get proper information about the thicknesses of the films, edges of the films were made by wiping out a part of the film using a sharp blade. AFM topography of each of the films was taken at three different places near the edges to check the consistency of the film thicknesses obtained. The analysis of the AFM images to obtain information about the film thickness and roughness was done using WSxM software [183]. High-resolution UHV-AFM measurements were carried out using a Omicron SPM operating at 3×10^{-10} mbar

pressure in non-contact mode with a silicon tip. The UHV-AFM results on clusters and individual nanoparticles formed in the films obtained after 15 min of reaction with and without anti-vibration table are presented here. We also performed X-ray fluorescence analysis of gold and phosphorous present in the organic layer using EDAX energy dispersive X-ray spectrometer (EDS) attached with FEI QUANTA 200F scanning electron microscope (FEG SEM) with the electron acceleration set at 10 kV.

6.3.2 Laser Reflection Experiment on Toluene-Water interface

In order to characterize the amplitude of vibrations of the toluene– water interface, a laser beam from He–Ne laser (wavelength = 632.8 nm, Power = 4.5 mW) was allowed to incident on the toluene–water interface. The fluctuations of reflected beam due to interfacial vibrations were detected by measuring the voltage fluctuations of a photo-diode placed after a 2 mm slit as shown in Figure 6.6. The voltage fluctuations were measured using a 100 MHz Digital Oscilloscope.

The fluctuations in the voltage of the photo-diode due the fluctuation of the reflected beam are shown in Figure 6.6(b). It is evident from Figure 6.6(b) that the amplitude of voltage fluctuations obtained from simple table is larger than that of anti-vibration table. The width of the distribution of the voltage fluctuations for simple table was obtained as $w_1 = 7.4$ mV while in case of anti-vibration table w_2 is 2.3 mV. This and corresponding reduction of amplitude in the specular direction, is the direct evidence of larger interfacial fluctuations at toluene–water interface on simple table compared to anti-vibration one. The power spectrum obtained through Fourier transform of the voltage fluctuations for the simple table as well as for the anti-vibration table are shown in Figure 6.6(c). The fluctuation in air-cushioned anti-vibration table is reduced substantially especially around 10 Hz frequencies. It should be mentioned here that coupling of vibration of the table with liquid–liquid interface is nontrivial and depends on liquid thicknesses and surface area – it will be interesting to study this interfacial reaction by driving the table with various frequencies.

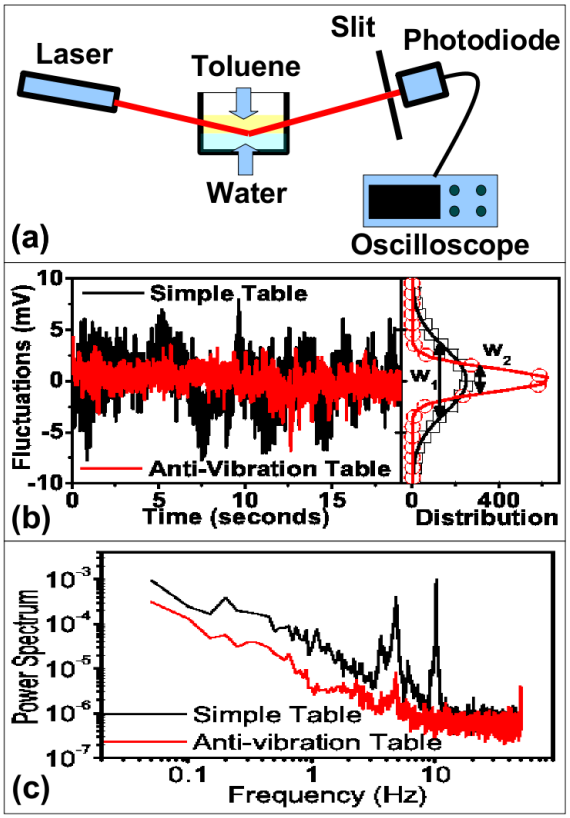

Figure 6.6: (a) The schematics of the optical set-up used to measure the interfacial vibrations of toluene–water interface. (b) The voltage fluctuations as a function of time detected in the photo-diode due to the fluctuation of reflected laser beam from toluene–water interface. The black solid line corresponds to the fluctuations when the beaker containing toluene–water interface was kept on a simple table and red solid line is when kept on anti-vibration table. The distribution of the fluctuations (symbols, red (simple table), black (anti-vibration table)) are shown just adjacent to it along with Gaussian fits (solid lines) with the corresponding FWHMs w_1 and w_2. (c) The power spectrum of the voltage fluctuations averaged over 15 measurements obtained from toluene–water interface on simple table and anti-vibration table.

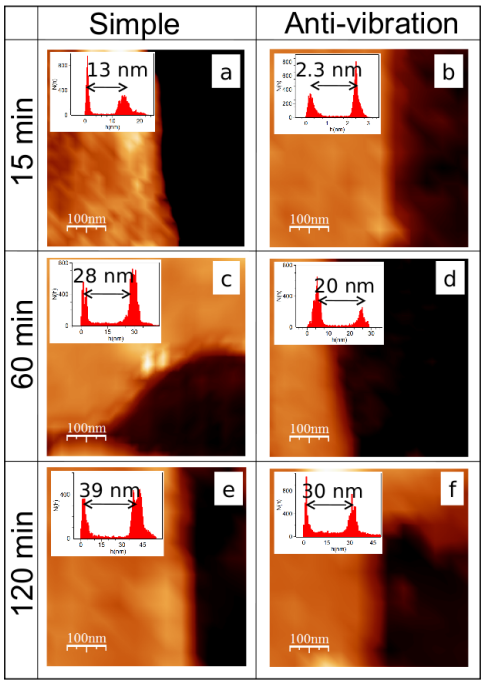

Figure 6.7: AFM images of films of gold nanoparticles formed on simple table and anti-vibration table after 15 min (a) and (b), after 60 min (c) and (d) and after 120 min (e) and (f), respectively. The dark and bright regions in the images correspond to substrate and nanoparticle film. The height distributions are shown in each of the insets showing two peaks corresponding to the substrate surface and the film surface. The distances between the peaks determine the average thickness of the films.

6.3.3 AFM measurements

The topography of the films transferred after the completion of 15, 60 and 120 min of reaction on the regular laboratory table are shown in Figure 6.7(a), (c) and (e), respectively and corresponding images for the films obtained on vibration isolation table are shown in Figure 6.7(b), (d) and (f), respectively. The thickness of each film was determined from the height distributions as shown in insets of Fig. 3. The films of nanoparticles obtained on the vibration isolation table is 2.3 nm in thickness (Figure 6.7(b)) which is about 10 nm thinner than the film obtained on simple table (Figure 6.7(a)) after 15 min of reaction time. After 1 h (shown in Figure 6.7(c) and (d)) and 2 h (shown in Figure 6.7(e) and (f)) of the reaction, there is increase in the thickness on both the normal and anti-vibration tables, but difference in thickness of about 8–10 nm is observed. High-resolution UHV-AFM images of the films after 15 min of reaction on the anti-vibration and normal tables are shown in Figure

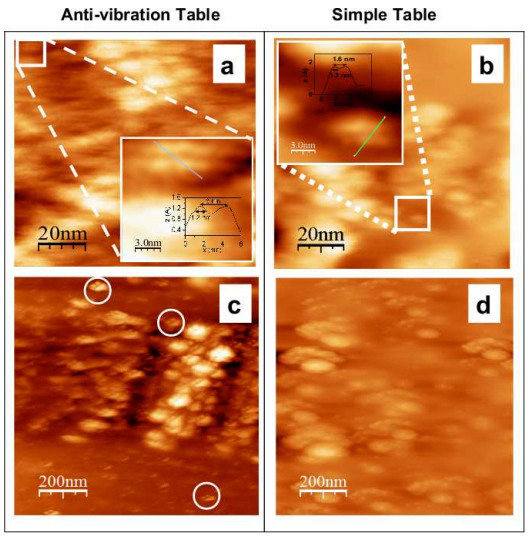

Figure 6.8: High-resolution UHV AFM images of nanoparticles obtained after 15 min of reaction on anti-vibration table (a) and (c) and on simple table (b) and (d). The regions marked under white squares in (a) and (b) are magnified to show the individual nanoparticles. The insets inside the magnified images are the height profiles to show the particle sizes and separation. Existence of 8 nm cluster is marked in (c) but aggregates shown in (d) have wide distribution.

6.8. It is apparent that height fluctuations are small in both the images due to the presence of organic capping. In the image of the sample prepared on the normal table the average in-plane size of the aggregates was much higher and has wide size distribution (Figure 6.8(d)). But sample transferred on anti-vibration table clearly showed presence of primarily 8 nm particles (refer Figure 6.8(c)). The clusters of this size having 13-member 1.2 nm gold nanoparticles with 1.1 nm organic shell were predicted from GIXS study (refer 6.4(b) and (c)). The images shown in the corresponding insets are magnified versions of the regions marked by white squares. Both the insets show the presence of individual nanoparticles of sizes about 1.2 nm and separation of these nanoparticles are also found to be around 3 nm. Both these numbers are consistent with the model shown in 6.4(b) and (c), which was proposed on the basis of GIXS measurements. The EDS data in Figure 6.9(a) and (b) for the films prepared without and with the anti-vibration table, respectively show the presence of Au-M_α and P-K_α, expected from the organic-coating of gold nanoparticles. All the EDS data are normalized with respect to the Si-K_α peak to see the relative strength of the Au and P peaks. Under both the reaction conditions

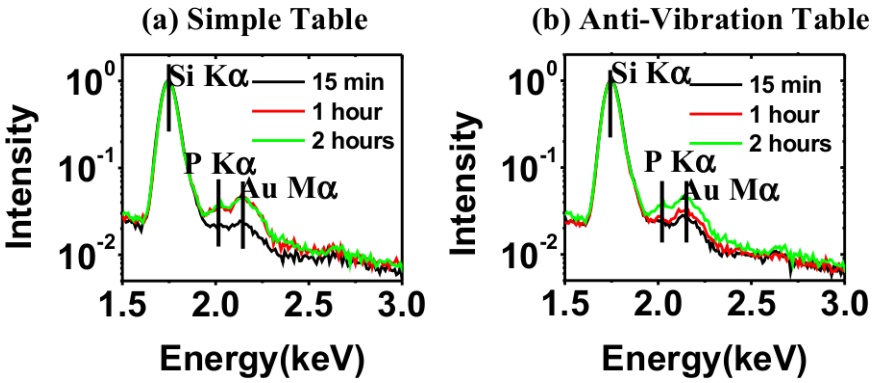

Figure 6.9: EDS data as a function of energy normalized with respect to the Si-K_α peak are shown for films formed on (a) simple table and on (b) anti-vibration table with different reaction times.

the strength of the Au-M_α peak increases with reaction time but relative strength with respect to P-K_α peak remains almost constant. This indicates the formation of nanoparticle aggregates having constant gold-to-organic ratio in both types of films.

In conclusion, results of UHV-AFM measurements on gold nanoparticle aggregates transferred on the silicon substrates after formation at the toluene–water interface have provided new insights. In the case of films produced on the anti-vibration table, we get smoother and thinner films and even a monolayer film of the 1.2 nm gold core with a 1.1 nm organic-coating, provided the films are lifted on to the substrates within few minutes of the reaction. It should be possible to produce 1.2 nm gold nanoparticles on a large scale by this method. The films produced on the normal table were much thicker and composed of aggregates of same sized core–shell nanoparticles. But the basic size of the gold nanoparticle remains around 1.2 nm and is dictated by the size of the fingers of two liquids that carry chemicals from one to the other.

6.4 GISAXS Measurements

In this section, we present the results of a GISAXS study that directly provide the size of the gold-core of the nanoparticles and core-core separation that arises due to the presence of the organic shells. The SAXS measurements also allow us to probe the aggregation process of the nanoparticles at the toluene-water interface. Inter-

estingly, the results presented here show that one can get almost mono-dispersed gold nanoparticles even when the interfacial film becomes thick in the absence of an anti-vibration table as discussed in the previous section. The use of an anti-vibration table slows down the reaction drastically and does not permit the large scale production of the core-shell nanoparticles. Fluctuations, microscopic as well as macroscopic, at the liquid-liquid interface play a crucial role in interfacial reactions [116]. The macroscopic fluctuations at the interface, introduced by external mechanical vibrations in the absence of the anti-vibration isolation, can increase the rate of the reaction to form thicker films. The present results show that the size of the gold-core remain almost unchanged even as the film becomes thick.

SAXS is an established technique [190, 191, 192, 193, 194, 195] to probe aggregation processes and this technique has been extended to grazing incidence geometry (known as GISAXS) to make it sensitive for surface/interface studies. To the best of our knowledge, this technique has not been applied to understand aggregation process at the liquid-liquid interface. The two dimensional nature of the liquid-liquid interface makes the SAXS measurement and its analysis more challenging. Scattering in typical SAXS measurements is three dimensional in nature wherein a confined beam of x-ray is allowed to scatter from a sample of interest and the scattered intensity is measured as a function of wave transfer vector $\vec{q}$ (q_x, q_y, q_z). In GISAXS measurements, the incident angle is kept at a small angle, around the critical angle of the interface and the scattering becomes different in the q_z and q_x(or q_y) directions. In the present experiment, two dimensional scattering is obtained in the initial stage of reaction but as the amount of nanoparticles increases at the interface due to reaction and the film thickens, the scattering tends to become isotropic in all the directions and depends only on the magnitude of the wave vector i.e $q = |\vec{q}| = \sqrt{q_x^2 + q_y^2 + q_z^2}$. We shall discuss experimental details in the next section. In the subsequent sections data analysis and results will be discussed.

6.4.1 Experimental Details

In the present study, we have used low concentrations of the chemicals compared to those used earlier [65] to slow down the reaction. We prepared fresh solutions of

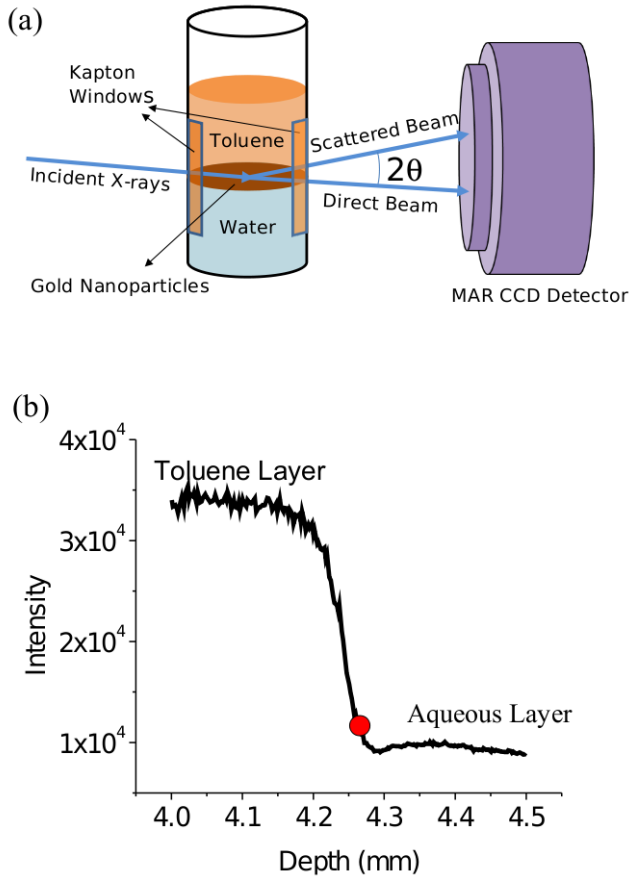

Figure 6.10: (a) Schematics of the experimental setup and small Teflon cell used for the scattering experiments. (b) The direct beam intensity, passing through the cell containing the liquid, as a function of depth. The change in intensity is observed at the toluene water interface. The red circle is marked to locate the position of the interface from which all scattering data are collected.

the gold precursor, $Au(PPh_3)Cl$ (triphenylphosphine gold chloride), in toluene, an aqueous solution of NaOH (sodium hydroxide) and THPC (tetrakis-hydroxymethyl phosphonium chloride) of concentrations 0.25 mM , 0.625 mM and 50 mM respectively. THPC is the reducing agent in this reaction. We carried out the reactions in a specially prepared Teflon cell kept on the goniometer table of beamline without vibration isolation (discussed in details in the next subsection). For the reactions, 2 ml solution of the gold precursor $Au(PPh_3)Cl$ in toluene was allowed to stand on 3 ml NaOH aqueous solution. The reaction was initiated by injecting 55 μl of THPC in the aqueous layer by a syringe with least disturbance of the interface. The injecting time of the reducing agent was taken to be the starting time of the reactions.

Absorption of X-rays plays a crucial role in designing the geometry of SAXS measurements from a liquid-liquid interface. In conventional SAXS measurements, X-rays are allowed to scatter from a dilute solution of sample kept in a thin capillary tube. The grazing incidence measurement (GISAXS) employed here requires larger interfacial region that can be achieved by increasing the diameter of the tube containing the liquids. Increase in the diameter reduces measured intensity due to absorption of the X-rays by the liquids. Keeping the thickness and absorption coefficients in mind, we prepared a Teflon cylindrical cell of diameter 20 mm as shown in 6.10(a) and used 16 keV (wavelength, λ=0.0775 nm) X-rays of X21 beamline of National Synchrotron Light Source, Brookhaven National Laboratory (BNL), USA, for our experiments. Two windows were cut on diametrically opposite walls of the cell and kapton sheets of 500 μm thickness are attached to allow X-rays to go in and out of the cell for scattering measurement. The X-ray beam was first defined by a pair of slits (200 μm (vertical) $\times$ 500 μm (horizontal)) and then allowed to incident on toluene-water interface with an angle of 0.08 degree. We could not employ lower incident angle (note that critical angle for toluene-water interface is 0.03 degree) as larger portion of flat meniscus was not available in the cell. The diameter of the cylindrical cell was kept quite large to avoid scattering from meniscus that changes with the reaction. The strategy was a compromise between reducing the background scattering coming from the solution and having a flat enough interface to allow proper measurements.

The scattered intensity was collected using a two dimensional (2D) MAR CCD detector. The wave vector transfer defined by the scattering angle 2θ for our experiment is $q = (4\pi/\lambda)\sin\theta$. The detector to sample distance was chosen to have q-range from 0.6 nm^{-1} to 6 nm^{-1} corresponding to length scale of 10.5 nm and 1.05 nm in real space. This length scale is ideal for studying the structure of aggregates of size 8 nm with the 1.2 nm gold-core nanoparticles as predicted in the earlier measurements. In our experiment, we blocked the direct beam with two types of beam stoppers. The large rectangular beam stopper (shown in right panel of Figure 6.11) was used to collect the three dimensional isotropic scattering at large **q** values while small rectangular beam stopper (shown in the left panel of Figure 6.11) was used to

collect the anisotropic scattering along q_z.

After the formation of the interface between the precursor solution in toluene and aqueous solution, we aligned the interface with the direct beam. In order to do that we collected the direct beam intensity passing through the cell with a point detector as the sample cell is scanned vertically. The interface could be located by a sharp change in the transmittance of the direct beam intensity (shown in Figure 6.10(b)) due to the difference in absorption coefficients of toluene and water. By performing few initial measurements with the 2D detector during the film formation, we found that the scattering from the gold nanoparticles could be observed properly when beam is at a particular position (marked as red circle in Figure 6.10(b)) where the intensity of the direct beam was observed to be 90% of that from the toluene layer. We performed two sets of GISAXS measurements with the same settings but different sized beam stoppers to monitor the gold nanoparticle formation at the toluene-water interface as a function of time. We monitored the reaction for 350 minutes and the changes became slow beyond this reaction time.

6.4.2 Results and Discussions

Representative data obtained with two different beam stoppers are shown in Figure 6.11. Isotropic scattering from the Kapton windows produces an isotropic ring at q = 4 nm^{-1} (marked as 'K') in the data. Representative data collected with smaller beam stopper at the initial stage of the reaction in the left panel of Figure 6.11 show Keissig fringes along the q_z directions indicating the formation of a thin film at the interface. The period of these fringes decreased with reaction time indicating thickening of the film. We observed the formation of a circular ring (marked as 'P') due to nanoparticle correlations at q=2.8 nm^{-1} after 30 minutes of the reaction. The data shown in Figure 6.11(d) was collected after 78 minutes of reaction show this isotropic ring. In the second set of data with large beam stopper, we obtained better statistics for the correlation peak 'P' to carry out detailed analysis (refer Figure 6.11(e)-(h)).

The formation of fringes along q_z at the initial stages of the reaction and the formation of isotropic ring at q=2.8 nm^{-1} at the later stage are the signatures of

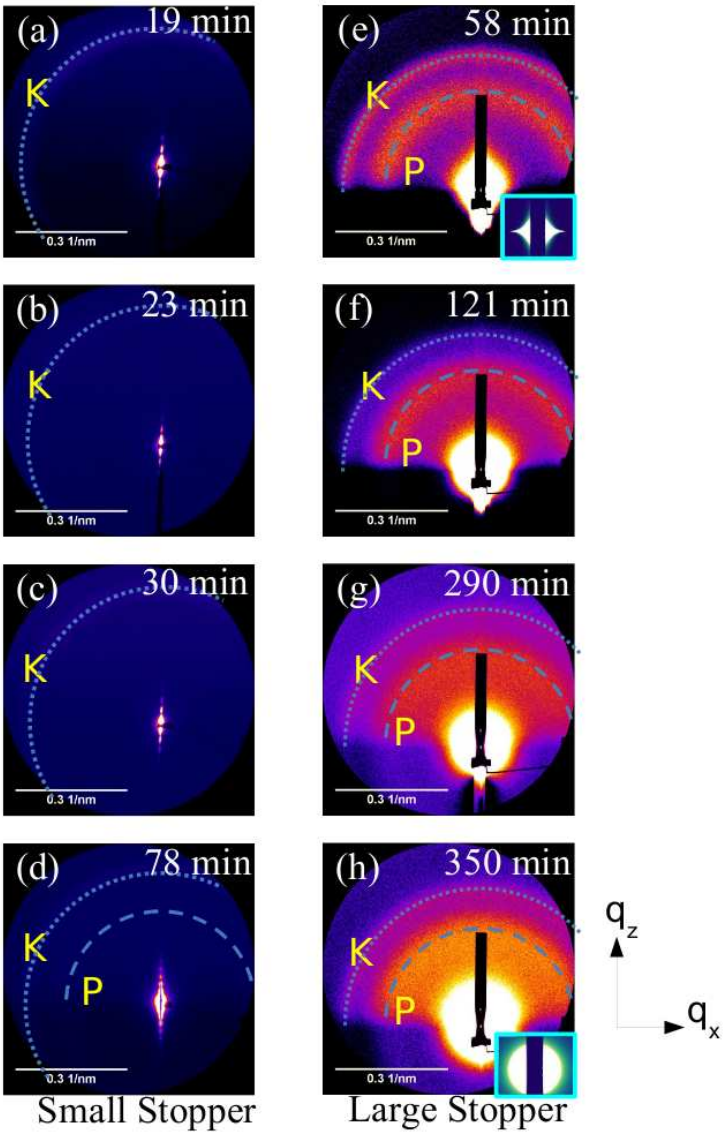

Figure 6.11: The two-dimensional scattering data collected by MAR CCD detector with small beam stopper after (a) 19 minutes, (b) 23 minutes, (c) 30 minutes, (d) 78 minutes and with large beam stopper after (e) 58 minutes, (f) 121 minutes, (g) 290 minutes and (h) 350 minutes after initiation of reaction. Insets of (e) and (h) are calculated scattering profiles from capillary wave theory and fractal structure as discussed in the text.

formation of the film of gold nanoparticles and its aggregation. In order to obtain quantitative information about the film thickness and the aggregation process, we analyzed different regions of the 2D data separately. There are three important regions of the data: (a) the low q_z region with Keissig fringes obtained with small beam stopper, (b) the peak at q=2.8 nm^{-1} and (c) the q region from 0.4 to 1 nm^{-1} of the data collected with large beam stopper. The third region provides information about the nature of aggregation of the nanoparticles in the films at the toluene-water interface.

The scattering at low q region is highly anisotropic at the initial stages of the reaction as evident from Figure 6.11 (a)-(e). At later stages of reaction, the scattering in the low q region became isotropic (refer Figure 6.11(f)-(h)). Scattering intensity collected at the early stage of reaction from toluene-water interface (shown in Figure 6.11(e)) with larger beam stopper, show the capillary wave scattering at low q values. For qualitative comparison, we have shown in the inset of Figure 6.11(e), a two dimensional plot of intensity calculated from capillary wave theory. [**?**, **?**] The high background did not allow us to do the quantitative analysis [112] of line profile along q_x direction. As the reaction progressed, 3D scattering became apparent leading to isotropic scattering from gold-particles both at low and high q values as shown Figure 6.11(f)-(h). In the inset of Figure 6.11(h) we have shown the isotropic scattering intensity calculated from fractal structure of aggregates of gold nanoparticles that will be discussed later.

The low q_z region

For the analysis of Keissig fringes, we extracted the line profiles (refer Figure 3(a)) as a function of q_z, integrated over small q_x values along the region marked as a line in the inset of Figure 3(a). The profile at the initial stage of reaction **is** slightly tilted due to the tilting of the meniscus. As the reaction progressed the meniscus flattened due to the presence of organic-shell covered nanoparticles and became horizontal at later stages.

Fixed incidence angle (θ_i) scattering data at $q_x = 0$ shown in Figure 6.12(a) were analyzed using capillary wave theory [156, 112, 117] assuming the film of gold

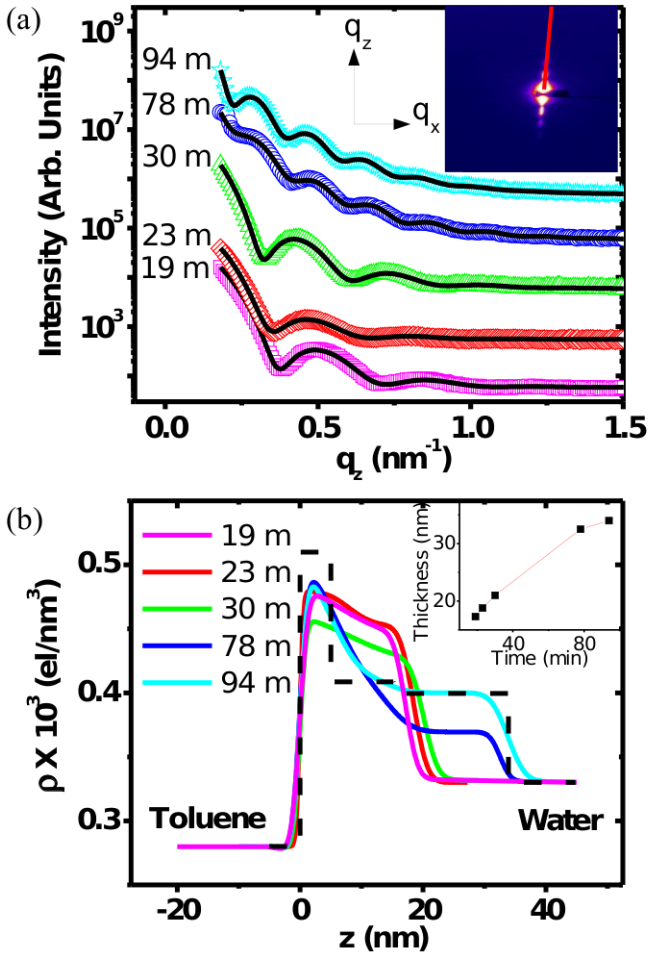

Figure 6.12: (a) The scattered intensities (Symbols) as a function q_z, extracted from line profiles (integrated over small q_x values) on the two dimensional data at different times.Inset: A two dimensional data collected after 23 minutes to show the area marked as red line to extract the line profiles. The solid lines are fits generated from capillary wave theory described in the text. (b) The electron density profiles (solid lines) extracted by fitting the data shown in (a). The solid dashed line show a typical box model used for fitting described in the text. Inset: Plot of thickness of the film as a function of time.

nanoparticles to be conformal with the interface as

$$I(q) \propto \frac{R(q_z)q_z}{2k_o\sqrt{\pi}\sin\theta_i}\Gamma\left(\frac{1-\eta}{2}\right), \tag{6.1}$$

where $\eta = k_B T q_z^2/(2\pi\gamma)$ with k_B, T and γ as Boltzmann constant, temperature and interfacial tension. $k_o = 2\pi/\lambda$ (λ being the wavelength of x-rays) and Γ is the gamma function. $R(q_z)$ is specular reflectivity calculated by using Parratt formalism [153] with discrete box models of electron density profiles (EDP). It is to be noted that in this expression small variation in q_y is neglected. The data were fitted with surface tension value $\gamma = 1.7$ mN/m as as obtained from the GIXS measurements and electron density profile as fitting parameter. The electron density profiles obtained by fitting the data are shown in Figure 6.12(b) with the fitting shown as solid lines in Figure 6.12(a).

During the initial phase of the reaction, the electron density profiles (shown in Figure 6.12(b)) obtained from reflectivity fitting show two noticeable changes with time. Firstly, there is an increase in the film thickness from 18 nm to 34 nm. Secondly, after 30 minutes there is a modification of the electron density profile with the appearance of a lower density film near water. Three-dimensional scattering became prominent after the appearance of this low density layer and isotropic scattering is observed (refer Figure 6.11(d)). The electron density distributions shown in Figure 6.12(b) clearly indicate that the nanoparticles aggregate more compactly away from the water surface giving rise to a decaying electron density towards water interface as the reaction progressed. We can hence infer accumulation of organic phase having less number of nanoparticle-clusters near water interface. The position of the peak at $q = 2.8$ nm^{-1} remain almost unchanged over the entire reaction time as we will discuss later. The layer of nanoparticle-clusters of 40 nm thickness between the toluene and water layers reorganized itself as the reaction progressed. The formation of the ring around $q = 2.8$ nm^{-1} clearly indicates that the scattering from the interfacial layer of 40 nm thickness is three dimensional in nature. A reduction in the rate of reaction is observed after about 60 minutes of reaction and this is apparent in the rate of increase in film thickness as shown in the inset of Figure 6.12(b). This

reduction in the rate of reaction is attributed to the formation of the low density organic layer near water interface hindering the exchange of reactants between the toluene and water layers.

The peak at q=2.8 nm^{-1}

The scattering around q = 2.8 nm^{-1} is isotropic in nature and line profiles for the peak are extracted by azimuthal averaging followed by background subtraction. The data collected from the interface before the initiation of the reaction was considered as background and azimuthal averaging was also done on this background data over the same q range before subtraction. Only the upper half of the q-space is used for this azimuthal averaging as scattering in lower half (through water) is much weaker.

The azimuthally averaged and background subtracted line profiles obtained from the peak (shown in Figure 6.13(a)) were analyzed with cluster model made of 13 nanoparticles discussed earlier. In the absence of anti-vibration isolation, a large quantities of nanoparticles formed and the clusters formed by the nanoparticles starts overlapping. Due to this overlapping there is reorganization of the nanoparticles and number of nanoparticles per cluster get reduced. We have, therefore, analyzed the peak assuming partial occupancy of the nanoparticles in the 13 member cluster. For incorporating partial occupancy we summed over all possible clusters containing N_c nanoparticles ranging from 2 to 13 and write the azimuthally averaged scattering intensity as [122]

$$I(q) = K_o \left|F(q)\right|^2 \left\{ \sum_{N_c=2}^{13} P(N_c) \left(N_c + \sum_{i,j}^{N_c} \frac{\sin qd_{ij}}{qd_{ij}} \right) \right\}, \tag{6.2}$$

where K_o is a constant proportional to the number of scatterers and $F(q)$ is the form factor of the gold-core-organic-shell structure of individual gold nanoparticles with gold core radius R_1 and organic capping thickness t_{org} with electron densities ρ_{core} and ρ_{org} respectively. It is to be noted that in Equation 6.2 and 6.3 we have not considered effects of multiple scattering and neglected the effects of reflection and refraction in this high q-region. $d_{i,j}$'s are the relative distances between the ith and jth nanoparticles in a cluster. The co-ordinates (x, y, z) of

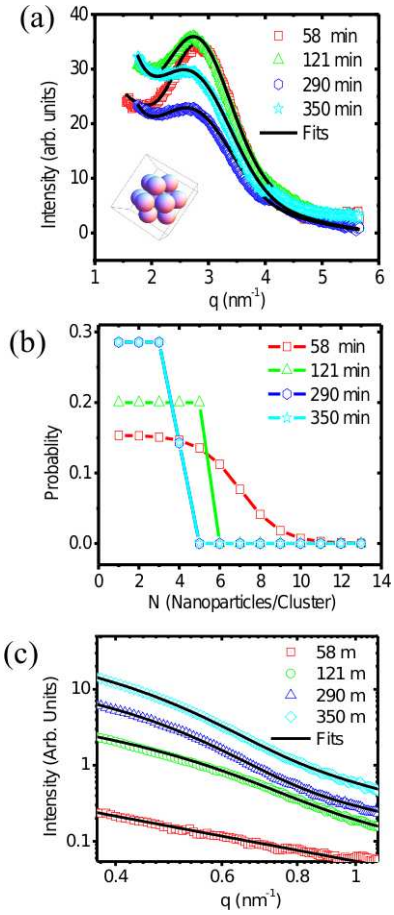

Figure 6.13: (a) The azimuthally averaged background subtracted data (symbols) for q >1.5 nm^{-1} collected at different times and the corresponding fits as discussed in the text. Inset: 3-D schematics of the 13-member cluster. (b) The probability distribution of number of nanoparticles in the aggregates, used to fit the data in (a) as discussed in the text. (c) The background subtracted intensities (symbols) at different times for low q values and the fits (solid lines) by fractal model as discussed in text. The data and the fit obtained for 350 minutes are multiplied by 2 for clarity.

the nanoparticles in a 13 member cluster used in our calculation are $\{0,0,0\}$ for the central nanoparticle, $\{\pm D,0,0\}$, $\{\pm D/2,\pm\sqrt{3}D/2,0\}$ for the six nanoparticles located in plane, $\{\pm D/2,D/(2\sqrt{3}),D\sqrt{2/3}\}$, $\{0,D(-\sqrt{3}+1/\sqrt{3})/2,D\sqrt{2/3}\}$ for three nanoparticles above the plane and $\{\pm D/2,-D/(2\sqrt{3}),-D\sqrt{2/3}\}$, $\{0,D(\sqrt{3}-1/\sqrt{3})/2,-D\sqrt{2/3}\}$ for the remaining three nanoparticles below the plane(shown in the inset of Figure 6.13(a)). $D=2(R_1+t_{org})$, is the separation between the two neighboring nanoparticles in a single cluster and $P(N_c)$ is the probability of getting a cluster with N_c number of nanoparticles. We assume the probability distribution of the cluster as $P(N_c)=\left(1-\tanh\left[(N_c-N_o)/\sigma\right]\right)/2/P_{norm}$ to calculate the scattering intensity from Equation 6.2. Here, σ is the width of the distribution, N_o is the number of nanoparticles in the largest possible cluster and P_{norm} is the normalization factor calculated by integrating the area under the curve of $P(N_c)$'s shown in Figure 6.13(b). The azimuthally averaged background subtracted data (refer Figure 6.13(a)) was fitted with Equation 6.2 keeping N_o, σ, D, and ρ_{org} as free parameters. The calculation using Equation 6.2 was performed by assuming that the most probable state starts with 6+1 gold particles located in a plane (with z = 0) and that 3 gold particles located above and below this plane further constitute the ideal cluster. The electron density of the gold core ρ_{core} and the organic shell ρ_{org} used are relative to the electron density of the toluene i.e 285 el/nm^3. We kept ρ_{core} fixed at 4000 el/nm^3 (bulk electron density of gold relative to that of toluene) in this analysis and the values of ρ_{org} obtained are shown in Table 1 along with the other parameters. We find that all the features of the correlation peak namely - 1) peak position, 2) peak width and 3) the difference between the intensities at the dip and at the peak, are correlated and highly dependent on N_o, ρ_{org}, and D. From Figure 6.2(a) it is evident that with time the difference between the peak intensity and the dip (at q = 2 nm^{-1}) decreased indicating a decrease in the contrast between the gold core and the organic shell. This observation is reflected in the increase of ρ_{org} values coming from our fitting. Also we found an increase in the width of the peak from 0.57 nm^{-1} to 0.62 nm^{-1} by Gaussian fits of the peaks (not shown here). This increase in peak width directly indicates the decrease in inter-particle-correlation of the nanoparticles in a cluster and is well reflected by the decrease in the value N_o.

t (min)	N_o (nm)	σ	D (nm)	ρ_{org} (el/nm^3)	K_o (x10^{-7})	P_{norm}	G	R_2 (nm)	B	d_f
58	7	2.00	2.52	60.0	9.75	6.5	0.0	0.0	0.16	1.49
121	5.5	0.01	2.50	60.0	20.0	5.0	2.75	4.0	0.18	1.82
290	4	0.01	2.44	140.0	23.1	3.5	13.21	4.8	0.28	1.82
350	4	0.01	2.42	200.0	29.4	3.5	31.56	4.9	0.56	2.05

Table 6.1: Parameters obtained from fitting the peak due to separation of nanoparticles and the SAXS data for low q values.

The values of D that determine the peak position showed a small decrease with time by 0.1 nm from 2.52 nm to 2.42 nm indicating compactification of the clusters. We also found the fits to be very sensitive to the core-size of gold nanoparticles ($2R_1$) which remained constant at 1.3 nm throughout the reaction. Apart form the initial value of σ=2.0 after 58 minutes of reaction the value of σ is found to be negligible indicating sharp cut-off of the number of nanoparticles in the cluster around 4. In Figure 6.13(b) we have shown the probability distribution of the clusters calculated from the fitted values of N_o and σ.

The azimuthally averaged and background subtracted peak and fitted curve obtained from Equation 6.2 based on the cluster model having 13 gold nanoparticles provides a clear insight of the ordering of the nanoparticles. When the reaction was carried out on a anti-vibration table, the rate of formation of the nanoparticles was slow and there was sufficient time to form well-separated 13-member equilibrium structures. In the absence of an anti-vibration table, a much thicker film is obtained at the interface due to macroscopic fluctuations. The value of N_o after 58 minutes of reaction showed that the clusters do not prefer to complete the 13-member equilibrium clusters in this situation. Rather they overlap with each other and the resultant clusters contain a smaller number of nanoparticles. This is reflected by the decrease in the value of N_o from 7 to 4 as the reaction progressed. Another important information from our analysis is that though there is a decrease in the number of nanoparticles per cluster with time, an increase in compactification of the structure of the clusters occurred. This compactification is reflected from the decrease in D value from 2.52 nm to 2.42 nm and increase in ρ_{org} value from 60 to

200 el/nm^3 relative to the electron density of toluene. The organic capping thickness around gold core i.e t_{org} calculated as $(D - 2R_1)/2$ is found to be around 0.55 nm. The thickness of the organic capping reveals that the capping is a monolayer coverage of left over organic precursor molecules of size about 0.5 nm **[196].**

The q region from 0.4 to 1 nm^{-1}

Figure 6.13(c) shows the background subtracted scattering intensities at small q values obtained from the interface at different times of the reaction. The presence of gold nanoparticles at the interface increased the scattering intensity at all the q values. Though the length scales probed by our present measurements is just about the size of the clusters, the extracted fractional occupancy motivated us to analyze the data with a fractal structure model at these length scales. We fitted the background subtracted data (shown as solid lines in Figure 6.13(c)) with global fitting function for fractal structures [194, 193, 195] as

$$I(q) = G \exp\left[-q^2 R_2^2/3\right] + B q^{-d_f} \tag{6.3}$$

The first term is the Guinier term and depends on cluster size $2R_2$ and the second term is due to fractal structure of the cluster with fractal dimension d_f. Here, G is Guinier prefactor which depends on number density of nanoparticles and B, the scaling prefactor, signifies the strength of power law scattering arising from the fractal structure [197]. The values of parameters obtained after fitting are enlisted in Table 1. The 2D data collected after 58 minutes of reaction at small q-values with the large beam stopper is highly anisotropic due to capillary wave scattering as shown in Figure 6.11(e). Due to this anisotropy, the values of R_2 and d_f obtained from the fitting of the low q data for 58 minutes are questionable. On the contrary, the low q scattering data for the longer durations of reaction i.e 121 minutes onwards are isotropic and can be considered as three dimensional scattering from clusters of nanoparticles. The values of R_2 and fractal dimension d_f show that cluster size increased with reaction time from 8 to 10 nm and the fractal dimension 1.82 to 2.05. It is known that the fractal dimension of aggregates formed by cluster-cluster

aggregation process is d_f=1.75. The value d_f=1.82 found at early reaction times is close to this value. As the reaction progressed higher values of d_f are obtained along with an increase in the values of G and B. The increase in the values of G and B directly gives a direct indication of the increase in the density of nanoparticles or their compactification. Such an increase in fractal dimension due compactification process has been observed earlier. [190] It is to be noted here that a fractal dimension 2 would be consistent with disc-like aggregates. [195]

6.5 Conclusions

In conclusion, we have studied the aggregation process of gold nanoparticles formed at the toluene-water interface using GISAXS. The measurements provide us direct evidence for the formation of 1.3 nm diameter gold nanoparticles with a particle-particle distance of about 2.5 nm. We demonstrated that in the absence of an anti-vibration, the nanoparticles aggregate to form thick interfacial films where the diameter and separation between nanoparticles remained almost unchanged. The monolayer of 13 member cluster formed in the interfacial reaction with the use of anti-vibration isolation exhibit fractional occupancy as the film thickness increases when the reaction is carried out without the anti-vibration isolation.

By combining both the results of fractal analysis of low-q scattering data and multiple cluster analysis of the peak we can model the growth of the clusters as follows. The reaction at the microscopic level produces gold nanoparticles of sizes around 1.3 nm which aggregate to form incomplete clusters. The clusters are incomplete in the sense that they do not have the full outer shell and the cites are fractionally occupied. The incomplete clusters aggregate to form fractal structures and then reorganize to form compact structures with decrease in inter-particle separation. The increase in fractal dimension from 1.82 to 2.05 is due to the reorganization and compactification of the clusters in the film in the course of the reaction. The compact portion of the film moves towards toluene layer leaving behind an organic-rich layer near water interface.

Chapter 7

Summary

Ultra-thin films of Gold nanoparticles have been studied extensively in the last two decades for their novel physical properties and direct possible applications in the diverse fields of electronics, optics, catalysis and biology. Study of growth and structural properties of these technologically important material is very important to understand along with its physical properties. In this thesis, I have presented the results of our studies to understand growth, morphology and structure of ultra-thin film of organic-capped gold nanoparticles formed at various interfaces. We have used X-ray scattering techniques extensively for our studies along with supplementary techniques like Atomic Force Microscopy (AFM), Transmission Electron Microscopy (TEM), Scanning Electron Microscopy (SEM) and UV-Visible Absorption Spectroscopy.

In Chapter 4, I have shown that monolayer of dodecanethiol encapsulated gold nanoparticles having gold core size $\sim$2 nm exhibits buckling upto a certain surface pressure $<$ 15 mN/m. Above this pressure range the monolayer collapses to give disordered multilayer structure. The buckled monolayer can be thermally annealed below $<$ 15 mN/m to form a well-packed monolayer of larger coverage. We have shown that by increasing the surface pressure upto 13 mN/m, annealing the monolayer and then depositing them on a substrate we can increase the monolayer coverage considerably. In the same chapter, I have shown study of gold nanoparticle having gold core size of 2.4 nm which exhibit irreversible pressure-area isotherm and monolayer to bilayer transition above 13 mN/m. These very nature of irreversibility

of isotherm and bilayer formation of nanoparticles having larger sized core can be attributed to the long range particle-particle interactions compared to the smaller ones.

In Chapter 5, I have shown our studies on the dynamics of monolayer of thiol encapsulated gold nanoparticles just after depositing them on a Silicon and on a soft polymer surface. Nanoparticles on air-water interface form dense monolayer with two dimensional hexagonal-closed-packed structure. After transferring the monolayer to a hydrophilic silicon substrate we found its structure to transform from two dimensional hexagonal-closed-packed structure to bilayer square-lattice within few hours of transfer due to pressure induced by continuous drying of underlying thin water layer. When the same nanoparticles are deposited as a monolayer on the surface of a thin hydrophilic polymer (Polyacrylamide) film, both its in-plane and out-of-plane structure change continuously due to in-plane and out-of-plane movements of nanoparticles. The out-of- plane diffusion of nanoparticles is shown to be non-fickian and slow with exponent $\beta = 0.5$ in comparison to the fickian dynamics with $\beta = 0.29$. The in-plane movement of nanoparticles at the top surface leads to cluster formation, starting with a network structure. Both the in-plane and out-of-plane change in morphology are the resultant of complex interacting forces developed due to polymer itself and the density in-homogeneity across the interface.

In Chapter 6, I have discussed the results of our study of formation, ordering and structure of gold nanoparticles at the toluene-water interface by an interfacial reduction reaction. The size of the nanoparticles which just form due to reaction is found to be 1.3 nm. The formation of nanoparticles accompanies the formation of left over organic precursors and some part of which encapsulate the nanoparticles to restrict their sizes and remaining gets accumulated at the interface hindering the further reactions. After formation the nanoparticles spontaneously self-assemble depending on the presence/absence of external mechanical vibrations. The external mechanical vibrations induce macroscopic fluctuations which increase the rate of reaction to form more nanoparticles resulting in the formation of thicker films of nanoparticles. When the reactions are carried out on a table with anti-vibration isolation the nanoparticles are found to self-organize to form 13-member equilibrium

clusters. While in the absence of anti-vibration isolation, aggregates of incomplete 13-member clusters form and having a fractal structure. The fractal dimension of the fractals approaches the value of 2 which indicates the formation of disc-like aggregates.

Bibliography

[1] G. Schmid, editor. *Clusters and Colloids.* VCH, Weinheim, 1994.

[2] G. Schmid. *In Nanoscale Materials in Chemistry.* Wiley, New York, 2001.

[3] G. Cao. *Nanostructures & Nanomaterials Synthesis, Properties and Applications.* Imperial College Press, London, 2004.

[4] J. H. Fendler, editor. *Nanoparticles and Nanostructured Films.* Wiley-VCH, Weinheim, 1998.

[5] M. C. Daniel and D. Astruc. Gold nanoparticles: Assembly, supramolecular chemistry, quantum-size-related properties, and applications toward biology, catalysis, and nanotechnology. *Chem. Rev.*, 104:293–346, 2004.

[6] I. Matsui. Nanoparticles for electronic device applications: A brief review. *J. Chem. Engg. Japan*, 38:535–546, 2005.

[7] M. Faraday. Experimental relations of gold (and other metals) to light. *Philos. Trans. R. Soc. London*, 147:145, 1857.

[8] J. Turkevitch, P. C. Stevenson, and J. Hillier. Nucleation and growth process in the synthesis of colloidal gold. *Discuss. Faraday Soc.*, 11:55–75, 1951.

[9] M. A. Hayat. *Colloidal Gold, Principles, Methods and Applications.* Academic Press, New York, 1989.

[10] G. Schmid. Large clusters and colloids. *Chem. Rev.*, 92:1709–1727, 1992.

[11] G. Schmid and L. F. Chi. Metal clusters and colloids. *Adv. Mat.*, 10:515–527, 1998.

[12] D. Bethell, M. Brust, D. J. Schiffrin, and C. Kiely. From monolayers to nanostructured materials: An organic chemists view of self-assembly. *J. Electroanal. Chem.*, 409:137–143, 1996.

[13] M. Brust, M. Walker, D. Bethell, D J. Schiffrin, and R. J. Whyman. Synthesis of thiol-derivatized gold nanoparticles in a two phase liquid-liquid system. *J. Chem. Soc., Chem. Commun.*, pages 801–802, 1994.

[14] M. Brust, J. Fink, D. Bethell, D J. Schiffrin, and C. J. Kiely. Synthesis and reactions of functionalised gold nanoparticles. *J. Chem. Soc., Chem. Commun.*, pages 1655–1656, 1995.

[15] U. Freibig and M. Vollmer. *Optical Properties of Metal Clusters*. Springer-Verlag, New York, 1995.

[16] D. L. Feldheim and Jr. A. F. Colby, editors. *Metal Nanoparticless-Synthesis, Characterization and Applications*. Marcel Dekker, New York, 2002.

[17] A. P. Alivisatos. Semiconductor clusters, nanocrystals, and quantum dots. *Science*, 271:933–937, 1996.

[18] M. Brust and C. J. Kiely. Some recent advances in nanostructure preparation from gold and silver: A short topical review. *Colloids Surf. A: Physicochem. Eng. Asp.*, 202:172–186, 2002.

[19] A. Z. Khosousi, P. E. Trudeau, Y. Suganuma, Al-Amin Dhirani, and Bryan Statt. Metal to insulator transition in films of molecularly linked gold nanoparticles. *Phys. Rev. Lett.*, 96:156403–1–4, 2006.

[20] M. Dorogi, J. Gomez, R. Osifchin, R. P. Andres, and R. Reifenberger. Room-temperature coulomb blockade from a self-assembled molecular nanostructure. *Phys. Rev. B*, 52:9071–9077, 1995.

[21] S. Pal, M. K. Sanyal, N. S. John, and G. U. Kulkarni. Formation of a rectifier with gold nanoclusters: X-ray reflectivity and atomic force microscopy measurements. *Phys. Rev. B*, 71:121404(R), 2005.

[22] J. M. Wessels, H. G. Nothofer, W. E. Ford, F. v. Wrochem, F. Scholz, T. Vossmeyer, A Schroedter, H. Weller, and A. Yasuda. Optical and electrical properties of three-dimensional interlinked gold nanoparticle assemblies. *J. Am. Chem. Soc.*, 126:3349–3356, 2004.

[23] S. Underwood and P. Mulvaney. Effect of the solution refractive index on the color of gold colloids. *Langmuir*, 10:3427–3430, 1994.

[24] P. Mulvaney. Surface plasmon spectroscopy of nanosized metal particles. *Langmuir*, 12:788–800, 1996.

[25] W. Rechberger, A. Hohenau, A. Leitner, J. R. Krenn, B. Lamprecht, and F. R. Aussenegg. Optical properties of two interacting gold nanoparticles. *Opt. Comm.*, 220:137–143, 2003.

[26] H. Hovel, S. Fritz, A. Hilger, U. Kreibig, and M. Vollmer. Width of cluster plasmon resonances: Bulk dielectric functions and chemical interface damping. *Phys. Rev. B*, 48:18178–18188, 1993.

[27] M. Quinten and U. Kreibig. Optical properties of aggregates of small metal particles. *Surf. Sci.*, 172:557–577, 1986.

[28] T. H. James, editor. *The Theory of the Photographic Process.* MacMillan Press, New York, 1977.

[29] H. C. V. Hulst. *Light Scattering by Small Metal Particles.* Wiley, New York, 1957.

[30] M. Kerker. *The Scattering of Light and Other Electromagnetic Radiation.* Academic Press, New York, 1969.

[31] Y. N. Hwang, D. H. Jeong, H. J. Shin, D. Kim, S. C. Jeoung, S. H. Han, J. S. Lee, and G. Cho. Femtosecond emission studies of gold nanoparticles. *J. Phys. Chem. B*, 106:7581–7584, 2002.

[32] M. W. Y. Chen and A. Katz. Steady-state fluorescence-based investigation of the interaction between protected thiols and gold nanoparticles. *Langmuir*, 18:2413–2420, 2002.

[33] J. Hu, J. Zhang, F. Liu, K. Kittredge, J. K. Whitesell, and M. A. Fox. Competitive photochemical reactivity in a self-assembled monolayer on a colloidal gold cluster. *J. Am. Chem. Soc.*, 18:1840–1848, 2002.

[34] T. Wang, NewAuthor2, W. Xu, J. Yang, R. Han, and D. Zhu. Preparation, characterization, and photophysical properties of alkanethiols with pyrene units-capped gold nanoparticles: Unusual fluorescence enhancement for the aged solutions of these gold nanoparticles. *Langmuir*, 18:1840–1848, 2002.

[35] K. G. Thomas and P. V. Kamat. Making gold nanoparticles glow: Enhanced emission from a surface-bound fluoroprobe. *J. Am. Chem. Soc.*, 122:2655–2656, 2000.

[36] V. K. Sarathy, K. S. Narayan, J. Kim, and J. O. White. Novel fluorescence and morphological structures in gold nanoparticles- polyoctylthiophene based thin films. *Chem. Phys. Lett.*, 218:543–548, 2000.

[37] P. Xu and H. Yanagi. Fluorescence patterning in dye-doped sol-gel films by generation of gold nanopartilces. *Chem. Mater.*, 11:2626–2628, 1999.

[38] O. V. Makarova, A. E. Ostafin, H. Miyoshi, Jr. J. R. Norris, and D. Meisel. Adsorption and encapsulation of fluorescent probes in nanoparticles. *J. Phys. Chem. B*, 103:9080–9084, 1999.

[39] E. Dulkeith, A. C. Morteani, T. Niedereichholz, T. A Klar, and J. Feldmann. Fluorescence quenching of dye molecules near gold nanoparticles: Radiative and nonradiative effects. *Phys. Rev. Lett.*, 89:203002–1–4, 2002.

[40] T. Gu, J. K. Whitesell, and M. A. Fox. Energy transfer from a surface-bound arene to the gold core in ω-fluorenyl-alkane-1-thiolate monolayer protected gold cluster. *Chem. Mater.*, 15:1358–1666, 2003.

[41] B. Dubertret, J. K. Whitesell, and A. J. Libchaber. Single-mismatch detection using gold-quenched fluorescent oligonucleotides. *Nat. Biotechnol.*, 19:365–370, 2001.

[42] H. Imahori and S. Fukuzumi. Porphyrin monolayer-modified gold clusters as phtotactive materials. *Adv. Mat.*, 13:1197–1199, 2001.

[43] P. Crespo, R. Litràn, T. C. Rojas, M. Multigner, J.M. de la Fuente, J. C. Sànchez-Loþez, M. A. Garcià, A. Hernando, S. Penadès, and A. Fernaǹdez. Permanent magnetism, magnetic anisotropy, and hysteresis of thiol-capped gold nanoparticles. *Phys. Rev. Lett.*, 93:087204, 2004.

[44] Y. Yamamoto, T. Miura, M. Suzuki, N. Kawamura, H. Miyagawa, T. Nakamura, K. Kobayashi, T. Teranishi, and H. Hori. *Phys. Rev. Lett.*, 93:116801, 2004.

[45] P. Dutta, S. Pal, M. S. Seehra, M. Anand, and C. B. Roberts. Magnetism in dodecanethiool=capped gold nanoparticles: Role of size and capping agent. *App. Phys. Lett.*, 90:213102–1–3, 2007.

[46] M. Zhu, C. M. Aikens, M. P. Hendrich, R. Gupta, H. Qian, G. C. Schatz, and R. Jin. Reversible switching of magnetism in thiolate-protected au25 superatoms. *J. Am. Chem. Soc.*, 131:2490–2492, 2009.

[47] M. Haruta, T. Kobayashi, H. Sano, and N. Yamada. Novel gold catalysts for the oxidation of carbon monoxide at a temperature far below zero degree celcius. *Chem. Lett.*, pages 405–408, 1987.

[48] G. J. Hutchings. Vapor phase hydrochlorination of acetylene: Correlation of catalytic activity of supported metal chloride catalysts. *J. Catalysis*, 96:292–295, 1985.

[49] M. M. Schubert, S. Hackenberg, A. C. van Veen, M. Muhler, V. Pizak, and R. J. Behm. Co oxidation over supported gold catalysts - 'inert' and 'active' support materials and their role for the oxygen supply during reaction. *J. Catalysis*, 197:113–122, 2001.

[50] M. Valden, X. Lai, and D. W. Goodman. Onset of catalytic activity of gold clusters on titania with the appearance of nonmetallic properties.

[51] M. Turner, V. B. Golovko, O. P. H. Vaughan, P. Abdulkin, A. B. Murcia, M. S. Tikhov, B. F. G. Johnson, and R. M. Lambert. Selective oxidation with dioxygen by gold nanoparticle catalysts derived from 55-atom clusters. *Nature*, 454:981–983, 2008.

[52] G. Schmid, M. Baumle, M. Gerrkens, I. Helm, C. Osemann, and T. Sawitowski. Current and future applications of nanoclusters. *Chem. Soc. Rev.*, 28:179–185, 1999.

[53] P. Alivisatos, P. F. Barbara, A. W. Castleman, J. Chang, D. A. Dixon, M. L. Klein, G. L. McLendon, J. S. Miller, M. A. Ratner, P. J. Rossky, S. I. Stupp, and M. E. Thompson. From molecules to materials: Current trends and future directions. *Adv. Mat.*, 10:1297–1336, 1999.

[54] R. P. Andres, T. Bein, M. Dorogi, S. Feng, J. I. Jenderson, C. P. Kubiak, W. Mahoney, R. G. Osifchin, and R. Reifenverger. 'coulomb staircase' at room temperature in a self-assembled molecular nanostructure. *Science*, 272:1323–1325, 1996.

[55] A. N. Shipway, E. Katz, and I. Willner. Nanoparticle arrays on surfaces for electronic, optical, and sensor applications. *Chem. Phys. Chem.*, 1:18–52, 2000.

[56] A. S. Edelstein and R. C. Cammarata. *Nanoparticle: Synthesis, Properties and Applications*. Institute of Physics Publishing, Bristol, 1996.

[57] J. H. Liao, K. J. Chen, L. N. Xu, C. W. Ge, J. Wang, L. Huang, and N. Gu. Self-assembly of length-tunable gold nanoparticle chains in organic solvents. *App. Phys. A*, 76:541–543, 2003.

[58] R. Tsunashima, S. Noro, T. Akutagawa, T. Nakamura, T. Karasawa, H. Kawakami, and K. Toma. One-dimensional array of au nanoparticles fixed

on nanofibers of organogelators by the langmuir-blodgett method. *J. Phys. Chem. C*, 111:901–907, 2007.

[59] H. Schwartz, Y. Harel, and S. Efrima. Surface behavior and buckling of silver interfacial colloid films. *Langmuir*, 17:3884–3892, 2001.

[60] B. Kim, M. A. Carignano, S. L. Tripp, and A. Wei. Cluster size analysis of two-dimensional order in colloidal gold nanoparticle arrays. *Langmuir*, 20:9360–9365, 2004.

[61] M. Fukuto, R. K. Heilmann, P. S. Pershan, A. Badia, and R. B. Lennox. Monolayer-bilayer transition in langmuir films of derivatized gold nanoparticles at the gas-water interface: An x-ray scattering study. *J. Chem. Phys.*, 120:3446–3459, 2004.

[62] E. V. Shevchenko, D. V. Talapin, N. A. Kotov, S. OBrien, and C. B. Murray. Structural diversity in binary nanoparticle superlattices. *Nature*, 439:55–59, 2006.

[63] C. N. R. Rao, G. U. Kulkarni, P. J. Thomas, and P. P. Edwards. Metal nanoparticles and their assembly. *Chem. Soc. Rev.*, 29:27–35, 2000.

[64] C. N. R. Rao, G. U. Kulkarni, V. V. Agrawal, U. K. Gautam, M. Ghosh, and U. Tumkurkar. Use of the liquid-liquid interface for generating ultrathin nanocrystalline films of metals, chalcogenides, and oxides. *J. Colloid. Interface Sci.*, 289:305–309, 2005.

[65] C. N. R. Rao, G. U. Kulkarni, P. J. Thomas, V. V. Agrawal, and P. Saravanan. Films of metal nanocrystals formed at aqueous-organic interfaces. *J. Phys. Chem. B*, 107:7391–7395, 2003.

[66] V. V. Agrawal, G. U. Kulkarni, and C. N. R. Rao. Nature and properties of ultrathin nanocrystalline gold films formed at the organic-aqueous interface. *J. Phys. Chem. B*, 109:7300–7305, 2005.

[67] C. P. Martin, M. O. Blunt, and P. Moriarty. Nanoparticle networks on silicon: Self-organized or disorganized? *Nano Lett.*, 4:2389–2392, 2004.

[68] C. P. Martin, M. O. Blunt, E. P. Vaujour, A. Stannard, P. Moriarty, I. Vancea, and U. Thiele. Controlling pattern formation in nanoparticle assemblies via directed solvent dewetting. *Phys. Rev. Lett.*, 99:116103–1–4, 2007.

[69] C. B. Murray, C. R. Kagan, and M. G. Bawendi. Self-organization of cdse nanocrystallites into three-dimensional quantum dot superlattices. *Science*, 270:1335–1338, 1995.

[70] A. J. Kim, P. L. Biancaniello, and J. C. Crocker. Engineering dna-mediated colloidal crystallization. *Langmuir*, 22:1991–2001, 2001.

[71] P. L. Biancaniello, A. J. Kim, and J. C. Crocker. Colloidal interactions and selfassembly using dna hybridization. *Phys. Rev. Lett.*, 94:058302–1–4, 2005.

[72] I Langmuir. The constitution and fundamental properties of solids and liquids. ii. liquids. *J. Am. Chem. Soc.*, 39:1848–1906, 1917.

[73] J. H. Fendler and F. C. Meldrum. The colloidal chemical approach to nanostructured materials. *Adv. Mat.*, 7:607–632, 1995.

[74] Ka Yee C. Lee, Michael M. Lipp, Dawn Y. Takamoto, Evgeny Ter-Ovanesyan, and oseph A. Zasadzinski. Apparatus for the continuous monitoring of surface morphology via fluorescence microscopy during monolayer transfer to substrates. *Langmuir*, 14:2567–2572, 1998.

[75] A. Datta, S. Kundu, M. K. Sanyal, J. Daillant, D. Luzet, C. Blot, and B. Struth. Dramatic enhancement of capillary wave fluctuations of a decorated water surface. *Phys. Rev. E*, 71:041604–1–7, 2005.

[76] G. M. Ribeiro, D. A. A. Ohlberg, R. S. Williams, and J. R. Heath. Rehybridization of electronic structure in compressed two-dimensional quantum dot superlattices. *Phys. Rev. B*, 59:1633–1636, 1999.

[77] S. H. Kim, G. M. Ribeiro, D. A. A. Ohlberg, R. S. Williams, and J. R. Heath. Individual and collective electronic properties of ag nanocrystals. *J. Phys. Chem. B*, 103:10341–10347, 1999.

[78] J. R. Heath, C. M. Knobler, and D. V. Leff. Pressure/temperature phase diagrams and superlattices of organically functionalized metal nanocrystal monolayers: The influence of particle size, size distribution, and surface passivant. *J. Phys. Chem. B*, 101:189–197, 1997.

[79] C. P. Collier, R. J. Saykally, J. J. Shiang, S. E. Henrichs, and J. R. Heath. Reversible tuning of silver quantum dot monolayers through the metal-insulator transition. *Science*, 277:1978–1981, 1997.

[80] S. Pal, N. S. John, P. J. Thomas, G. U. Kulkarni, and M. K. Sanyal. Deposition of a metal-organic heterstructure to form magnetic-nonmagnetic bilayer. *J. Phys. Chem. B*, 108:10770–10776, 2004.

[81] G. Ge and L. E. Brus. Evidence for spinodal phase in two-dimensional nanocrystal self-assembly. *J. Phys. Chem. B*, 104:9573–9575, 2000.

[82] V. F. Puntes, K. M. Krishnan, and A. P. Alivisatos. Colloidal nanocrystal shape and size control: The case of cobalt. *Science*, 291:2115–2117, 2001.

[83] G. M. Whitesides and B. Grzybowski. Self-assembly at all scales. *Science*, 295:2418–2421, 2002.

[84] R. G. Freeman, K. C. Grabar, K. J. Allison, R. M. Bright, J. A. Davis, A. P. Guthrie, M. B. Hommer, M. A. Jackson, P. C. Smith, D. G. Walter, and M. J . Natan. Self-assembled metal colloid monolayers: An approach to sers substrates. *Science*, 267:1629–1632, 1995.

[85] E. Rabani, D. R. Reichman, P. L. Geissler, and L. E. Brus. Drying-mediated self-assembly of nanoparticles. *Nature*, 426:271–274, 2003.

[86] P. Moriarty. Nanostructured materials. *Rep. Prog. Phys.*, 64:297–381, 2001.

[87] A. Stannard, C. P. Martin, E. P. Vaujour, P. Moriarty, and U. Thiele. Dual-scale pattern formation in nanoparticle assemblies. *J. Phys. Chem. C*, 112:15195–15203, 2008.

[88] M. Schmidt and H. Lowen. Freezing between two and three dimensions. *Phys. Rev. Lett.*, 76:4552–4555, 1996.

[89] A. N. Goldstein, C. M. Echer, and A. P. Alivisatos. Melting in semiconductor nanocrystals. *Science*, 256:1425–1427, 1992.

[90] T. A. Weber and R. H. Stillinger. Melting of square crystals in two dimensions. *Phys. Rev. E*, 48:4351–4358, 1993.

[91] J. A. Weiss, D. W. Oxtoby, D. G. Grier, and C. A. Murray. Martensitic transition in a confined colloidal suspension. *J. Chem. Phys.*, 103:1180–1190, 1995.

[92] Y. Han, Y. Shokef, A. M. Alsayed, P. Yunker, T. C. Lubensky, and A. G. Yodh. Geometric frustration in buckled colloidal monolayers. *Nature*, 456:898–903, 2008.

[93] T. Das, S. Sengupta, and S. Sinha. Structural transitions in a crystalline bilayer: The case of lennard-jones and gaussian core models. *J. Phys: Condens. Matter*, 21:195408, 2009.

[94] M. J. Stevens, M. O. Robbins, and J. F. Belak. Shear melting of colloids: A nonequilibrium phase diagram. *Phys. Rev. Lett.*, 66:3004–3007, 1991.

[95] L. B. Chen, C. F. Zukoski, B. J. Ackerson, H. J. M. Hanley, G. C. Straty, J. Barker, and C. J. Glinka. Structural changes and orientaional order in a sheared colloidal suspension. *Phys. Rev. Lett.*, 69:688–691, 1992.

[96] W. Wen, N. Wang, H. Ma, Z. Lin, W. Y. Tam, C. T. Chan, and P. Sheng. Field induced structural transition in mesocrystallites. *Phys. Rev. Lett.*, 82:4248–4251, 1999.

[97] A. Chaudhuri, S. Sengupta, and M. Rao. Stress relaxation in a perfect nanocrystal by coherent ejection of lattice layers. *Phys. Rev. Lett.*, 95:266103–1–4, 2005.

[98] A. Sengupta, S. Sengupta, and G. I. Menon. Driven disordered periodic media with an underlying structural phase transition. *Phys. Rev. B*, 75:180201, 2007.

[99] P. Pieranski, L. Strzelecki, and B. Pansu. Thin colloidal crystals. *Phys. Rev. Lett.*, 50:900–903, 1982.

[100] S. Neser, C. Bechinger, P. Leiderer, and T. Palberg. Finite-size effects on the closest packing of hard spheres. *Phys. Rev. Lett.*, 79:2348–2351, 1997.

[101] S. Asakura and F. Oosawa. On interaction between two bodies immersed in a solution of macromolecules. *J. Chem. Phys.*, 22:1255–1256, 1954.

[102] P. Arumugam, H. Xu, S. Srivastava, and V. M. Rotello. Bricks and mortar nanoparticle self-assembly using polymers. *Pol. Inter.*, 56:461–466, 2007.

[103] S. M. Ilett, A. Orrock, W. C. K. Poon, and P. N. Pusey. Phase behavior of a model colloid-polymer mixture. *Phys. Rev. E.*, 51:1344–1352, 1995.

[104] M. S. Kunz, K. R. Shull, and A. J. Kellock. Morphologies of discontinuous gold films on amorphous polymer substrates. *J. App. Phys.*, 72:4458–4460, 1992.

[105] S. Chatoopadhyay and A. Datta. Effect of polymer confinement: Tuning self-assembled growth of monodisperse au nanoparticles on polystyrene films. *Macromolecules*, 40:3313–3319, 2007.

[106] S. Narayanan, D. R. Lee, R. S. Guico, S. K. Sinha, and J. Wang. Real-time evolution of the distribution of nanoparticles in an ultrathin-polymer-film-based waveguide. *Phys. Rev. Lett.*, 94:145504–1–4, 2005.

[107] S. Narayanan, D. R. Lee, A. Hagman, X. Li, and J. Wang. Particle dynamics in polymer-metal nanocomposite thin films on nanometer-length scales. *Phys. Rev. Lett.*, 98:185506–1–4, 2007.

[108] K. S. Mayya and M. Sastry. A new technique for the spontaneous growth of colloidal nanoparticle superlattices. *Langmuir*, 15:1902–1904, 1999.

[109] A. Kumar, S. Mandal, S. P. Mathew, P. R. Selvakannan, A. B. Mandale, R. V. Chaudhuri, and M. Sastry. Benzene-and anthracene-mediated assembly of gold nanoparticles at the liquid-liquid interface. *Langmuir*, 18:6478–6483, 2002.

[110] Y. Lin, H. Skaff, T. Emrick, A. D. Dinsmore, and T. P. Russell. Nanoparticle assembly and transport at liquid-liquid interfaces. *Science*, 299:226–229, 2003.

[111] C. N. R. Rao and K. P. Kalyanikutty. *Acc. Chem. Res.*, 41:489, 2008.

[112] M. K. Sanyal, S. K. Sinha, K. G. Huang, and B. M. Ocko. X-ray scattering study of capillary-wave fluctuations at a liquid surface. *Phys. Rev. Lett.*, 66:628–631, 1991.

[113] J. Daillant, S. Mora, C. Fradin, M. Alba, A. Braslau, and D. Luzet. Structure and fluctuations of liquid surfaces and interfaces. *App. Surf. Sci.*, 182:223–230, 2001.

[114] M. L. Schlossman. X-ray scattering from liquid-liquid interfaces. *Physica B*, 357:98–105, 2005.

[115] M. Fukuto, O. Gang, K. J. Alvine, and P. S. Pershan. Capillary wave fluctuations and intrinsic widths of coupled fluid-fluid interfaces: An x-ray scattering study of a wetting film on bulk liquid. *Phys. ReV. E*, 74:031607–1–19, 2006.

[116] I. Benjamin. Chemical reactions and solvation at liquid interfaces: A microscopic perspective. *Chem. Rev.*, 96:1449–1475, 1996.

[117] J. K. Basu and M. K. Sanyal. Ordering and growth of langmuir-blodgett fims: X-ray scattering studies. *Phys. Rep.*, 363:1–84, 2002.

[118] J. Daillant and M. Alba. High resolution x-ray scattering measurements: I. surfaces. *Rep. Prog. Phys.*, 63:1725–1777, 2000.

[119] G. Luo, S. Malkova, J. Yoon, D. G. Schultz, B. Lin, M. Meron, I. Benjamin, P. Vanysek, and M. L. Schlossman. Ion distributions near a liquid-liquid interface. *Science*, 311:216–218, 2006.

[120] C. Fradin, D. Luzet, A. Braslau, M. Alba, F. Muller, J. Daillant, J. M. Petit, and F. Rieutord. X-ray study of the fluctuations and the interfacial structure of a phospholipid monolayer at an alkane-water interface. *Langmuir*, 14:7327–7330, 1998.

[121] M. L. Schlossman, D. Synal, Y. Guan, M. Meron, G. S.-McCarthy, Z. Huang, Anibal Acero, S. M. Williams, S. A. Rice, and P. J. Viccaro. A synchrotron x-ray liquid surface spectrometer. *Rev. Sci. Instrum.*, 68:4372–4384, 1997.

[122] J. A. Nielsen and D. McMorrow. *Elements of Modern X-Ray Physics*. Wiley, England, 2001.

[123] D. M. Mitrinovic, Z. Zhang, S. M. Williams, Z. Huang, and M. L. Schlossman. X-ray reflectivity study of the water-hexane interface. *J. Phys. Chem. B*, 103:1779–1782, 1999.

[124] M. Mezger, H. Reichert, S. Schoder, J. Okasinski, H. Schroder, H. Dosch, D. Palms, J. Ralston, and V. Honkimaki. High-resolution in-situ x-ray study of the hydrophobic gap at the water-octadecyl-trichlorosilane interface. *Proc. Natl. Acad. Sci*, 103:18401–18404, 2006.

[125] B. R. MacClain, D. D. Lee, B. L. Carvalho, S. G. J. Mochrie, S. H. Chen, and J. D. Litster. X-ray reflectivity study of an oil-water interface in equilibrium with a middle-phase microemulsion. *Phys. Rev. Lett.*, 72:246–249, 1994.

[126] G. Schmid, R. Pfeil, R. Boese, F. Bandermann, S. Meyer G. H. M. Calis, and J. W. A. van der Velden. $[Au_{55}(PPh_3)_{12}Cl_6]$ - a gold cluster of unusual size. *Chem. Ber.*, 114:3634–3642, 1981.

[127] M. Fox. *Optical Properties of Solids*. Oxford University Press, New York, 2006.

[128] U. Kreibig and C. v. Fragstein. The limitation of electron mean free path in small silver particles. *Z. Phys.*, 224, 307-323.

[129] A. Kawabata and R. Kubo. Electronic properties of fine metallic particles. ii. plasma resonance absorption. *J. Phys. Soc. Japan*, 21:1765–1772, 1966.

[130] W. P. Halperin. Quantum size effects in metal particles. *Rev. Mod. Phy.*, 58:533–606, 1986.

[131] A. Rosenauer. *Transmission Electron Microscopy of Semiconductor Nanostructures: Analysis of Composition and Strain State*, volume Volume 182/2003. Springer, Berlin / Heidelberg, 2003.

[132] C. J. Lawrence. *Phys. Fluids*, page 2786, 1988.

[133] K. B. Blodgett. Films built by depositing successive monomolecular layers on a solid surface. *J. Am. Chem. Soc.*, 57:1007–1022, 1935.

[134] K. B. Blodgett and I. Langmuir. Built-up films of barium stearate and their optical properties. *Phys. Rev.*, 51:964–982, 1937.

[135] W. Kern and J. Vossen, editors. *Thin Film Processes.* Academic Press, New York, 1978.

[136] W. Kern, editor. *Handbook of Semiconductor Cleaning Technology.* Noyes Publishing, Park Ridge, NJ, 1993.

[137] W. C. Roentgen. On a new kind of rays. *Nature*, 53:274–276, 1896.

[138] G. F. Knoll. *Radiation Detection and Measurement.* Wiley, New York, 1989 edition.

[139] F. R. Elder, A. M. Gurewitsch, R. V. Langmuir, and H. C. Pollock. Radiation from electrons in a synchrotron. *Phys. Rev.*, 71:829–830, 1947.

[140] *EPICS: Experimental Physics and Industrial Control System.* http://www.aps.anl.gov/epics/, 2003.

[141] *CSS, Certified Scientific Software: SPEC.* http://www.certif.com/spec.html, 2003.

[142] *Notes on Alignment of Liquid Surface Spectrometer.* http://liquids.deas.harvard.edu/x22bnotes.html, 2000.

[143] E. DiMasi. *X22B Liquid Surface Spectrometer.* http://www.solids.bnl.gov/lss/, 2001.

[144] G. Binnig, C. F. Quate, and Ch. Gerber. Atomic force microscope. *Phys. Rev. Lett.*, 56:930, 1986.

[145] G. Binnig, H. Rohrer, Ch. Gerber, and E. Weibel. Surface studies by scanning tunneling microscopy. *Phys. Rev. Lett.*, 49:57–61, 1982.

[146] F. Giessibl. Advances in atomic force microscopy. *Rev. Mod. Phy.*, 75:949–983, 2003.

[147] Joseph Goldstein, Dale E. Newbury, David C. Joy, Charles E. Lyman, Patrick Echlin, Eric Lifshin, Linda Sawyer, and Joseph Michael. *Scanning Electron Microscopy and X-ray Microanalysis.* Kluwer Academic/Plenum Publishers, New York, 2003.

[148] J. Daillant and A. Gibaud, editors. *X-ray and Neutron Reflectivity: Principles and Applications.* Springer, Berlin / Heidelberg, 1999.

[149] M. Tolan. *X-ray Scattering from Soft Matter Thin Films: Material Science and Basic Research.* Springer, Berlin / Heidelberg, 1999.

[150] M. Born and E. Wolf. *Principles of Optics.* Pergamon Press Ltd, London, 2002.

[151] D. J. Griffiths. *Introduction to Electrodynamics.* Prentice Hall, Upper Saddle River, New Jersey, 1999.

[152] J. D. Jackson. *Classical Electrodynamics.* Academic Press, New York, 1999.

[153] L. G. Parratt. Surface studies of solids by total reflection of x-rays. *Phys. Rev.*, 95:359–370, 1954.

[154] T. P. Russell. X-ray and neutron reflectivity for the investigation of polymers. *Mat. Sci. Rep.*, 5:171–271, 1990.

[155] T. V. C. Rao and M. K. Sanyal. The effect of growth defects on the x-ray reflectivity of multilayer systems. *App. Surf. Sci.*, 74:315–321, 1994.

[156] S. K. Sinha, E. B. Sirota, S. Garoff, and H. B. Stanley. X-ray and neutron scattering form rough surfaces. *Phys. Rev. B*, 38:2297–2311, 1988.

[157] M. Piecuch and L. Nevot. X-ray and neutron characterization of multilayer systems. *Mat. Sci. Forum*, 59-60:93–140, 1990.

[158] M. K. Sanyal, S. Hazra, J. K. Basu, and A. Datta. Extraction of density profile for near perfect multilayers. *Phys. Rev. B*, 58:R4258–R4261, 1998.

[159] G. Reiss and R. Lipperheide. Inversion and the phase problem in specular reflection. *Phys. Rev. B*, 53:8157–8160, 1996.

[160] W. L. Clinton. Phase determination in x-ray and neutron reflectivity using logarithmic dispersion relations. *Phys. Rev. B*, 48:1–5, 1993.

[161] K. M. Zimmermann, M. Tolan, R. Weber, J. Stettner, A. K. Doerr, and W. Press. Phase determination of x-ray reflection coefficients. *Phys. Rev. B*, 62:10377–10382, 2000.

[162] *Scilab*. http://www.scilab.org/, France, 2003.

[163] J. W. Goodman. *Statistical Optics*. Wiley, New York, 1985.

[164] M. Abramowitz and I. A. Stegun, editors. *Handbook of Mathematical Functions*. National Bureau of Standards, Washington, 1972.

[165] V. Holy and T. Baumbach. Nonspecular x-ray reflection from rough multilayers. *Phys. Rev. B*, 49:10668–10676, 1994.

[166] S. K. Sinha, M. K. Sanyal, S. K. Satija, C. F. Majkrzak, D. A. Neumann, H. Homma, S. Szpala, A. Gibaud, and H. Morkoc. X-ray scattering studies of surface roughness of gaas/alas multilayers. *Physica B*, 198:72–77, 1994.

[167] S. Sun, C. B. Murray, D. Weller, L. Folks, and A. Moser. Monodisperse fept nanoparticles and ferromagnetic fept nanocrystal superlattices. *Science*, 287:1989–1992, 2000.

[168] Z. L. Wang, S. A. Harfenist, R. L. Whetten, J. Bentley, and N. D. Evans. Bundling and interdigitation of adsorbed thiolate groups in self-assembled nanocrystal superlattices. *J. Phys. Chem. B*, 102:3068–3072, 1998.

[169] R. P. Sear, S. W. Chung, G. Markovich, W. M. Gelbart, and J. R. Heath. Spontaneous patterning of quantum dots at the air-water interface. *Phys. Rev. E.*, 59:R6255–R6258, 1999.

[170] G. U. Kulkarni, P. J. Thomas, and C. N. R. Rao. Mesoscale organization of metal nanocrystals. *Pure. App. Chem.*, 74:1581–1891, 2002.

[171] S. Narayanan, J. Wang, and X. M. Lin. Dynamical self-assembly of nanocrystal superlattices during colloidal droplet evaporation by in situ small angle x-ray scattering. *Phys. Rev. Lett.*, 93:135503–1–4, 2004.

[172] F. C. Meldrum, N. A. Kotov, and J. H. Fendler. Utilization of surfactant-stabilized colloidal silver nanocrystallites in the construction of mono- and multiparticulate langmuir-blodgett films. *Langmuir*, 10:2035–2040, 1994.

[173] F. Dubreuil, P. Fontaine, M. Alba, J. Daillant, J. W. Mays, G. Zalczer, and P. Guenoun. Buckling of charged diblock copolymer monolayers at the air-water interface. *Europhysics Lett.*, 70:176–182, 1995.

[174] E. Matteoli and G. A. Mansoori. A simple expression for radial distribution functions of pure fluids and mixtures. *J. Chem. Phys.*, 103:4672–4677, 1995.

[175] M. A. Garcia, J. de la Venta, P. Crespo, J. LLopis, S. Penadès, A. Fernàndez, and A. Hernando. *Phys. Rev. B*, 72, 2005.

[176] J. N. Israelachvili. *Intermolecular And Surface Forces.* Academic Press, New York, 1992.

[177] D. G. Schultz, X. M. Lin, D. Li, J. Gebhardt, M. Meron, P. J. Viccaro, and B. Lin. Structure, wrinkling, and reversibility of langmuir monolayers of gold nanoparticles. *J. Phys. Chem. B*, 110:24522–24529, 2006.

[178] W. A. Lopes and H. M. Jaeger. Hierarchical self-assembly of metal nanostructures on diblock copolymer scaffolds. *Nature*, 414:735–738, 2001.

[179] A. C. Balazs, T. Emrick, and T. P. Russell. Nanoparticle polymer composites: Where two small worlds meet. *Science*, 314:1107–1110, 2006.

[180] G. Filipcsei, I. Csetneki, A. Szilágyi, and M. Zrínyl. Magnetic field-responsive smart polymer composites. *Adv. Pol. Sci*, 206:137–189, 2007.

[181] V. Zaporojtchenko, T. Strunskus, J. Erichsen, and F. Faupel. Embedding of nobel nanoclusters into polymers as potential probe of the surface glass transition. *Macromolecules*, 34:1125–1127, 2001.

[182] J. H. Teichroeb and J. A. Forrest. Direct imaging of nanoparticle embedding to probe viscoelasticity of polymer surfaces. *Phys. Rev. Lett.*, 91:16104–1–4, 2003.

[183] I. Horcas, R. Fernández, J. M. G. Rodríguez, J. Colchero, J. G. Herrero, and A. M. Baro. Wsxm: A software for scanning probe microscopy and a tool for nanotechnology. *Rev. Sci. Instrum.*, 78:13705–1–8, 2007.

[184] G. J. Kovacs and P. S. Vincett. Formation and thermodynamic stability of a novel class of useful materials: Close-packed monolayers of submicron monodispersed spheres just below a polymer surface. *J. Colloid. Interface Sci.*, 90:335–351, 1982.

[185] M. D. Hughes, Y. J. Xu, P. Jenkins, P. McMorn, P. Landon, D. I. Enache, A. F. Carley, G. A. Attard, G. J. Hutchings, F. King, E. Hugh Stitt, P. Johnston, K. Griffin, and C. J. Kiely. *Nature*, 437:1132, 2005.

[186] Daniel G. Duff, Alfons Baiker, Ian Gameson, and Peter P. Edwards. A new hydrosol of gold clusters. 2. a comparison of some different measurement techniques. *Langmuir*, 9:2310–2317, 1993.

[187] M. G. Nikolaides, A. R. Bausch, M. F. Hsu, A. D. Dinsmore, M. P. Brenner, C. Gay, and D. A. Weitz. Electric-field-induced capillary attraction between like-charged particles at liquid interfaces. *Nature*, 420:299–301, 2002.

[188] R. A. W. Dryfe. Modifying the liquid/liquid interface: pores, particles and deposition. *Phys. Chem. Chem. Phys.*, 8:1869–1883, 2006.

[189] C. Fradin, A. Braslau, D. Luzet, D. Smilgies, M. Alba, N. Boudet, K. Mecke, and J. Daillant. Reduction in the surface energy of liquid interfacesatshort lengthscales. *Nature*, 403:871–874, 2000.

[190] D. W. Schaefer, J. E. Martin, P. Wiltzius, and D. S. Cannell. Fractal geometry of colloidal aggregates. *Phys. Rev. Lett.*, 52:2371–2374, 1984.

[191] P. Dimon, S. K. Sinha, D. A. Weitz, C. R. Safinya, G. S. Smith, W. A. Varady, and H. M. Lindsay. Structure of aggregated gold colloids. *Phys. Rev. Lett.*, 57:595–598, 1986.

[192] A. K. Boal, F. Ilhan, J. E. DeRouchey, T. T. Albrecht, T. P. Russell, and V. M. Rotello. Self-assembly of nanoparticles into structured spherical and network aggregates. *Nature*, 404:746–748, 2000.

[193] G. Beaucage, H. K. Kammler, R. Mueller, R. Strobel, N. Agashe, S. E. Pratsinis, and T. Narayanan. Probing the dynamics of nanoparticle growth in a flame using synchrotron radiation. *Nature*, 3:370–374, 2004.

[194] H. K. Kammler, G. Beaucage, D. J. Kohls, N. Agashe, and J. Ilavsky. Monitoring simultaneously the growth of nanoparticles and aggregates by in situ ultra-small-angle x-ray scattering. *J. App. Phys.*, 97:054309–1–11, 2005.

[195] G. Beaucage. Determination of branch fraction and minimum dimension of mass-fractal aggregates. *Phys. Rev. E.*, 70:031401–1–9, 2004.

[196] R. E. Benfield, A. Filipponi, D. T. Bowron, R. J. Newport, and S. J. Gurman. An x-ray absorption study of gold co-ordination compounds: Exafs refinements and double electron excitation. *J. Phys. Cond. Mat*, 6:8429–8448, 1994.

[197] G. Beaucage. Small-angle scattering from polymeric mass fractals of arbitrary mass-fractal dimension. *J. App. Cryst.*, 29:134–146, 1996.